NASA CONTRACTOR REPORT

NASA CR-2473

NASA CR-2473

EFFECT OF SYMMETRICAL VORTEX SHEDDING ON THE LONGITUDINAL AERODYNAMIC CHARACTERISTICS OF WING-BODY-TAIL COMBINATIONS

by Michael R. Mendenhall and Jack N. Nielsen

Prepared by
NIELSEN ENGINEERING & RESEARCH, INC.
Mountain View, Calif. 94043
for Ames Research Center

NATIONAL AERONAUTICS AND SPACE ADMINISTRATION • WASHINGTON, D. C. • JANUARY 1975

TABLE OF CONTENTS

TABLE OF CONTENTS (CONCLUDED)

EFFECT OF SYMMETRICAL VORTEX SHEDDING ON THE LONGITUDINAL AERODYNAMIC CHARACTERISTICS OF WING-BODY-TAIL COMBINATIONS

By Michael R. Mendenhall and Jack N. Nielsen
Nielsen Engineering & Research, Inc.

SUMMARY

An engineering prediction method for determining the longitudinal aerodynamic characteristics of wing-body-tail combinations is developed. The method includes the effects of nonlinear aerodynamics of components and the interference between components. Nonlinearities associated with symmetrical vortex shedding from the nose of the body are considered as well as the nonlinearities associated with the separation vortices from the leading edges and side edges of the lifting surfaces. The wing and tail characteristics are calculated using lifting-surface theories which include effects of incidence, camber, twist, and induced velocities from external sources of disturbance such as bodies and vortices. The lifting-surface theories calculate the distribution of leading-edge and side-edge suction which is converted to vortex lift using the Polhamus suction analogy. Correlation curves are developed to determine the fraction of the theoretical suction force which is converted into vortex lift. The prediction method is compared with experimental data on a variety of aircraft configurations to assess the accuracy and limitations of the method.

INTRODUCTION

Over the years, high angle-of-attack aerodynamics has become increasingly important for aircraft as, for instance, in such areas as spin avoidance and maneuverability of military aircraft at high altitudes. A principal distinguishing feature of high angle-of-attack aerodynamics is that the aerodynamic lift and pitching moments are no longer linear functions of the angle of attack. Much work has been directed to studying the high angle-of-attack characteristics of components such as wings and bodies, but much less attention has been given to the interference effects between the components of complete configurations in this range. It is the basic purpose of this report to formulate an engineering prediction method for determining the longitudinal aerodynamic characteristics of wing-body-tail configurations which includes the effects of nonlinear aerodynamics of components and the interference among them. Specifically, we will pay particular attention to the nonlinearities associated with symmetrical vortex shedding from the nose of the fuselage and to leading-edge and side-edge separation vortices from the lifting surfaces.

For a sufficiently small range of angles of attack, the lift and pitching-moment characteristics of wings and bodies are usually linear with angle of attack. As the angle of attack is increased, a fuselage nose can shed symmetrical vortex pairs which produce nonlinear lift and moment characteristics. At still higher angles of attack the nose can shed asymmetrical vortices even though at zero sideslip. We will confine our attention to the symmetrical vortex shedding range. Lifting surfaces have linear characteristics up to an angle of attack depending on their aspect ratio and Mach number, among other parameters. However, most thin lifting surfaces possess an angle-of-attack range in which vortices are shed from their leading edges and from their side edges. These additional vortices from a wing can cause additional wing-tail interference at high angles of attack, and are particularly serious for canard configurations. There is a fair amount of data describing the nonlinear behavior of bodies alone and wings alone at high angles of attack, but no general theories suitable for an a priori prediction method are available. For the separation from the leading edges and side edges of wings, the vortex-lift concept of Polhamus (ref. 1) is of use in practical prediction methods.

In developing an engineering prediction method, the first goal is to develop good models for the nonlinear behavior of the components. This is accomplished by a combination of empirical and analytical techniques. The next step is to develop methods for handling the interference among components. The final engineering tool is a computer program incorporating the method with applications to the subsonic and supersonic speed ranges. In order to determine the validity of engineering approximations used in the method and to determine its range of validity, extensive comparison with experiment is required. The program has been designed so that at later stages it can be extended to asymmetrical nose vortices and sideslip.

The linear method presented in reference 2 is one of the common methods for predicting the lift and moment characteristics of wing-body-tail configurations at subsonic and supersonic speeds in the low angle-of-attack regime. The present computer program retains as much of the linear method as possible. Basically, the linear method has been extended to include the effects of symmetrical body vortices and vortices shed from the leading edges and side edges of the lifting surfaces. One basic modification being made to the linear method is that lifting-surface theory is being used to calculate the loading on the lifting surfaces since it can readily handle effects of induced camber associated with vortices. Also, a capability is being added to the method to determine the trajectories of interacting vortices as they sweep back over the configuration.

The scope of the present work includes wing-body-tail combinations at zero sideslip at subsonic or supersonic speeds. All shed vortices must possess mirror symmetry about the vertical plane of symmetry. The range of angle of attack for which the method is valid will vary with Mach number and aspect ratio and must be determined largely from experiment. For instance, an upper limit on angle of attack is presented when vortex bursting occurs over the wing. Another limit would be set by the development of asymmetric vortex shedding from the fuselage nose. It is expected that the computer program will be improved and extended as experience is gained in its use.

The computer programs being discussed in this report are two of four programs for calculating aerodynamic characteristics of wing-body or wing-body-tail combinations. The linear method has been programmed as well as a crossflow method described by Jorgensen in references 3 and 4. Separate programs for subsonic and supersonic speeds have been developed to include nonlinear effects. These programs are being separately documented in a computer manual listed as reference 5.

With regard to the present report, first a general description of the approach is given followed by the details of the predictive method. Then, limited comparisons between experiment and theory are presented for both subsonic and supersonic cases. Suggestions for future work are also made.

SYMBOLS

AR	aspect ratio
a	local body radius
c_{d_c}	crossflow drag coefficient
C_L	lift coefficient, $\frac{L}{qS}$
C_{L_α}	lift curve slope
C_m	pitching-moment coefficient, $\frac{M}{qS\ell}$
C_N	normal-force coefficient, $\frac{N}{qS}$
c	local chord
c_ℓ	section-lift coefficient
c_n	section normal-force coefficient, $\frac{1}{c}\int_{LE}^{TE} \frac{\Delta p}{q_\infty}\, dx$
c_r	chord at juncture of body and lifting surface
c_s	section leading-edge suction coefficient, $\frac{dS/dy}{qc}$
c_{tip}	tip chord of lifting surface
c_x	x-direction section suction coefficient, $\frac{dX/dy}{qc}$
c_y	y-direction section suction coefficient, $\frac{dY/dy}{qc_{tip}}$
F_x	force in x-direction
F_y	force in y-direction
G	velocity functions, equation (10) and Appendix A
K_v	theoretical Polhamus vortex-lift factor

K_v^*	vortex-lift ratio, equation (20)
L	lift force
ℓ	reference length
ℓ_{LE}	length of leading edge
M	pitching moment about center of moments, or free-stream Mach number
N	normal force
Δp	static pressure difference between lower and upper surfaces of lifting surface
q	free-stream dynamic pressure
r	body radius
r_N	radius of base of nose
S	reference area
S_{LE}	suction force normal to leading edge
S_{SE}	suction force normal to side edge
s	semispan of lifting surface, or width of elemental panel in supersonic method
u,v,w	perturbation velocities along x,y,z directions, respectively
V	free-stream velocity
V_N	volume of nose
x,y,z	configuration coordinates with origin at body nose, figure 1
x_e,y_e,z_e	tail coordinates, figure 1
x_w,y_w,z_w	wing coordinates, figure 1
x_{HL}	x location of lifting-surface hinge line

x_m	x location of center of moments
x_s	x position for onset of separation from body nose
$\bar{x}$	center-of-pressure location
z_{HL}	height of lifting-surface hinge line
α	body angle of attack
β	$\sqrt{1 - M^2}$ or $\sqrt{M^2 - 1}$
Γ_B	right body-vortex strength, positive counterclockwise when viewed from rear of configurations
Γ_n	n'th separation-vortex strength on right wing panel
Γ_t	trailing-vortex strength on right wing panel
δ	lifting-surface deflection angle, positive trailing edge down
θ_N	nose angle, degrees
Λ	sweep angle
ν	transformed vortex position, Appendix A
ρ	density
σ	complex vortex position, y + iz

Subscripts

A	afterbody
avg	average
B	body
B(T)	body in presence of tail
B(W)	body in presence of wing
c	canard
e	tail or empennage
HL	hinge line

LE	leading edge
N	nose
p	potential
root	root chord
SE	side edge
T(B)	tail in presence of body
TE	trailing edge
t	trailing vortex
tip	tip chord
v	vortex
W(B)	wing in presence of body
w	wing

Superscripts

( )'	incompressible quantity

GENERAL DESCRIPTION OF APPROACH

Definitions, Notations, and Conventions

Before presenting details of the prediction method, the general approach to the method, the coordinate systems, and the sign conventions are described in this section. In order to proceed with the analysis, the configuration must be subdivided into its basic lifting components as follows:

(1) Nose, N

(2) Wing in presence of body, W(B)

(3) Body in presence of wing, B(W)

(4) Afterbody, A

(5) Tail in presence of body, T(B)

(6) Body in presence of tail, B(T)

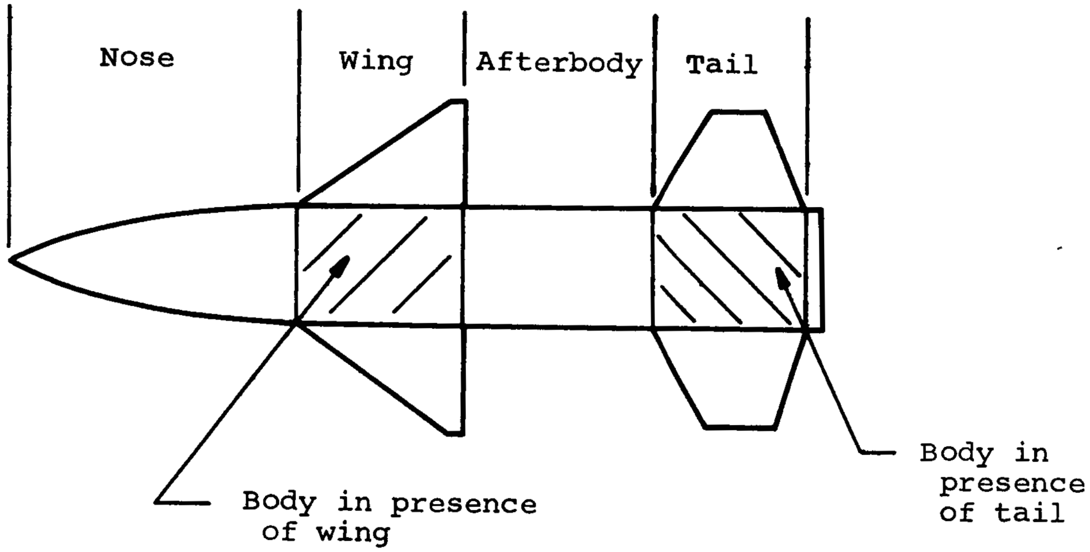

The components are indicated on the above sketch. The nose is taken as that part of the body ahead of the wing leading-edge intersection with the body. The wing in the presence of the body and the tail in the presence of the body are considered to be the exposed lifting panels. The body in the presence of the wing (tail) corresponds to that part of the body onto which any significant part of the lift generated by the wing (tail) panels can be carried over. The shaded areas shown in the preceding sketch correspond roughly to the body in the presence of the wing and the body in the presence of the tail for subsonic speeds. For supersonic speeds, these areas are bounded at their forward parts by Mach lines originating at the leading edge of the wing-body or tail-body junctures. The afterbody is that portion of the body between the wing trailing-edge and the tail leading-edge intersections with the body. The contribution of each of the components including interference effects is calculated and added to determine the complete configuration characteristics.

To standardize the notation for all configurations, the forward lifting surface is denoted the wing and the aft surface the tail, even in the case of canard configurations. Both wing and tail may have incidence with respect to the body axis, but differential incidence between opposite wing or tail panels is not considered.

For the wing-body-tail combination, a set of coordinates, x,y,z are set up with origin at the body nose as shown in figure 1. Wing and tail panels need not be centrally mounted on the body. They have hinge lines located at coordinates as shown in figure 2. The wing and tail panels in combination with the body have coordinate systems designated x_w,y_w,z_w and x_e,y_e,z_e, respectively. The coordinates of the panels are shown for zero panel incidence, and they do not rotate with panel incidence. Positive panel incidence is considered to be trailing edge down, and the positive sense is shown in figure 2.

In the theoretical work involving lifting-surface methods, the wing alone and the tail alone will be introduced. The wing alone is the exposed wing panels joined together, and the tail alone is the exposed tail panels joined together. When the wing and tail are mounted on the body in regions of changing cross section, the undeflected lifting surfaces will usually have root sections which are not parallel to the body axis. In this case, the root section is taken parallel to the body axis at some average body radius, such that there is no change in panel planform area. The panels will then fit smoothly together at their root chords to form the wing alone or tail alone. The coordinate systems attached to the wing alone and tail alone are designated x_w, y_w, z_w and x_e, y_e, z_e, respectively. These coordinate systems originate at the most forward points of the panel leading edges as shown in figure 1. The coordinate transformations, which assume small incidence angles, are as follows for the right-hand panels

$$\left.\begin{aligned} x_w &= x - x_{LE_w} \\ y_w &= y - r_{avg_w} \\ z_w &= z - z_{HL_w} - (x_{HL_w} - x_w)\sin \delta_w \end{aligned}\right\} \tag{1}$$

$$\left.\begin{aligned} x_e &= x - x_{LE_e} \\ y_e &= y - r_{avg_e} \\ z_e &= z - z_{HL_e} - (x_{HL_e} - x_e)\sin \delta_e \end{aligned}\right\} \tag{2}$$

Each of the six components of the configuration contribute to the total force and moment on the complete configuration. Each component has a force and moment associated with potential flow and a force and moment associated with viscous or vortex flow. However, in the case of the afterbody, we will only consider viscous forces and moments. (Part of the lift carryover from the wing panels onto the body may appear on the afterbody.)

The symbols list in a previous section defines all the coefficients and subscripts, but in order to clarify the notation for force and moment coefficients for various components, a systematic set of notation has been compiled in Table 1. The normal force represents the force normal to the axis of the body. Lift is normal to the free-stream direction. Pitching moments are taken about a specified center of moments with a positive moment tending to rotate the configuration to a higher angle of attack. The center-of-pressure locations are measured from the nose of the body in the body coordinate system. The axial force is aligned along the body axis with a positive force directed aft. Since zero angle drag is excluded from the analysis, the only components contributing to an axial force are the lifting surfaces at non-zero incidence angle. Supersonic wave drag is not included.

A system of designation is required for the vortices present in the analysis. Only one pair of body vortices is assumed shed from the nose, and the symbol Γ_B is used to refer to the right body vortex. The sense is such that a counterclockwise rotation, when viewed from the rear of the configuration, is taken as positive. Only one pair of vortices originating at the wing panel trailing edges is considered, and the right trailing vortex is designated Γ_t with the same sign convention as for the body vortices. Since more than one wing separation vortex may be involved, we designate right wing panel separation vortices as $\Gamma_1, \Gamma_2, ..$ with subscripts increasing as the vortices are more outboard.

Summary of Analytical Approach

Before deriving the detailed equations applicable to each lifting element of the configuration, it is useful to summarize the analytical approach. The body potential lift distribution up to the start of the wing is determined by slender-body theory in the same manner as described in reference 2. The vortex characteristics of the body are determined from a combination of data correlation and theory. The available data are analyzed to yield the positions of the vortices as a function of distance behind the body-separation position, x_s. The value of x_s is determined from experimental correlations. The body-vortex strengths are determined from the vortex-lift theorem and experimental normal-force distribution data. The vortex strengths so determined from the data are correlated to provide a chart for prediction purposes. In the foregoing fashion, the body-vortex strength and position are known at every axial station up to the wing. From this information the resulting body normal force and pitching moment can be determined.

The trajectory taken by the body-vortex pair as it moves downstream past the wing and body is computed by conformal transformation and crossflow methods. The presence of the wing is included in this calculation as the vortex pair is imaged inside the wing and body. The effect of wing panel deflection on the body-vortex trajectories is not taken into account. The body vortices do not change strength after they pass the $x = x_{LE_W}$ station.

The next step is to determine the normal force on the wing in the presence of the body. For this purpose the induced velocity normal to the wing panel control points with the deflected panels in the presence of the body are calculated. The normal induced velocity at a particular control point is made up of a free-stream component due to body crossflow, and an induced velocity field due to the body vortices. The induced velocity normal to each wing elemental panel at the control point is calculated with the wing panel in place. The wing panels are then joined together at the root chord and the wing-alone characteristics are determined from the lifting-surface theory. The distribution and center of pressure of the leading-edge suction and side-edge suction are determined at this time.

The next step in the analysis is to set up the wing-separation vortex model. This requires a knowledge of strength of the wing-separation vortices and their positions at the wing trailing edge.

The assumption is made that the rate of vortex shedding from the leading and side edges is proportional to the local leading-edge suction force per unit length. The fraction of the total leading-edge suction which is converted to vortex lift through the Polhamus analogy is not predicted, but it is known that it is not all converted to vortex lift for all aspect ratios. Comparing wing-alone lift data on delta wings in subsonic and supersonic flow with predicted lift curves, including vortex lift, the actual fraction of the theoretical vortex lift required to give good agreement with experiment can be determined. This procedure was carried out for a family of delta wings with aspect ratios from 0.25 to 4 and results in correlation curves for the fraction of theoretical leading-edge vortex lift achieved versus aspect ratio. A similar correlation curve developed from rectangular wing data is available for side-edge vortex lift. From these results we then obtain the wing-separation vortex strength and lateral position. We have been unable to determine the vertical vortex position accurately by theory, so correlated test data for vortex vertical position at the wing panel trailing edge is used. Having determined the vortex lateral position by a method which includes body upwash and body-vortex effects and having determined the loading on the wing panel in the presence of the body, we assume the lateral vortex position as calculated above is not further influenced by the presence of the body.

The lift carryover onto the body in the presence of the wing due to the various components of lift on the wing is obtained from vortex-lift theorems for subsonic speeds and lift interference factors at supersonic speeds.

At the wing trailing edge we have at least three pairs of vortices; one pair of body vortices, a pair of trailing vortices due to the wing potential lift, and one or more pairs of separation vortices. The trajectories of the three pairs of vortices are calculated using methods of conformal transformation in the crossflow plane from the wing trailing edge to the trailing edge of the empennage. The normal-force distribution on the afterbody can then be determined by the vortex-lift theorem.

The induced velocities due to the vortex pairs are determined at the control points on the tail panels. These velocities, together with those associated with the free stream, panel deflection, and body crossflow, allow the tail loading to be calculated in the same fashion as for the wing. The loading on the body in the presence of the tail is determined in a similar fashion as for the body in the presence of the wing. The system of trailing and separation vortices from the tail are calculated, but these vortices do not contribute to the interference on the configuration.

From the loadings on the various components of the configuration, the complete configuration lift force and the induced drag due to lift are calculated. From theoretical calculations of the centers of pressure of the various loadings, the pitching moment of the complete configuration is determined.

PREDICTION METHOD

The detailed analysis of the calculation procedure used for each component of the configuration is presented in this section. Any needed data correlations are also described.

Body Nose

The nose, that part of the body ahead of the wing, generally does not contribute a large portion of the total force on a typical aircraft configuration. For this reason, it is assumed that slender-body theory is sufficiently accurate to predict nose forces and moments due to potential flow. From reference 2, the lift coefficient is

$$C_{L_{N,p}} = \frac{2\pi r_N^2}{S} \sin \alpha \qquad (3)$$

where the trigonometric function of α is used in place of α to improve the results at higher angles of attack. From the same reference, the slender-body theory center of pressure of the potential lift is

$$\bar{x}_N = x_{LE_W}\left[1 - \frac{V_N}{\pi r_N^2 x_{LE_W}}\right] \tag{4}$$

where V_N is the volume of the nose.

As the angle of attack of a body increases, flow separation occurs on the leeward side. This separated flow has been observed to consist of concentrated vortices. At intermediate angles of attack, this vorticity is in the form of a symmetrical pair of vortices. As the angle of attack increases, the pair of vortices become asymmetric. The present investigation is concerned only with the symmetrical pair of vortices. This shed vorticity is a source of nonlinear loading which must be accounted for in the prediction of forces and moments on the body nose. Further, these shed body vortices are a source of interference on the wing and tail surfaces downstream of the origin of separation. Thus, it is necessary that a method be developed to describe the vortex characteristics and the associated induced loadings.

The range of angle of attack over which a symmetric, steady vortex system occurs must be defined. As the angle of attack is increased above this range, the vortex system becomes asymmetrical and side forces are induced on the body. Available data on the onset of body-flow separation and the onset of asymmetric vortex shedding have been correlated (refs. 6 to 23 and 61). The angle of attack for the onset of asymmetrical vortex shedding as a function of nose fineness ratio is presented in figure 3. A recommended boundary is shown on this figure. Configurations which fall above the boundary are considered to be outside the range of applicability of the current method.

For a body alone, separation occurs first at the aft end. As the angle of attack is increased, the separated region extends further forward until it finally covers most, if not all, of the body length. Thus, some means of determining the axial location where separation begins must be obtained. For this purpose, data were examined to develop an appropriate analytical relation.

The available data were generally determined by one of three methods; examination of circumferential pressure distributions, vapor screen indications of the presence of a vortex pair, and surface flow visualization. The first two methods are not very sensitive indicators. In addition, circumferential pressure distributions are taken at discrete intervals along the models, which yields an uncertainty of up to the interval length. Surface flow visualization is perhaps the most reliable indicator, but it is difficult to interpret at the forward edge of the separated region. Thus, there is considerable uncertainty associated with attempting to define the origin of separation on an inclined body.

Data on the origin of separation are shown in figure 4. The data are separated according to the bluntness of the body nose. For sharp-nose bodies, (fig. 4(a)), several investigations show results in the form of bands one to two diameters wide, generally obtained by the first two methods noted above. The data points from reference 18 were obtained from surface flow visualization and tend to fall below the bands. It is probable that there is some angle of attack of the order of 4° below which separation does not occur on bodies of reasonable length. Further, cone data indicate separation to occur up to the nose at angles of attack of the order of the cone semiapex angle, so it is probable that separation does originate at the nose of pointed-nose bodies at sufficiently high angles of attack. As a result of these data and considerations, the following expression was chosen for sharp-nosed bodies.

$$\frac{x_s}{r_N} = 32\left[1 - \sqrt{\frac{\alpha - 4}{\theta_N - 4}}\right] \tag{5}$$

The resulting curve for $\theta_N = 20^\circ$ is shown in figure 4(a).

Data for blunt-nosed bodies are shown in figure 4(b). In this case it appears that the bluntness dominates the separation characteristics such that separation is relatively insensitive to angle of attack. For this case, the following expression was chosen.

$$\frac{x_s}{r_N} = \frac{10}{\alpha - 4} + 2 \tag{6}$$

The resulting curve is shown on figure 4(b).

In the correlation work for vortex strength and position, which is discussed below, the origin of separation must be known. Equations (5) and (6) were used for this purpose. The precise form of these relations is not so important as consistency in their use, in that different relations would result in compensating differences in strength and position correlations to give essentially the same vortex pattern and induced force distribution.

Data on shed vortex strength and position are shown as a function of distance along the body from the origin of separation in figure 5. The vortex strength data collapse into two curves in figure 5(a), one each for subsonic flow and supersonic flow. The lateral vortex position in figure 5(b) also appears to be a function of Mach number and it can be resolved into two curves also. The two recommended curves are shown for Mach numbers less than and greater than one. The vortex vertical positions in figure 5(c) tend to collapse onto a single curve. Note on these correlation curves, the axial distance along the body is normalized by the body radius at the base of the nose, but the strength and position data are normalized by the local body radius.

The vortex-induced force on the nose is determined in the following manner. The separation point is calculated from equations (5) or (6), depending upon nose shape. If the separation point is aft of the wing root leading-edge location, it is assumed that no body vortices are shed and they are not considered in following interference calculations. When separation occurs on the nose, the correlation curves in figure 5 are used to determine the strength and position of the vortex pair along the nose. Once this information is available, the distribution of normal force induced on the nose by the shed vorticity is calculated using the vortex impulse theorem of reference 24.

The vortex impulse theorem simply states that the force induced on a body by a vortex is proportional to the change in the product of the vortex strength and the complex distance between the vortex and its image. Therefore, the normal-force coefficient on the nose between points x_1 and x_2, both of which must lie between x_s and x_{LE_W}, is the following.

$$\Delta C_{N_{N,v}} = \frac{4}{S}\left(\frac{\Gamma_2}{V}\right) \text{Real}(\sigma_{r_2} - \sigma_{r_1}) \tag{7}$$

where

and

$$\left.\begin{aligned} \sigma_{r_n} &= \sigma_n - \frac{a_n^2}{\bar{\sigma}_n} \\ \sigma_n &= y_n + iz_n \end{aligned}\right\} \quad n = 1,2 \tag{8}$$

The nose, between the separation point and x_{LE_W}, is broken into a number of segments and the normal-force coefficient on each segment is computed using equation (7). The total vortex-induced normal force is simply the sum of the normal forces on all the segments. The distribution of normal force can be used to compute a center of pressure.

Vortex Trajectories

Having established the body-separation vortex strength and position at the wing leading edge, it is now necessary to compute the trajectory of the symmetrical vortex pair as it moves downstream past the wing. Since there will be more than one pair of symmetric vortices in the flow field downstream of the wing, the trajectory equations in this section will be developed for an arbitrary number of symmetrical vortex pairs.

At some initial axial station at which the trajectory integration is to begin, the vortex strengths, Γ_n, and position, y_n and z_n, are known. The differential equations of motion for each vortex are written as

$$\frac{d\bar{\sigma}_n}{dx} = \frac{v_n - iw_n}{V_\infty} \tag{9}$$

which can be expressed in terms of the G-functions derived in Appendix A.

$$\frac{v_n - iw_n}{V_\infty} = G_{c_n} + \underbrace{\sum_n \sum_m}_{n \neq m} G_{mn} + G^*_{nn} + G_{T_n} \tag{10}$$

Combining equations (9) and (10) results in a set of 2n differential equations which may be integrated from the initial location to some point downstream. Thus, the trajectories of the n vortices in the field are determined simultaneously.

When the leading edge of the wing is supersonic; that is, it lies in front of the Mach cone, the vortex trajectories are assumed to move parallel to the lifting surface with no change in lateral position. Between the wing trailing edge and the tail leading edge, the trajectories are calculated as described above. If the tail leading edge is supersonic, the trajectories move parallel to that surface without change in lateral position.

Wing in Presence of Body

In reference 2, the lift on the wing (or tail) in the presence of the body is computed using an experimental value for wing-alone C_{L_α} or a value obtained from linear theory, and a slender-body theory interference factor to account for the presence of the body. This same procedure was used for both subsonic and supersonic flows. In the present method, the wing (or tail) loading is computed using a lifting-surface theory. The wing panels are left in place for calculation of the interference flow field, but they are moved together and assumed joined at the root chord for the loading calculation. Since different lifting-surface schemes are used for subsonic or supersonic flows, each of these flow regimes are discussed separately.

Subsonic flow.- Since we are considering the wing alone, the wing coordinate system (x_w, y_w, z_w) shown in figure 1 is used. The compressibility correction is included through use of the Glauert-Prandtl rule which states that the incompressible condition can be obtained from the compressible by stretching the streamwise coordinates by the factor $1/\beta$ and reducing all angles by the factor β. Therefore, the geometric transformations are

$$\left.\begin{aligned} x_w' &= \frac{x_w}{\beta}, \quad y_w' = y_w, \quad z_w' = z_w \\ \alpha' &= \beta\alpha \\ u' &= \beta^2 u, \quad v' = \beta v, \quad w' = \beta w \end{aligned}\right\} \qquad (11)$$

where the prime indicates the incompressible flow condition. The lifting-surface solution is carried out in the incompressible system and the loading results are transformed back to the compressible condition through the following transformations.

The normal force of the wing is proportional to the product of the pressure difference and the reference area

$$\frac{N_W}{N_W'} = \frac{S\Delta p}{S'\Delta p'} = \beta\left(\frac{1}{\beta^2}\right) = \frac{1}{\beta} \tag{12}$$

where we have used the result based on linear theory that the pressure coefficient scales as u .

The suction force on the leading edge is proportional to the product of the pressure difference and the length of the leading edge.

$$\frac{F_x}{F_x'} = \frac{\ell_{LE}}{\ell_{LE}'}\ \frac{\Delta p}{\Delta p'} = \left[\frac{1 + \tan^2\Lambda_{LE}}{1 + \dfrac{\tan^2\Lambda_{LE}}{\beta^2}}\right]^{1/2}\left(\frac{1}{\beta^2}\right)$$

$$= \frac{1}{\beta}\left[\frac{1 + \tan^2\Lambda_{LE}}{\beta^2 + \tan^2\Lambda_{LE}}\right]^{1/2} \tag{13}$$

The suction side force on the streamwise edge, or tip, scales as the product of the pressure difference and the length of the edge.

$$\frac{F_Y}{F_Y'} = \frac{c_{tip}}{c_{tip}'}\ \frac{\Delta p}{\Delta p'} = \beta\left(\frac{1}{\beta^2}\right) = \frac{1}{\beta} \tag{14}$$

Boundary condition: The lifting-surface method chosen to solve the subsonic case is a three-dimensional, vortex-lattice method. The wing is divided into an arbitrary number of trapezoidal area elements. A horseshoe vortex is placed in each area element such that the bound leg lies along the quarter chord of the element and its trailing legs lie along the streamwise edges of the element. The trailing legs are assumed to lie in the plane of the area element. Thus, the wing vortex trailing legs extend back to infinity in the plane of the wing. The area elements have a uniform spacing in the chordwise direction; but in the spanwise direction, the element spacing need not be equal to allow for closer spacing where large loading gradients exist. The wing may have camber, twist, and incidence. The leading and trailing edges may have breaks in sweep and the tip chord must be parallel with the wing root chord. Thickness effects are neglected.

The flow tangency boundary condition is applied at the control points located at the midpoint of the three-quarter chord of each area element. The control points lie in the plane of the wing. The boundary condition states that there is no flow normal to each area element at the control point. The velocities normal to the wing consist of a component of the free stream due to angle of attack, wing incidence, and camber; perturbation velocities induced by the wing horseshoe vortex system; and externally induced velocities. The externally induced velocities are generated by the free vortices in the flow field and body-induced upwash using the method described in Appendix B. Satisfying the boundary condition yields equations for obtaining the circulation strength of each horseshoe vortex. The equations describing the above boundary conditions are presented in detail in reference 25 along with a discussion of the use of a vortex-lattice, lifting-surface method.

Potential lift: Once the circulation values have been computed, the normal force on each wing element can be obtained by means of the Kutta-Joukowski theorem for the aerodynamic force on a bound vortex. The force per unit length on the bound vortex is the density multiplied by the vector product of the velocity and circulation vectors. The line of action is normal to both the velocity vector and the vortex line. For a given area element, the normal force is made up of two parts: the force acting on the bound leg plus the force acting on that part of the trailing legs on the streamwise edges of the area element. Summing these forces over all the area elements results in a total potential normal force for the wing. The distribution of normal force is used to compute a wing-alone center of pressure.

Now, having the wing loading and circulation distribution on the wing, the trailing-vortex system from the wing, due to the potential lift, can be calculated. The trailing vortices from the wing can be computed in two ways. Since the vortex-lattice scheme results in a trailing-vortex filament from each column in the wing lattice, these could be used directly. This would require consideration of as many as twenty vortices and would involve a rolling-up calculation which involves a rather lengthy mathematical process. It is believed that the gain in accuracy achieved in the downstream interference calculations does not make this time-consuming calculation worthwhile. Therefore, the distribution of trailing filaments are combined into a single trailing vortex located at the center of vorticity. Since we know a normal-force spanwise distribution, the lateral position of the trailing vortex representing this span loading is given by

$$y_{w_t} = \frac{\int_0^{s_w} (cc_n)_{W(B),p}\, dy_w}{(cc_n)_{W(B),p}\Big|_{root}} \tag{15}$$

which is measured in the wing-alone coordinate system. The strength of this single trailing-vortex filament is given by

$$\frac{\Gamma_t}{2\pi V} = \frac{S}{8\pi y_{w_t}} C_{N_{W(B),p}} \cos(\alpha + \delta_w) \tag{16}$$

The vertical position of the trailing vortex is assumed to be at the wing trailing edge corresponding to y_{w_t}.

Vortex lift: At high angles of attack, wings can develop more lift than is accounted for by the potential lift just described. For instance, additional lift is associated with flow separation along swept leading edges. Accompanying this additional lift is a separation vortex shed continually along the leading edge. Efforts to predict theoretically the strength and location of this vortex and its induced effects have not been successful. A recently developed approach described in reference 26 shows some promise for an analytical solution of the separation vortex. A simple method of estimating the vortex-lift characteristics of swept wings has been the Polhamus leading-edge suction analogy (ref. 1). This analogy in oversimplified form states that the vortex lift on a delta wing is equal in magnitude to the leading-edge suction on the wing. Physically, the analogy indicates that when flow separates from the leading edge and reattaches on the upper surface, the additional normal force on the upper surface required to maintain flow about the vortex is the same as the leading-edge suction force that is required to maintain potential flow about the leading edge.

The vortex-induced normal force can be written as

$$C_{N_{W(B),v}} = K_{v_{LE}} \sin^2\alpha \tag{17}$$

where Kv_{LE} can be computed from a lifting-surface theory. Charts of $K_{v_{LE}}$ for a variety of swept wing shapes are available in reference 27. Calculation of the vortex lift by the Polhamus analogy gives no indication of where the center of pressure of this part of the lift occurs. Also, existing results are for a wing alone with no external interference effects from bodies or free vortices. The vortex-lattice method is a good means for calculating the leading-edge suction distribution. It also allows external interference effects to be considered.

In a manner analogous to the normal-force calculation, the forces in the x_w, y_w plane of the wing can be computed once the circulation distribution on the wing is known. Let $\vec{e}_x$ and $\vec{e}_y$ be unit vectors in the x and y directions, respectively. We are indebted to Dr. John E. Lamar of Langley Research Center for pointing out the application of the vortex analogy to streamwise edges.

$$\vec{\Gamma} = \vec{e}_x \Gamma_x + \vec{e}_y \Gamma_y \tag{18}$$

and the force per unit length on the vortex element, has x and y components given by

$$F_x = \rho w \Gamma_y \qquad F_y = \rho w \Gamma_x \tag{19}$$

where w is the upwash at the vortex element neglecting its own self-induction at the point. This technique will also result in a y_w-component of force associated with a separation vortex from the streamwise edge of the wing. This use of the vortex-lattice, lifting-surface method allows the distribution of leading-edge and side-edge suction to be computed which gives not only the gross suction force but its center of pressure, assuming that the vortex lift acts directly on the edge where it was generated. In the calculation it is assumed that all inplane forces appear at the edges of the wing planform, but none appears at the trailing edge because of the Kutta condition. It is possible to obtain the gross inplane forces and the streamwise edge side force independently. By subtraction we thus obtain the leading-edge suction force. As a check, it must be perpendicular to the leading edge for straight leading edges. The predicted values of $K_{v_{LE}}$ from the vortex-lattice method agree well with those in the charts in reference 27 for delta wings.

To determine how much of the leading-edge or side-edge suction is converted to a normal force, the following procedure was used. The method of reference 27 was applied to predict the potential lift and vortex lift of a large number of wing-alone configurations for which data are available (refs. 28 to 39).

The potential lift was predicted by two schemes. The first used the theoretical C_{L_α} from reference 27, and the second used an estimated value obtained from the experimental data at $\alpha = 0^\circ$. There is some error involved in fitting a tangent to an experimental lift-curve slope near $\alpha = 0^\circ$.

The lift data for all the wings in references 28 to 39 were analyzed to obtain the potential and vortex-lift components from both prediction methods; one using the theoretical lift-curve slope, the other using an approximate measured value. Assuming that the potential lift was correct, the vortex lift obtained from the measured total lift was compared to the theoretical vortex lift assuming that all the theoretical suction is converted to vortex lift. A suction ratio is defined as follows:

$$K^*_{v_{LE}} = \frac{\text{Experimental } K_{v_{LE}}}{\text{Theoretical } K_{v_{LE}}} \qquad (20)$$

The above ratio is the fraction of the theoretical vortex lift developed by the wing.

The data correlations for $K^*_{v_{LE}}$ are shown in figure 6(a). In this the open symbols represent those values computed using measured C_{L_α} at $\alpha = 0^\circ$ and the solid symbols represent those values computed using an analytical C_{L_α}. In most cases, the solid symbols are slightly higher than the corresponding open symbols. Although there is considerable scatter in the correlations, faired curves are presented to make it easier to chose the appropriate value of $K^*_{v_{LE}}$. When fairing the curves, the data of reference 29 was weighted more heavily than the other references because it contains a systematic series of sharp leading-edge delta wings which were tested to very high angles of attack. The dashed curve is the fairing for the open symbols, and the solid curve is the fairing for the solid symbols. The curves are in fair agreement over the entire range of aspect ratios. In figure 6(a), the leading-edge shape is noted beside each reference. One might expect that wings with sharp edges develop more vortex lift than wings with blunt or rounded edges. There is definite indication of this fact in the data taken on the thickest wing ($t/c = 0.12$) with the largest radius leading edge (ref. 33) which exhibits much less vortex lift than wings of the same aspect ratio with sharp edges. Thin wings ($t/c \leq 0.5$) having rounded leading edges (refs. 36, 37, 38, and 39) possess essentially the same vortex-lift characteristics as sharp-edge wings.

One interesting feature of figure 6(a) is that it points out that delta wings do not develop their full theoretical vortex lift at all aspect ratios. Full vortex lift is achieved on delta wings having aspect ratios in the range of $0.75 < A\!\!R < 1.75$. For zero angle of attack, the experimental value of $K_{v_{LE}}$ should be equal to the drag coefficient of a flat two-dimensional plate normal to the flow, which is about 2. The theoretical value of $K_{v_{LE}}$ for zero aspect ratio is π. Accordingly, the value of $K^*_{v_{LE}}$ at zero aspect ratio is about $2/\pi$. This value is shown on figure 6(a), and the correlation curves have been faired to this value at zero aspect ratio.

The approximate range of validity of the leading-edge factor $K_{v_{LE}}$ for delta wings is shown in figure 6(b) as obtained from the data of references 28 to 35. The upper limit of angle of attack at which the theory fails to predict the nonlinear lift characteristics of sharp-edge delta wings can be determined by vortex bursting. A further discussion of the effects of vortex bursting is included in the concluding remarks of this report.

On wings with finite tips, the normal force induced by a separated tip vortex is assumed to be equal in magnitude to the tip-suction force for attached potential flow (refs. 40 and 62). This side-edge, vortex-induced normal force can be written as

$$C_{N_{W(B),v}} = K_{v_{SE}} \sin^2\alpha \qquad (21)$$

where $K_{v_{SE}}$ can be computed from the vortex-lattice method. The side-edge force distribution is given by the product of the density, the perturbation upwash velocity, and the bound part of the streamwise vorticity at the wing side edges.

Anticipating that a correlation curve for side-edge vortex lift similar to figure 6(a) could be developed for $K^*_{v_{SE}}$, a vortex-lattice, lifting-surface method with leading-edge and side-edge suction-force calculation capability was applied to a series of rectangular wings (refs. 30, 31, 41 to 43). Comparisons between measured and predicted lift coefficients indicate generally good agreement assuming that all the theoretical side-edge suction is converted to lift for rectangular wings with aspect ratios between 0.1 and 5 ($K^*_{v_{SE}} = 1$). At aspect ratios greater than 5, the side-edge vortex lift is a small fraction of the potential lift and, as such, has little effect on the predicted characteristics of rectangular wings. The leading-edge and side-edge suction coefficients as predicted by the vortex-lattice method for rectangular wings in incompressible flow are presented in figure 7(a). The approximate range of validity of the leading-edge factors $K_{v_{LE}}$ and $K_{v_{SE}}$ is shown in figure 7(b) as obtained from the data of references 30, 31, and 41-43. Some data on the effects of Mach number and wing camber are shown.

The vortex-lattice method calculates a spanwise distribution of leading-edge suction and a chordwise distribution of side-edge suction. These results permit calculation of the strengths and lateral positions of any number of vortices used to model separation from the edges. In the following analysis, a model is shown based on two separation vortices per wing panel. Its generalization to many vortices per panel is clear. If a wing has a break in sweep, it might be expected that separation vortices would be shed from both the inboard section and the outboard section. The side-edge separation vortex is assumed to be combined with the leading-edge vortex from the outboard panel as shown in the sketch on the next page. The suction factors $K^*_{v_{LE}}$ and $K^*_{v_{SE}}$

are incorporated into the analysis, but for wings with pointed tips, the side-edge factor $K^*_{v_{SE}}$ is zero.

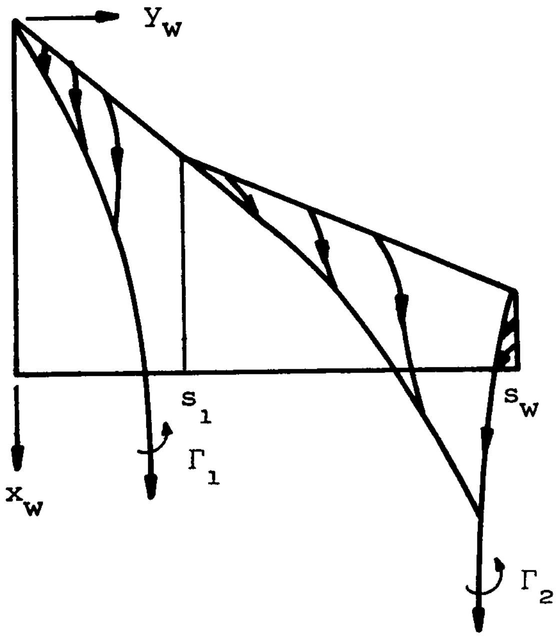

The separation vortex-induced normal force on the inboard panel is

$$C_{N_{v_1}} = 2K^*_{v_{LE}} \int_0^{s_1} \left(\frac{cc_{s_{LE}}}{S} \right) dy_w \tag{22}$$

and that on the outboard panel is

$$C_{N_{v_2}} = 2K^*_{v_{LE}} \int_{s_1}^{s_w} \left(\frac{cc_{s_{LE}}}{S} \right) dy_w + 2K^*_{v_{SE}} \int_{x_{LE_{tip}}}^{x_{TE_{tip}}} \left(\frac{cc_{s_{SE}}}{S} \right) dx_w \tag{23}$$

Assume that the actual distribution of shed vorticity is similar to the theoretical one. Then, the inboard vortex lateral position is given by

$$y_{w_1} = \frac{\int_0^{s_1} (cc_{s_{LE}}) y_w dy_w}{\int_0^{s_1} (cc_{s_{LE}}) dy_w} \tag{24}$$

and its strength is

$$\frac{\Gamma_1}{2\pi V} = \frac{S}{8\pi y_{w_1}} C_{N_{v_1}} \cos(\alpha + \delta_w) \tag{25}$$

The outboard vortex lateral position is

$$y_{w_2} = \frac{K^*_{v_{LE}} \int_{s_1}^{s_w} (cc_{s_{LE}}) y_w dy_w + K^*_{v_{SE}} s_w \int_{x_{LE_{tip}}}^{x_{TE_{tip}}} (cc_{s_{SE}}) dx_w}{K^*_{v_{LE}} \int_{s_1}^{s_w} (cc_{s_{LE}}) dy_w + K^*_{v_{SE}} \int_{x_{LE_{tip}}}^{x_{TE_{tip}}} (cc_{s_{SE}}) dx_w} \tag{26}$$

and its strength is

$$\frac{\Gamma_2}{2\pi V} = \frac{S}{8\pi y_{w_2}} C_{N_{v_2}} \cos(\alpha + \delta_w) \tag{27}$$

The total separation vortex-induced force on the wing is

$$C_{N_{W(B),v}} = C_{N_{v_1}} + C_{N_{v_2}} \tag{28}$$

If only one separation vortex is shed from the wing, its lateral position is given by equation (26) with $s_1 = 0$, and the strength is given by equation (27) with $C_{N_{v_2}} = C_{N_{W(B),v}}$.

The present predicton method provides no means of predicting the vertical position, z_1, of the separation vortex at the wing trailing edge. Examination of data from references 32, 44, and 45, for various delta wings results in a correlation curve for vortex vertical position as a function of angle of attack. These data and the correlation are presented in figure 8. It is seen that the vortex from the leading edge lies approximately one quarter of the distance between the wing chord plane and the free-stream direction.

Supersonic flow.- The lifting-surface method used to solve the supersonic case is a constant-pressure panel scheme obtained from R. Carmichael of the Ames Research Center, NASA. This program is based on the method described in references 46 and 47. The original method has been modified and extended to calculate the forces acting in the plane of the wing; that is, the leading-edge and side-edge suction forces. The leading-edge forces are present only on wings with a subsonic leading-edge, and they are identically zero on wings with supersonic edges. The method of calculating the leading-edge suction distribution is shown subsequently.

Boundary conditions: The supersonic lifting-surface program divides the wing into trapezoidal area elements. Their leading and trailing edges are swept and their side edges are in the streamwise direction. To obtain a trapezoidal lifting element, a planar semi-infinite triangle with uniform loading is used. The trapezoidal element is obtained by a superposition of semi-infinite triangles, each having an apex at one of the four corners of the trapezoidal element. Each trapezoidal lifting element is to be uniformly loaded. For a given Mach number and angle of attack, the loading on each area element is computed by satisfying a flow tangency condition at the control point. The control point is located at the 95-percent station of the chord through the centroid of the trapezoidal element. The element angle of attack is made up of the geometric flow angle, the panel incidence including wing twist and camber, and any induced flow angles caused by the presence of a body or vortices.

Potential lift: The normal force on the wing due to the potential loading is determined by summing the normal force on each area element. The normal force on each element is simply the product of the pressure difference and the element area. The wing pitching moment is computed by summing the contribution due to each area element assuming the normal force to act at the centroid of the element.

Since the spanwise distribution of normal force is known, the lateral position of the trailing vortex representing this span loading is given by the same expression used in the subsonic case, equation (15). The strength of the trailing-vortex filament is given by equation (16). The trailing vortex is assumed to be shed from the wing trailing edge.

Vortex lift: Swept wings in supersonic flow develop additional lift due to flow separation along the leading edge in the same manner as in subsonic flow so long as the leading edge is subsonic. The Polhamus suction analogy (ref. 1) applies in supersonic flow, but special means must be used to calculate the leading-edge suction distribution. The lifting-surface method described previously has been used to calculate the distribution of leading-edge and side-edge suction in the following manner.

The pressure loading on each area element is replaced by an equivalent bound vortex of strength

$$\frac{\Gamma}{V} = \frac{c\Delta c_p}{2} \qquad (29)$$

where c is the chord through the centroid of the element. Thus an equivalent vortex lattice is constructed to represent the wing loading distribution. The bound portion of each horseshoe is located at the midchord of the area element with the trailing legs extending in the streamwise direction as shown in the following sketch.

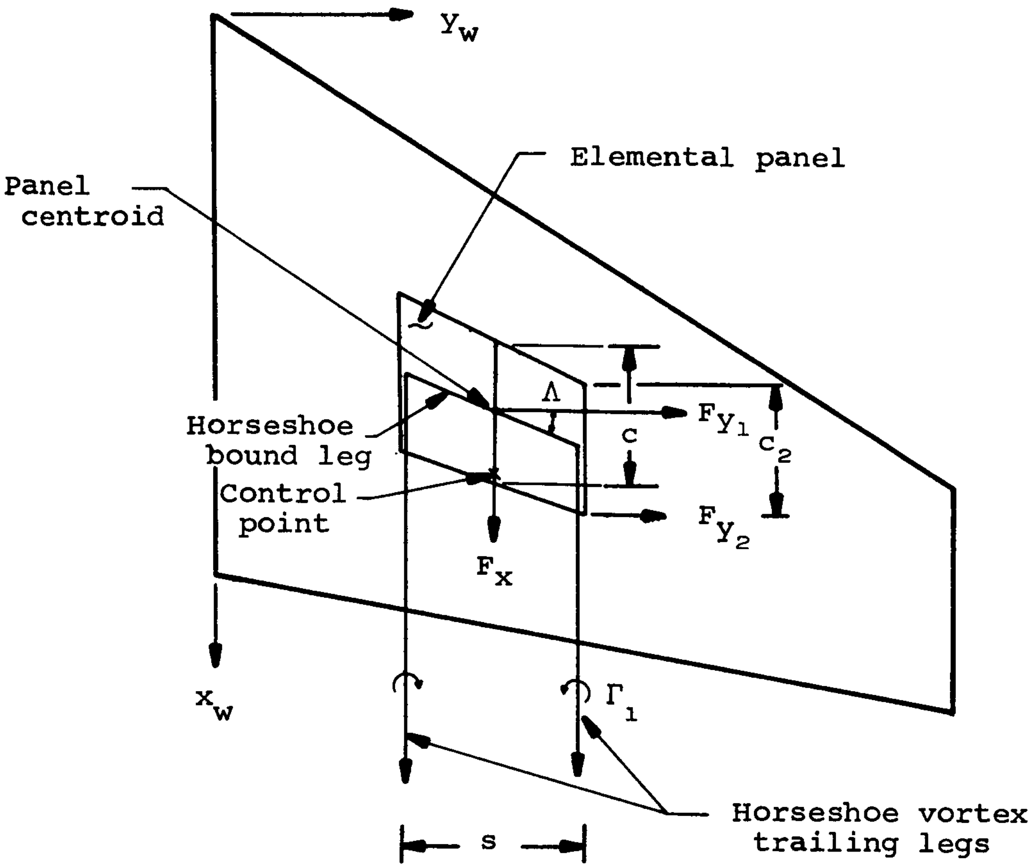

The suction forces in the x_w, y_w-plane of the wing can be computed in the same manner as for subsonic speeds since the circulation strengths are known and the induced upwash field can be calculated. The induced upwash is computed from the supersonic lifting-surface theory in this case, however. The forces on the bound vortex filaments contained within one area element are written as

$$\frac{F_x}{qs} = -\frac{4s}{S}\frac{\Gamma_1}{V}\left(\sin\alpha + \frac{w_1}{V}\right) \tag{30}$$

$$\frac{F_{y_1}}{qs} = \frac{4s}{S}\frac{\Gamma_1}{V}\tan\Lambda\left(\sin\alpha + \frac{w_1}{V}\right) \tag{31}$$

$$\frac{F_{Y_2}}{qs} = 2\,\frac{c_2}{S}\,\frac{\Delta\Gamma}{V}\left(\sin\alpha + \frac{w_2}{V}\right) \tag{32}$$

where w_1 is computed at the centroid of the area element and w_2 is computed at the aft, outboard corner. These forces are calculated on each area element and summed to obtain the net inplane forces on any spanwise strip. Since there is no suction force on the trailing edges, and since the suction force on the side edges can be specifically calculated, the distribution of leading-edge and side-edge suction can now be completely determined.

The question of how much of the leading-edge and side-edge suction is converted into vortex lift at supersonic speeds is approached in the same manner as for the subsonic speeds. The method of reference 1 was applied to predict the potential lift and vortex lift (assuming complete conversion of suction to vortex lift) for which data are available (refs. 48-50). The potential lift was predicted by using the theoretical C_{L_α} from linear theory and an approximate value obtained from the experimental data at $\alpha = 0^\circ$. The potential lift subtracted from the total measured lift then gives the realized vortex lift. The actual vortex lift attained by the wing divided by the maximum theoretical vortex lift is the suction ratio, $K^*_{v_{LE}}$, defined in equation (20) and was obtained for each wing at each Mach number.

The data correlation for the supersonic $K^*_{v_{LE}}$ are shown in figure 9(a). Only the results obtained using the theoretical C_{L_α} are presented in this figure as there was no difference between the correlation curve shown here and the curve obtained when the experimental C_{L_α} was used. The use of $\beta A\!\!\!R$ as a correlating parameter is suggested by the fact that the leading-edge suction is zero for a delta wing with sonic leading edges for which $\beta A\!\!\!R = 4$. The correlation curve of figure 9(a) can be used for wings other than delta wings, provided the aspect ratio used is related to the leading-edge sweep angle by the expression

$$\text{Æ} = \frac{4}{\tan \Lambda_{LE}} \tag{33}$$

This usage assumes that what occurs on the leading edge is not influenced by flow everywhere downstream of the leading edge, a valid assumption at supersonic speeds.

In figure 9(a) the curve for $K^*_{v_{LE}}$ equal unity has been included for comparison purposes. The curve for $K^*_{v_{LE}} = 0$ is the horizontal axis. The results of the data can be assessed in terms of those limits. Generally, the agreement is good, but several notable deviations from correlation are exhibited. For instance, the data of reference 48 for $\beta\text{Æ} \approx 2.6$ show values of $K^*_{v_{LE}}$ of 0 and 1. Also, for $\beta\text{Æ} = 2.6$ another set of data for the same reference exhibit significant deviation from the correlation. Two types of models were used to obtain the data in reference 48. The first set was a series of thin, sharp-edge delta wings. Data on these wings produced the results which fall on the $K^*_{v_{LE}} = 1$ line. The other data were taken on a thick, aspect ratio 1 delta wing with a blunt leading edge. Most of these data fall below the correlation curve. As was also seen in the subsonic correlations, leading-edge bluntness for thick wings can have an effect on vortex lift at supersonic speeds.

A correlation of data for side-edge suction could not be made for supersonic flow because of the lack of data. Since the subsonic results indicate full conversion of side-edge suction to lift, and since no reason is known that this result should be changed by Mach number for streamwise edges, it is recommended that $K^*_{v_{SE}} = 1$ be used.

The approximate range of validity of the leading-edge factor $K_{v_{LE}}$ is shown in figure 9(b) as obtained from the data in reference 49. These data are the only supersonic delta wing data available at angles of attack above the range of validity of the supersonic method.

In supersonic flow, the strength and lateral position of the separation vortices are found from the same expressions derived for subsonic flow. The correlation curve in figure 8 for vertical position must also be used in supersonic flow because of the lack of good vortex location experiments at high speeds.

Body in Presence of Wing

The normal force on the body in the presence of the wing is due to the carryover of loading from the wing to the body. The body force can be calculated using a simplified vortex model described in references 2 and 51. Charts (ref. 2) and tables (ref. 51) are available for rapid calculation of the body normal force. This method basically replaces the wing-body combination with a pair of horseshoe vortices, the strength (Γ_t) of which is computed in the previous section. The trailing-vortex filament is located at y_t given by equation (15). The horseshoe vortex model requires that an image of the trailing filament be located at a^2/y_t as shown in the following sketch.

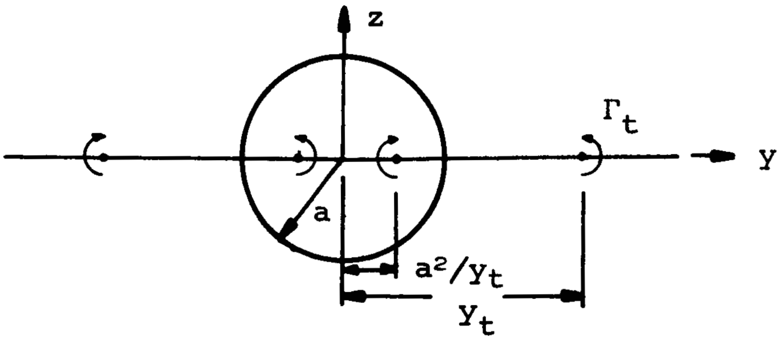

The load on the body is represented by the length of the lifting line inside the body. Thus,

$$C_{N_{B(W),p}} = \left(\frac{a - \frac{a^2}{y_t}}{y_t - a}\right) C_{N_{W(B),p}} \tag{34}$$

The load carried by the body due to the vortex lift on the wing can be calculated in the preceding manner (even though the vortex is not in the plane of the wing) using the strength Γ_1, and the lateral position of the trailing filament, y_1 as obtained from equations (27) and (26), respectively. The vortex is located off the wing at a position

$$\sigma_1 = y_1 + iz_1 \tag{35}$$

as shown in the following sketch.

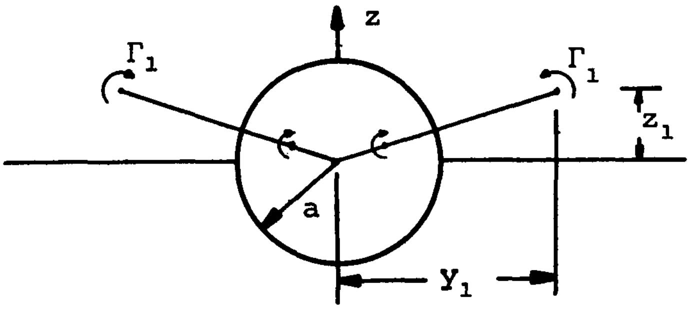

The normal force on the body due to the additional lift on the wing caused by leading-edge separation is

$$C_{N_{B(W),v}} = \left[\frac{a - \text{Real}\left(\frac{a^2}{\bar{\sigma}}\right)}{\text{Real}(\sigma) - a}\right] C_{N_{W(B),v}} \tag{36}$$

For purposes of computing the pitching-moment contribution of these body forces in subsonic flow, the assumption is made that the viscous part of the normal force on the body in the presence of the wing has the same axial location of the center of pressure as does the potential part of the normal force. This assumption is based on the approximation that the center of pressure of the loading carried over onto the body from the wing is not sensitive to the distribution of wing loading.

Equations (34) and (36) are used for the subsonic calculations. In supersonic flow, the force on the body in the presence of the wing is obtained from the method of reference 2. The same factor used to obtain the potential body lift is also used to determine the portion of leading-edge and side-edge vortex lift carried over onto the body. The center of pressure of the lift on the body in the presence of a wing in supersonic flow is also obtained from the methods described in reference 2.

Afterbody

A loading on the part of the body located between the wing trailing edge and the tail leading edge is associated with the presence of the free vortices in the flow field. At this point, the free vortex field can be made up of a pair of body vortices shed from the nose, a pair of trailing vortices representing the potential lift on the wing, and one or more pairs of separation vortices representing the vortex lift on the wing. The trajectories of all these mutually interacting vortices is calculated over the afterbody length; therefore, the induced normal force due to each vortex can be computed using the vortex impulse theorem of reference 24. Thus, the normal force on the afterbody, C_{N_A}, is computed using equation (7). Doing this calculation in stepwise fashion along the afterbody gives a distribution of normal force which can be used to calculate center of pressure.

Tail in Presence of Body

The tail of wing-body-tail configuration is a lifting surface, and it is handled using the same techniques described above for the wing. The only difference between the tail and wing in the calculations is the different positions in the flow field. Where the wing has only a pair of body vortices interferring on it, the tail is affected by the same pair of body vortices plus all the vorticity shed from the wing.

The presence of many free vortices, mutually interacting with each other and the configuration leads to certain problems in the interference calculations. In the trajectory calculations one or more vortices may pass very close to the tail surface. When this occurs, the potential model of the vortex yields large velocities at nearby control points which cause locally unrealistic tail loadings. An example of the type of problem which arose in the present investigation occurred when a trailing vortex passed very near the tail surface on the inboard side of a row of control points. A small change in angle of attack alters the trajectory slightly such that the same vortex now passes near the tail surface and on the outboard side of the same row of control points. Control points on the tail near a vortex can experience a complete reversal of the sense of the large induced upwash and a similar change in the character of the loading. This problem is inherent with the use of discrete control points for satisfying boundary conditions and the use of potential flow models of vortices which are singular at their center.

The problem can be solved through the use of a viscous model of a vortex with a finite core, but this solution was not used in the present investigation. An alternate scheme is to arbitrarily limit the maximum angle of attack induced by a vortex on the grounds of local stall. An arbitrary limit on the maximum induced velocity from a potential vortex results in a vortex tangential velocity profile of the type shown in the following sketch. The

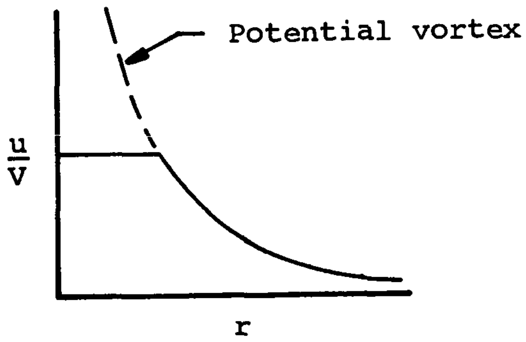

use of this type of correction is discussed in connection with the comparisons with data.

Body in Presence of Tail

The normal force and center of pressure on the body in the presence of the tail is calculated in the same fashion as for the body in the presence of the wing.

RESULTS

In this section, predictions made by various elements of the method are compared with experimental results where possible. Also, predictions of the method are compared with experimental results for complete aircraft configurations of various types. Some limitations of the predicton method are discussed in light of the data comparisons, and general rules are set up for the use of the method.

Wing Alone

Subsonic flow.- The subsonic vortex-lattice, lifting-surface method has been applied to a number of wing-alone configurations for which experimental data are available. In particular, the method has been used to predict the aerodynamic characteristics of delta wings which exhibit both potential lift and leading-edge separation,vortex-induced lift. Some representative results are presented in figure 10 for sharp-edged delta wings. In figure 10(a) the measured and predicted lift and pitching-moment coefficients of an aspect ratio 1.07 delta wing are compared up to the angle of attack for which the wing stalls. Above 10° angle of attack, the vortex lift contributes a substantial amount to the total lift of the wing; and at 30° angle of attack, the vortex lift is greater than the potential lift. The full amount of predicted leading-edge suction is assumed converted to vortex lift through the Polhamus analogy and the agreement between experiment and theory is excellent up to the point of wing stall.

The predictions and the data for pitching-moment coefficients are in good agreement until the vortex lift is approximately one half the potential lift. As the angle of attack increases, the predicted pitching moment becomes more negative. If we assume the potential lift to act at the theoretical center of pressure given by the lifting-surface theory, the pitching moment at $\alpha = 30^{o}$ can be brought into agreement with experiment with a forward shift of 10 percent of the mean aerodynamic chord in the predicted center of pressure of the vortex lift.

Similar comparisons for an aspect ratio 2.31 delta wing are shown in figure 10(b). According to the correlation curve in figure 6(a), a sharp-edged delta wing of this aspect ratio converts approximately 55 percent of its leading-edge suction to vortex lift. The comparisons with experiment in figure 10(b) indicate the predicted lift curve with the limited vortex lift to be in good agreement with the data. It should be pointed out that the results in this figure are included in the subsonic correlation curves in figure 6. The pitching-moment data for this higher aspect ratio delta wing appear similiar to that for the lower aspect ratio wing. There is a tendency for a forward shift in the center of pressure with increase in angle of attack not accounted for by the theory.

The predicted leading-edge suction distribution for the two delta wings discussed above are presented in figure 11 for both wings at 20^{o} angle of attack. The value of $cc_s/2b$ increases in magnitude as aspect ratio decreases,and the maximum section suction coefficient occurs more outboard on the wing at the lower aspect ratios. The suction distribution reduced by the correlation factor is also shown in this figure.

Based on the predicted leading-edge suction distribution, the strength and position of the separation vortex shed from the leading edge is calculated using equations (25) and (26), respectively. No data on vortex strength are available, but a number of observations of the position of the separation vortex have been made (refs. 32, 44, 45, and 52). The predicted lateral position of the leading-edge separation vortex is compared with experimentally observed positions on several aspect ratio 1.0 delta wings. The comparison is shown in figure 12 for an angle of attack of 15°, and the predicted lateral positions are in good agreement with the observed positions for the sharp-edged wings. It is interesting to note from the experimental results that as the wing gets thinner and the leading edge gets sharper, the vortex moves inboard. The predicted results, which correspond in principle to a flat wing with no thickness, lie along the inboard side of the experimental results and may represent the limiting case.

The above prediction method for the vortex lateral position, coupled with the data correlation on vertical position in figure 8, is the basis for predicting the separation-vortex position at the wing trailing edge.

Supersonic flow.- The supersonic lifting-surface method was used to predict the characteristics of an aspect ratio 1.0, sharp-edged delta wing alone (ref. 49) at Mach numbers of 1.96 to 3.30. The vortex lift is specified by the $K^*_{v_{LE}}$ factor from the correlation curve in figure 9(a). The results are shown in figure 13 for lift coefficient versus angle of attack only, as no pitching-moment data are available for this wing. Three curves are shown for each Mach number. One curve represents the potential lift alone with no augmentation due to vortex lift. A second dashed curve represents the potential lift plus the full amount of predicted leading-edge suction converted to vortex lift, and the third curve represents the potential lift plus the correlated vortex lift.

At the lowest Mach number ($M = 1.96$), the predicted lift curve, taken as the potential plus limited vortex lift, is in good agreement with experiment up to about 20° angle of attack.

Above 20°, the measured lift curve drops off more rapidly than the predicted curve. The results for the intermediate Mach number ($M = 2.43$) show the predicted lift curve to be in fair agreement with the measured lift at 20° angle of attack. It appears that the vortex lift factor, K_v^*, is slightly large for this wing as less leading-edge suction is being converted to lift than is anticipated by the correlation curve in figure 9(a). The opposite condition prevails for the highest Mach number ($M = 3.30$) for which slightly more leading-edge suction is converted to vortex lift than is indicated by the correlation curve. For the two higher Mach numbers, the error in predicting the vortex lift is such that the total lift is predicted within 10 percent up to 25° angle of attack.

The leading-edge suction distribution on an aspect ratio 1 delta wing is computed from conical theory which gives a linear spanwise distribution. This result is shown as a dashed line in figure 14. The leading-edge suction coefficients obtained from the supersonic lifting-surface method are shown as symbols in the same figure. The lifting-surface method of predicting leading-edge suction coefficient produces results which agree well with conical theory on the inboard portion of the wing, but tend to be greater than the conical theory near the wing tip. However, the total suction force on the leading edge is nearly the same whether computed by conical theory or the lifting-surface method.

The effect of lattice size and distribution on the leading-edge suction is illustrated in this same figure by the different symbols. The first number is the number of chordwise rows and the second number is the number of spanwise columns. For a fixed chordwise number of lattice panels, the suction distribution approaches a linear distribution as the number of spanwise panels is increased. Increasing the chordwise number of panels tends to raise the level of the suction coefficient. These results indicate that the lifting-surface technique for computing leading-edge suction on a wing alone is in good agreement with conical theory and should be a reasonable method for computing leading-edge suction on wings with interference. Additional accuracy should be obtained by putting the panels more closely spaced at the tip.

The leading-edge, separation-vortex strength and lateral position are computed for supersonic speeds in the same manner as for subsonic speeds. The predicted lateral position on an aspect ratio 1 delta wing is shown in figure 15. Experimental vortex positions are not available for comparison purposes, but comparing the supersonic vortex positions in figure 15 with the subsonic results in figure 12 show that the separation vortex in the supersonic case lies somewhat further outboard than the vortex in the subsonic case on the same shape wing. The vortex position in supersonic flow is nearly independent of Mach number as the calculated difference between $M = 1.96$ and $M = 3.30$ is less than 2 percent of the semispan of the wing.

Vortex Trajectories

The positions and strengths at the trailing edge of the wing of vortices shed from the leading edges can be obtained by methods already described. The position and strength of the trailing vortex representing the wing potential lift is known from lifting-line theory. Thus, at the wing trailing edge, we have a model of the entire wing shed vortex system. This model supplies the initial conditions for the calculation of the trajectories of these vortices as described in a previous section and Appendix A.

A number of unpublished vapor screen pictures of a canard-body-wing configuration (ref. 53) at both subsonic and supersonic speeds were obtained from the NASA/Ames Research Center. Many of these pictures showed the core of the canard vortex system in its trajectory past the body and wing. These experimental trajectories are compared with theoretically determined trajectories in figure 16.

Figures 16(a), (b), and (c) correspond to the configuration at subsonic speeds (M = 0.8). Parts (a) and (b) are for the model at 10° and 18° angle of attack, respectively, with the canard undeflected. Two vortices, shown dashed, are shed from the canard. The largest is the trailing vortex, Γ_t, representing the canard potential lift, and the other vortex is the canard leading-edge separation vortex. These vortices spiral around each other as they move downstream past the wing. The predicted trajectories in these two cases fall quite near the vortex trajectory observed experimentally. The possible diffusion of these two vortices into each other could account for the appearance of a single vortex in the data.

In figure 16(c), the canard is deflected 10° and the entire configuration is at 10° angle of attack. The canard vortices spiral around each other until they reach the wing leading edge, at which point they are separated by the wing and the trailing vortex passes beneath the wing and moves downward and inboard while the separation vortex moves over the wing and slightly outboard. The lateral position of the separation vortex is in reasonable agreement with the experimental trajectory, but the vertical position is much lower everywhere for unknown reasons. The overall agreement between the predicted and actual vortex trajectories in this case is not good. Combining Γ_l and Γ_t at the trailing edge might help.

The results for the same configuration at supersonic speeds (M = 1.3) are shown in figures 16(d) and (e). In the first of these figures, the canard is undeflected and the configuration is at 5° angle of attack. The predicted lateral position of the canard vortices is in very close agreement with that observed experimentally, but the predicted vertical position is beneath the actual location. In figure 16(e), the canard is deflected 10° and the configuration is at 0° angle of attack. The predicted trajectories pass under the wing while experimental vortices are observed to be above the wing.

The above results for the canard vortex trajectory calculations show generally good agreement with data for lateral positions but the predicted vertical positions are often lower than the observed positions. The wing thickness effects are not included in the trajectory calculations. It appears that the predicted vertical positions are too low for the two cases with canards deflected. In the case of figure 16(c), this effect seems to be an initial condition problem in that the vortices start too low. Possibly the shed separation vortex is higher than the correlation curves indicate and the trailing vortex is not leaving the canard at the trailing edge. Further detailed measurements of vortex trajectories need to be made to answer these and other questions more precisely.

Complete Configurations

Subsonic flow.- The ability of the subsonic prediction method to compute the static longitudinal aerodynamic characteristics of a complete aircraft configuration with interference between the various components is illustrated in figure 17. In the figure, the experimental results on a canard-body-wing configuration (ref. 54) in incompressible flow, $M \approx 0.1$, are compared with predicted characteristics. The results are compared for various stages of interference effects; that is, canard off, canard on, and canard deflected. In each comparison, two sets of theoretical results are presented. The first is the linear solution from reference 2, and the second is the present method which includes vortex lift and vortex interference effects.

In the comparisons between data and the theory of reference 2 it should be borne in mind that the theory of reference 2 is generally valid only up to 10° angle of attack or less for very low aspect ratio wings. In certain cases the data exhibit linear behavior as a function of α for angles of attack much greater than 10°. However, since the theory of reference 2 does not make any prediction concerning the size of the nonlinearities, it does not predict when the behavior will be approximately linear at high angles of attack. It can therefore not be said to predict results beyond $\alpha = 10^{\circ}$ even if they are linear. For this reason the curves based on reference 2 are terminated at about $\alpha = 10^{\circ}$.

The lift and pitching-moment characteristics of the configuration with the canard removed are compared in figure 17(a). The wing leading-edge vortex lift is limited by the factor from figure 6(a), and the predicted lift curve from the lifting-surface method is in good agreement up to 24° angle of attack. The linear lift results are lower than the data because of the vortex lift. The pitching-moment comparisons indicate some inaccuracy in predicting the wing center of pressure with the present method. The predicted center of pressure is too far aft resulting in too much negative moment. The linear results are in better agreement with experiment at low angles of attack.

Part (b) of figure 17 is for the complete configuration with the canard undeflected. The linear prediction method underestimates the lift coefficient, but it does predict the correct trend in the pitching-moment comparisons. The lifting-surface method with limited vortex lift on both the canard ($K^*_{VLE} = 0.53$) and wing ($K^*_{VLE} = 0.41$) is in good agreement with the measured lift curve over the entire angle-of-attack range for which data are available. The pitching-moment curve, including some of the nonlinearities exhibited by the data, is in good agreement over the full range of lift coefficients.

Figure 17(c) corresponds to the complete configuration with the canard deflected 10°. As in previous results, the linear results underpredict the lift coefficient over the entire angle-of-attack range. The linear pitching-moment results show the proper trend, but there appears to be a disagreement in the center-of-pressure location predicted by this method. The nonlinear results from the subsonic lifting-surface method show good agreement with experiment over the total range of angle of attack with the exception of the region around $\alpha = 8^{\circ}$. Near this point there appears to be a discontinuity in the lift curve and the corresponding moment curve. Examination of the details of the prediction method in this area indicate that one of the canard vortices switches from passing under the wing to passing over the wing. During this transition, the vortex passes very near to the wing and to some of the control points in the vortex lattice. The large induced downwash causes a loss in wing loading which causes the dip shown in the figure. The pitching-moment curve behaves erratically in this region because of the large fluctuations in the wing loading. This behavior was discussed in a previous section.

Since the loading changes are caused by large and unrealistic changes in the vortex-induced velocities on the wing control points, a simple remedy is to limit the magnitude of the induced velocities. The vortex model is that of a potential vortex which has a singularity at its center, thus, a vortex coming close to a control point can induce indefinitely large velocities at that point. As described in an earlier section, a simple and approximate improvement in the vortex model is to not let the induced velocity at any point exceed some arbitrary magnitude. This has the effect of smoothing out any loading irregularities associated with a vortex approaching too near a control point. The smoothed theoretical curves in figure 17(c) were obtained using the assumption that none of the vortex-induced velocities could exceed 0.1. The change improved the results considerably. There is still a small dip in the lift curve caused by the vortex passing near the wing, but the character of the dip is smoothed out and agreement with experiment is good over the entire angle-of-attack range.(1) The predicted pitching-moment coefficients are somewhat

---

(1) When the vortex is very close to the wing, it moves rapidly laterally. This motion induces loading on the wing which would have to be accounted for in a more precise analysis than the present one.

more sensitive to vortex interference as the moment curves show larger effects than do the lift curves. Vortex interference causes changes in the distribution of the loading on the wing and thus changes the center-of-pressure location. The net lift on the wing may not be changed appreciably, but a small change in center of pressure can have large effects on the pitching-moment coefficient. As the angle of attack increases, the trailing vortices move farther from the wing and the induced velocities get smaller. Thus, the limitation on the induced velocities has smaller and smaller effect and the predicted curves with and without the limit should approach one another as they do.

The compressibility effects in the subsonic lifting-surface method have been tested by applying the prediction method to a wing-body configuration at high subsonic Mach numbers. The configuration considered is an aspect ratio 2 diamond-shaped wing with a simple body-of-revolution fuselage (ref. 55). The vortex lift on this wing was limited through the use of the $K^*_{v_{LE}}$ factor for a delta wing with the same leading-edge sweep angle. Note that the $K^*_{v_{LE}}$ factors in figure 6(a) were developed from incompressible data. There was not enough subsonic wing-alone data available to develop correlation curves which would be a function of both wing shape and Mach number. The comparisons between experiment and theory are presented in figure 18, and, as before, both the linear results and the lifting-surface results are shown.

In figure 18(a), the predicted lift and pitching-moment coefficients at $M = 0.24$ are compared with experimental results. The linear method is in good agreement for lift at low angles of attack, but underpredicts the lift above 10°. The linear pitching moment is in good agreement over the same range of angle of attack. The nonlinear subsonic method overpredicts the lift curve by a small amount which is due to too large a value for $K^*_{v_{LE}}$. This wing apparently converts less than 30 percent of the leading-edge suction to vortex lift. The pitching moment is in good agreement with experiment up to an angle of attack of approximately 15°. The same configuration at Mach numbers of 0.6 and 0.8 are shown in figures 18(b) and (c), respectively. Similar results are observed except that transonic nonlinearities not accounted for in the present prediction method appear in the data at high angles of attack.

Supersonic flow.- The supersonic method was applied to a complete aircraft configuration consisting of a canard-body-wing combination from reference 56. Both canard and wing are aspect ratio 1.46 delta wings. The experimental results on this configuration at $M = 2.01$ are compared with predicted characteristics with various stages of interference included; that is, canard off, canard on, and canard deflected. As in the subsonic cases, the predicted results from both the linear method and the present method are shown in each comparison.

The lift and pitching-moment characteristics of the configuration with the canard removed are shown in figure 19(a). The linear method with no vortex lift included is in good agreement with experimental results. However, there is reason to believe that this wing is developing very little vortex lift. The correlation curves in figure 9 indicate a suction factor of 0.5 for this wing; but as seen in the lift comparison in figure 19(a), this much vortex lift causes the lift to be overpredicted by a large amount. If the vortex lift is not included in the prediction ($K^{*}_{V_{LE}} = 0$), the prediction is in much better agreement with the lift data. With the wing vortex lift removed, the lifting-surface method predicts lift coefficients slightly higher than the linear method. A small part of the difference between the two methods is due to the vortex-induced normal force on the nose of the configuration and the remainder of the difference is in the lift on the wing in the presence of the body. The pitching-moment results predicted by the present method are in slightly better agreement with experiment than those predicted by the linear method, but above 10° angle of attack the agreement is only fair.

The complete canard-body-wing configuration with canard undeflected is shown in figure 19(b). The comparison between predicted and measured lift coefficient exhibits the same behavior as that described above for the canard-off condition. The pitching-moment nonlinearity at high angles of attack is not well predicted.

Results on the same configuration with the canard deflected 10° are presented in figure 19(c). In its range of validity, the linear theory predicts the lift data very well, but it does not predict the pitching-moment data well. The present theory has been carried out with $K_V^* = 0$. We have also used the limitation that the induced velocities due to the vortices not exceed $0.1\ V$ since the canard vortices cross over the rear lifting surface near $\alpha = 7^{\circ}$. The present prediction method overpredicts the lift at low angles of attack but predicts the low angle pitching-moment results well. It overpredicts the high angle-of-attack pitching-moment coefficients.

The supersonic high-angle prediction method was applied to a second configuration, a wing-body-tail combination from reference 57. This model has a body-of-revolution fuselage with a wing and tail which have very small leading-edge sweep angles. The configuration was tested over a wide range of Mach numbers, but all the supersonic Mach numbers were large enough that the leading edges of both wing and tail are supersonic and, as such, develop no leading-edge suction.

The configuration with the horizontal tail removed is examined in figure 20(a) at Mach numbers 1.30 and 2.22. At the lower Mach number, the high-angle method somewhat overpredicts the experimental lift curve while the linear method predictions are in good agreement. At $M = 2.22$, the lift predicted by both methods is in good agreement with experiment. The predicted pitching-moment coefficients at $M = 1.30$ for both methods differ from the data by an amount corresponding to a shift in the center of pressure amounting to 5 percent of the mean aerodynamic chord. At $M = 2.22$, both methods predict the pitching-moment data fairly well.

Parts (b), (c), and (d) of figure 20 compared the measured and predicted characteristics of the complete configuration with the tail undeflected, deflected -10°, and deflected -20°, respectively. In all cases, the two predicted lift curves are in good agreement with the measured lift characteristics. With tail deflection both methods give the same pitching moment at zero lift, but the experimental values are only two-thirds to three-fourth of the predicted values. The linear theory yields better values of moment-curve slopes than the present method.

CONCLUDING REMARKS

The present report attempts to extend the linear method of prediction of longitudinal characteristics reported in reference 2 to higher angles of attack. In particular, symmetric vortex shedding from the nose of the fuselage and the leading edges and side edges of the lifting surfaces are considered in their influence on the aerodynamic characteristics. Separate computer programs have been written for subsonic and supersonic speeds. Limited comparisons between the predicted and measured characteristics for complete wing-body-tail combinations at subsonic speeds have shown generally good agreement. Similar comparisons for supersonic speeds show generally fair comparison. Many more comparisons need to be made between prediction and experiment to check out the prediction method thoroughly and to make any necessary alterations to improve its accuracy.

The method has certain limitations in its range of applicability. Because symmetrical body-vortex shedding has been assumed, the method is limited in angle-of-attack range. The limiting angle of attack depends principally on nose-fineness ratio as shown in figure 3. Another angle-of-attack limitation is imposed by wing stall since the vortex lift now no longer increases approximately quadratically with angle of attack. For rectangular wings at subsonic speeds, the limiting angle depends on wing aspect ratio as shown in figure 7(b). For delta wings, the limiting angle also depends on aspect ratio or leading-edge sweep angle as shown in figure 6(b) for subsonic speeds and figure 9(b) for supersonic speeds.

As the angle of attack of a swept wing is increased, the position of vortex bursting of the trailing vortices moves upstream towards the trailing edge and crosses the trailing edge at some angle of attack. Above this angle of attack, a loss of lift occurs on the wing due to vortex bursting which becomes progressively larger as the angle of attack increases. Data are available from several investigators on the angle of attack at which vortex bursting occurs at the trailing edge of delta wings tested at low speeds. These data are shown in figure 21. What is significant about these results is that they do not correlate. This suggests that the factors which control vortex bursting were not reproduced between the several sets of test data. If the angle-of-attack limits shown by figure 6(b) are caused by vortex bursting, as is suspected, these data will not correlate unless those factors influencing vortex bursting are properly controlled. The lift and moment data for delta-wing configurations will also show variability from tunnel to tunnel on this basis. A precise determination of the limitation of the present method based on vortex bursting cannot, therefore, be made until better experimental information is available.

As a result of the present work, it has been found that other experimental data would be useful to improve the correlation curves used in the method and to provide a basis for further verification of the method. First of all, the data on delta wing-alone characteristics are meager for high angles of attack in the range of $0.5 < M < 0.9$ and in the supersonic range. The same is true for rectangular wings to a greater degree. There exist no systematic data to indicate experimentally the side-edge suction factor for rectangular wings at supersonic speeds. With regard to the position of separated vortices from leading edges and side edges, the available data are sparse at compressible speeds, both subsonic and supersonic. The effect of wing-body interference on the separation-vortex structure needs experimental study.

With regard to complete wing-body-tail configurations, more data are needed. For instance, more data on vortex trajectories are needed, either based on the vapor screen techniques or more precise methods such as laser anemometry. The effects of canard deflection on the vortex trajectories needs more attention, as well as the interaction between the potential trailing vortices and the leading-edge separation vortices for canards of low aspect ratio. It appears that some attention should also be given to the interaction of vortices with lifting surfaces which they approach closely. Questions of the vortex-core radius need investigation as well as possible vortex bursting. There is also the continuing need for systematic data on the build-up of wing-body-tail combinations at high angles of attack at all speeds.

Further analytical investigation would improve the accuracy of the predictive method. While significant areas in which to expand these efforts should come to light by additional systematic comparison between prediction and data, several areas are already apparent. One of these is the method for predicting the vertical position of the vortices shed by forward lifting surfaces as they move aft over the rear lifting surfaces. Another area is the behavior of a vortex in the close proximity of a lifting surface. The use of a vortex model which includes a core can help reduce the effect of the singularity in upwash associated with a potential vortex model. Also, the method of determining the effect of the vortex on the lifting surface under such conditions should include a force proportional to vortex lateral velocity that is usually ignored. The lateral vortex velocity can become large for close approach because of the image system inside the lifting surface. Also, there is the possibility of inducing vortex breakdown because of axial pressure gradients associated with the proximity of the lifting surface.

Another subject which can stand more precise treatment is that of determining the center-of-pressure location of forces associated with vortex lift. Further work on calculation of vortex trajectories as influenced by a lifting surface not centrally mounted would be useful as well as further consideration of the effects of canard deflection.

In the present model, an attempt has been made to utilize methods which will allow extension of the complete method to other regimes without modification of its basic framework. For instance, it should be possible to extend the method to the case of asymmetric nose vortices. Correlation charts or other means for determining the strength and position of the asymmetric vortices at the beginning of the forward lifting surface would be required. The vortex-lattice method for subsonic speeds or the lifting-surface method for supersonic speeds can then be extended to account for a lack of left-right symmetry on the wing or tail. The same is true of the vortex trajectory prediction method. It is also possible to extend the present methods to conditions of sideslip by virtue of the same considerations. Another area in which the method can be extended is to include the effects of wing stall. This can be accomplished in part by using experimental wing-alone characteristics in the method. However, some unanswered questions exist with regard to formulating a correct vortex model for the wing flow since vortex bursting can be a complicating factor.

APPENDIX A

EQUATIONS OF MOTION OF SEVERAL PAIRS OF VORTICES IN THE PRESENCE OF A WING-BODY COMBINATION

The following sketch shows a pair of body vortices and a pair of wing trailing vortices in the presence of the empennage section of a wing-body-tail combination with centrally mounted tail panel at zero deflection.

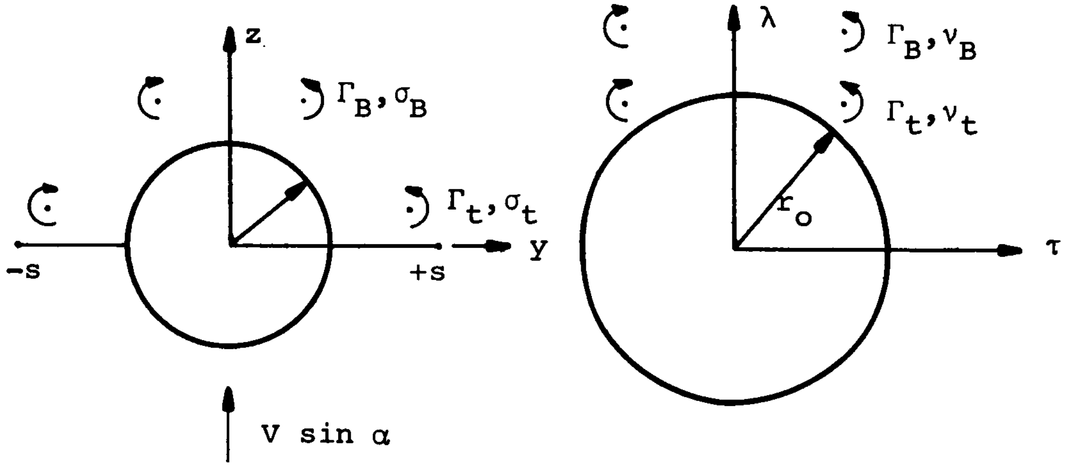

$\sigma = y + iz$ $\qquad\qquad$ $\nu = \tau + i\lambda$

The vortex strengths, Γ_B and Γ_t, are constant and their position, σ_B and σ_t, are to be determined as a function of distance downstream from some initial location.

We transform the wing-body combination into a circle of radius r_o by means of the transformation

$$\sigma + \frac{a^2}{\sigma} = \frac{1}{2}\left(s + \frac{a^2}{s}\right)\left(\frac{\nu}{r_o} + \frac{r_o}{\nu}\right) = \nu + \frac{r_o^2}{\nu} \tag{A-1}$$

where

$$r_o = \frac{1}{2}\left(s + \frac{a^2}{s}\right) \tag{A-2}$$

The transformations are given explicitly by

$$\sigma = \frac{1}{2}\left(\nu + \frac{r_o^2}{\nu}\right) + \frac{1}{2}\sqrt{\left(\nu + \frac{r_o^2}{\nu}\right)^2 - 4a^2} \qquad \text{(A-3)}$$

and

$$\nu = \frac{1}{2}\left(\sigma + \frac{a^2}{\sigma}\right) + \frac{1}{2}\sqrt{\left(\sigma + \frac{a^2}{\sigma}\right)^2 - \left(s + \frac{a^2}{s}\right)^2} \qquad \text{(A-4)}$$

The complex potential for the flow in the ν plane is

$$W(\nu) = -iV \sin\alpha \left(\nu - \frac{r_o^2}{\nu}\right) - \frac{i\Gamma_t}{2\pi} \ln \frac{(\nu - \nu_t)\left(\nu + \frac{r_o^2}{\nu_t}\right)}{(\nu + \bar{\nu}_t)\left(\nu - \frac{r_o^2}{\bar{\nu}_t}\right)}$$

$$- \frac{i\Gamma_B}{2\pi} \ln \frac{(\nu - \nu_B)\left(\nu + \frac{r_o^2}{\nu_B}\right)}{(\nu + \bar{\nu}_B)\left(\nu - \frac{r_o^2}{\bar{\nu}_B}\right)} + r_o V \ln \nu \frac{dr_o}{dx} \qquad \text{(A-5)}$$

In the σ plane the complex potential $W_B(\sigma)$ governing the motion of the right body vortex is

$$W_B(\sigma) = -iV \sin\alpha\left(\nu - \frac{r_o^2}{\nu}\right) - \frac{i\Gamma_1}{2\pi} \ln \frac{(\nu - \nu_1)\left(\nu + \frac{r_o^2}{\nu_1}\right)}{(\nu + \bar{\nu}_1)\left(\nu - \frac{r_o^2}{\bar{\nu}_1}\right)}$$

$$- \frac{i\Gamma_B}{2\pi} \ln \frac{\left(\nu + \frac{r_o^2}{\nu_B}\right)}{(\nu + \bar{\nu}_B)\left(\nu - \frac{r_o^2}{\bar{\nu}_B}\right)} + \frac{i\Gamma_B}{2\pi} \ln \frac{\sigma - \sigma_B}{\nu - \nu_B} + aV \ln \sigma \frac{da}{dx}$$

$$\text{(A-6)}$$

wherein we have simply subtracted the potential in the σ plane due to the right body vortex from the total potential given by equation (A-5). This removes the singularity which would otherwise result in the velocity of that vortex.

We now have the velocity of the right body vortex as

$$v_B - iw_B = \left.\frac{dW_B(\sigma)}{d\sigma}\right|_{\sigma=\sigma_B} \tag{A-7}$$

Let us examine the last term of equation (A-6) first.

$$\lim_{\sigma\to\sigma_B} \left.\frac{d}{d\sigma} \ln \frac{(\sigma - \sigma_B)}{(\nu - \nu_B)}\right|_{\sigma_B} = \lim_{\sigma\to\sigma_B}\left[\frac{1}{\sigma - \sigma_B} - \frac{1}{\nu - \nu_B}\frac{d\nu}{d\sigma}\right]$$

$$= \lim_{\sigma\to\sigma_B}\left[\frac{1}{\nu - \nu_B}\left(\frac{\nu - \nu_B}{\sigma - \sigma_B} - \frac{d\nu}{d\sigma}\right)\right] \tag{A-8}$$

In the neighborhood of σ_B

$$\nu - \nu_B = (\sigma - \sigma_B)\left.\frac{d\nu}{d\sigma}\right|_{\sigma_B} + \frac{1}{2}(\sigma - \sigma_B)^2\left.\frac{d^2\nu}{d\sigma^2}\right|_{\sigma_B} + \ldots \tag{A-9}$$

$$\frac{d\nu}{d\sigma} = \left.\frac{d\nu}{d\sigma}\right|_{\sigma_B} + (\sigma - \sigma_B)\left.\frac{d^2\nu}{d\sigma^2}\right|_{\sigma_B} + \ldots \tag{A-10}$$

Thus, the argument of equation (A-8) becomes

$$\frac{1}{(\nu - \nu_B)}\left(\frac{\nu - \nu_B}{\sigma - \sigma_B} - \frac{d\nu}{d\sigma}\right) = \frac{1}{\nu - \nu_B}\left[\left.\frac{d\nu}{d\sigma}\right|_{\sigma_B} + \frac{1}{2}(\sigma - \sigma_B)\left.\frac{d^2\nu}{d\sigma^2}\right|_{\sigma_B}\right.$$

$$\left. - \left.\frac{d\nu}{d\sigma}\right|_{\sigma_B} - (\sigma - \sigma_B)\left.\frac{d^2\nu}{d\sigma^2}\right|_{\sigma_B} + O(\sigma - \sigma_B)^2\right]$$

and

$$\lim_{\substack{\sigma\to\sigma_B \\ \nu\to\nu_B}} \left(\frac{1}{\nu - \nu_B}\right)\left(\frac{\nu - \nu_B}{\sigma - \sigma_B} - \frac{d\nu}{d\sigma}\right) = -\frac{1}{2}\,\frac{d\sigma}{d\nu}\,\frac{d^2\nu}{d\sigma^2}\bigg|_{\sigma_B} \qquad \text{(A-11)}$$

Since the transformation is analytic at σ_B except for a few exceptional points, we find a finite contribution from the last term of equation (A-6) to the body-vortex velocity.

It is now possible to express the body-vortex velocity in the following complex form.

$$\begin{aligned} v_B - iw_B = \frac{d}{d\nu}\Bigg\{ & -iV\sin\alpha\left(\nu - \frac{r_o^2}{\nu}\right) - \frac{i\Gamma_t}{2\pi}\ln\frac{(\nu - \nu_t)\left(\nu + \frac{r_o^2}{\nu_t}\right)}{(\nu + \bar{\nu}_t)\left(\nu - \frac{r_o^2}{\bar{\nu}_t}\right)} \\ & - \frac{i\Gamma_B}{2\pi}\ln\frac{\left(\nu + \frac{r_o^2}{\nu_B}\right)}{(\nu + \bar{\nu}_B)\left(\nu - \frac{r_o^2}{\bar{\nu}_B}\right)}\Bigg\}\frac{d\nu}{d\sigma} \\ & - \frac{i\Gamma_B}{2\pi}\,\frac{1}{2}\,\frac{d\sigma}{d\nu}\,\frac{d^2\nu}{d\sigma^2} + \frac{r_o}{\nu_n}\,\frac{dr_o}{dx}\,\frac{d\nu}{d\sigma} \end{aligned} \qquad \text{(A-12)}$$

Equation (A-12) is evaluated at $\sigma = \sigma_B$, and the last term is the effect of a changing body radius. Assume the following form for equation (A-12).

$$\frac{v_B - iw_B}{V} = G_{C_B} + G_{tB} + G^{*}_{BB} + G_{T_B} \qquad \text{(A-13)}$$

This equation can be rewritten in the general form

$$\frac{v_n - iw_n}{V} = G_{C_n} + \underbrace{\sum_n \sum_m G_{mn}}_{n \neq m} + G^*_{nn} + G_{T_n} \tag{A-14}$$

where the subscript n denotes the vortex under consideration and the subscript m denotes the vortex causing the motion. Each term in equation (A-14) can now be evaluated. Generally, the complex quantities will be expressed in terms of ν plane quantities. From equation (A-4)

$$\left.\frac{d\nu}{d\sigma}\right|_{\sigma_n} = \frac{2\left(\frac{\nu_n}{r_o}\right)^2 \left[\left(\frac{\nu_n}{r_o} + \frac{r_o}{\nu_n}\right)^2 - \left(\frac{2a}{r_o}\right)^2\right]^{1/2}}{\left[\left(\frac{\nu_n}{r_o}\right)^2 - 1\right]\left\{\left(\frac{\nu_n}{r_o} + \frac{r_o}{\nu_n}\right) + \left[\left(\frac{\nu_n}{r_o} + \frac{r_o}{\nu_n}\right)^2 - \left(\frac{2a}{r_o}\right)^2\right]^{1/2}\right\}} \tag{A-15}$$

The first term of equation (A-14) is the body-interference effect and it is made up of a part representing the body in a crossflow and a part representing the change in body radius with axial position.

$$G_{C_n} = -i \frac{\left(\frac{\nu_n}{r_o}\right)^2 + 1}{\left(\frac{\nu_n}{r_o}\right)^2} \sin\alpha \left.\frac{d\nu}{d\sigma}\right|_{\sigma_n} + \frac{r_o}{\nu_n}\frac{dr_o}{dx}\cos\alpha \left.\frac{d\nu}{d\sigma}\right|_{\sigma_n} \tag{A-16}$$

The second term in equation (A-14) is the influence of all other vortices and their images on the vortex in question. Thus, for $n \neq m$,

$$G_{mn} = -\frac{i\Gamma_m}{2\pi V}\left[\frac{1}{\nu_n - \nu_m} + \frac{1}{\nu_n + \frac{r_o^2}{\nu_m}} - \frac{1}{\nu_n + \bar{\nu}_m} - \frac{1}{\nu_n - \frac{r_o^2}{\bar{\nu}_m}}\right]\left.\frac{d\nu}{d\sigma}\right|_{\sigma_n}$$

(Continued on next page)

$$= -i\left(\frac{\Gamma_m}{2\pi V a}\right)\left(\frac{a}{r_o}\right)\left[\frac{1}{\frac{\nu_n}{r_o} - \frac{\nu_m}{r_o}} + \frac{1}{\frac{\nu_n}{r_o} + \frac{r_o}{\nu_m}} - \frac{1}{\frac{\nu_n}{r_o} + \frac{\bar{\nu}_m}{r_o}} - \frac{1}{\frac{\nu_n}{r_o} - \frac{r_o}{\bar{\nu}_m}}\right]\frac{d\nu}{d\sigma}\bigg|_{\sigma_n} \tag{A-17}$$

The influence of the opposite vortex and the images of the vortex being considered is represented by the third term.

$$G^*_{nn} = -i\left(\frac{\Gamma_n}{2\pi V}\right)\left[\frac{1}{\nu + \frac{r_o^2}{\nu_n}} - \frac{1}{\nu + \bar{\nu}_n} - \frac{1}{\nu - \frac{r_o^2}{\bar{\nu}_n}}\right]\frac{d\nu}{d\sigma}\ ;\ \sigma = \sigma_n$$

$$= -i\left(\frac{\Gamma_B}{2\pi V a}\right)\left(\frac{a}{r_o}\right)\left[\frac{1}{\frac{\nu_n}{r_o} + \frac{r_o}{\nu_n}} - \frac{1}{\frac{\nu_n}{r_o} + \frac{\bar{\nu}_n}{r_o}} - \frac{1}{\frac{\nu_n}{r_o} - \frac{r_o}{\bar{\nu}_n}}\right]\frac{d\nu}{d\sigma}\bigg|_{\sigma_n} \tag{A-18}$$

The last term in equation (A-14) is a result of the transformation and can be expressed as follows.

$$G_{T_n} = -i\left(\frac{\Gamma_n}{2\pi V}\right)\frac{1}{2}\,\frac{d\sigma}{d\nu}\,\frac{d^2\nu}{d\sigma^2}\ ;\ \sigma = \sigma_n \tag{A-19}$$

where

$$\frac{d\sigma}{d\nu}\,\frac{d^2\nu}{d\sigma^2} = \frac{d\sigma}{d\nu}\,\frac{d}{d\sigma}\left(\frac{d\nu}{d\sigma}\right) = \frac{d\sigma}{d\nu}\,\frac{d\nu}{d\sigma}\,\frac{d}{d\nu}\left(\frac{d\nu}{d\sigma}\right) = \frac{d}{d\nu}\left(\frac{d\nu}{d\sigma}\right) \tag{A-20}$$

With the help of equation (A-15)

$$\frac{d\sigma}{d\nu}\,\frac{d^2\nu}{d\sigma^2} = \frac{d}{d\nu}\left[\left(\frac{2\nu^2}{\nu^2 - r_o^2}\right)\frac{R}{\left(\nu + \frac{r_o^2}{\nu}\right) + R}\right]$$

where

$$R = \sqrt{\left(\nu + \frac{r_o^2}{\nu}\right)^2 - 4a^2} \qquad \text{(A-21)}$$

Now we can write

$$\frac{d}{d\nu}\left(\frac{2\nu^2}{\nu^2 - r_o^2}\right) = \frac{-4\nu r_o^2}{(\nu^2 - r_o^2)^2} \qquad \text{(A-22)}$$

$$\frac{d}{d\nu}\left[\frac{R}{\left(\nu + \frac{r_o^2}{\nu}\right) + R}\right] = \frac{(\nu^2 - r_o^2)\left(\nu + \frac{r_o^2}{\nu} - R\right)}{\nu^2 R\left(\nu + \frac{r_o^2}{\nu} + R\right)} \qquad \text{(A-23)}$$

so that

$$\frac{d\sigma}{d\nu}\,\frac{d^2\nu}{d\sigma^2} = \frac{-4\nu r_o^2 R}{(\nu^2 - r_o^2)^2\left(\nu + \frac{r_o^2}{\nu} + R\right)} + \frac{2\left(\nu + \frac{r_o^2}{\nu} - R\right)}{\left(\nu + \frac{r_o^2}{\nu} + R\right)R}$$

$$= \frac{2}{\left(\nu + \frac{r_o^2}{\nu} + R\right)}\left[\frac{\nu + \frac{r_o^2}{\nu}}{R} - 1 - \frac{2\nu r_o^2 R}{(\nu^2 - r_o^2)^2}\right] \qquad \text{(A-24)}$$

Thus

$$G_{T_n} = -i\left(\frac{\Gamma_n}{2\pi V a}\right)\left(\frac{a}{r_o}\right)\left[\frac{1}{\left(\frac{\nu_n}{r_o} + \frac{r_o}{\nu_n}\right) + \sqrt{\left(\frac{\nu_n}{r_o} + \frac{r_o}{\nu_n}\right)^2 - \frac{4a^2}{r_o^2}}}\right]$$

(Continued on next page)

$$\left[\frac{\dfrac{\nu_n}{r_o} + \dfrac{r_o}{\nu_n}}{\sqrt{\left(\dfrac{\nu_n}{r_o} + \dfrac{r_o}{\nu_n}\right)^2 - \dfrac{4a^2}{r_o^2}}} - 1 - \frac{2\left(\dfrac{\nu_n}{r_o}\right)\sqrt{\left(\dfrac{\nu_n}{r_o} + \dfrac{r_o}{\nu_n}\right)^2 - \dfrac{4a^2}{r_o^2}}}{\left(\dfrac{\nu_n^2}{r_o^2} - 1\right)^2}\right] \tag{A-25}$$

This completes the information required to compute the complex velocity of one of the free vortices.

In the case of a wing or tail not centrally mounted on the fuselage, the value of $d\nu/d\sigma$ must be changed. This modification has not been included in the present analysis.

APPENDIX B

CROSSFLOW VELOCITIES INDUCED BY A FREE VORTEX AND A CIRCULAR CYLINDER AT ANGLE OF ATTACK

Consider a circular cylinder at angle of attack α with a pair of vortices with mirror symmetry.

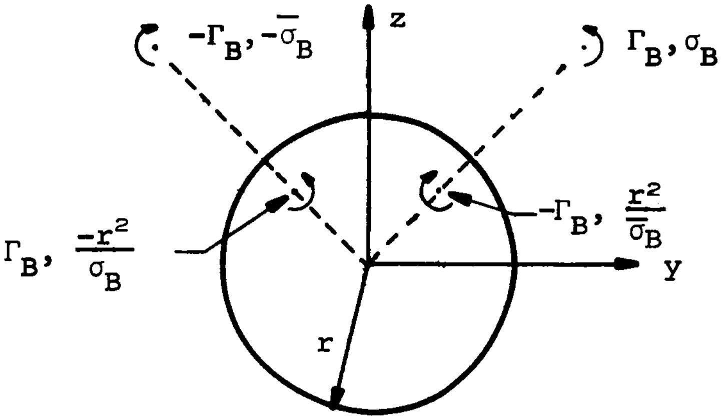

$\sigma = y + iz$

The right vortex of strength Γ_B is located at

$$\sigma_B = y_B + iz_B \tag{B-1}$$

The complex potential for the flow is known to be

$$W(\sigma) = -iV \sin \alpha\left(\sigma - \frac{r^2}{\sigma}\right) - \frac{i\Gamma_B}{2\pi} \ln \frac{(\sigma - \sigma_B)\left(\sigma + \frac{r^2}{\sigma_B}\right)}{(\sigma + \bar{\sigma}_B)\left(\sigma - \frac{r^2}{\bar{\sigma}_B}\right)} \tag{B-2}$$

$$v - iw = \frac{dW}{d\sigma} = -iV \sin \alpha\left(1 + \frac{r^2}{\sigma^2}\right)$$

$$- \frac{i\Gamma_B}{2\pi}\left[\frac{1}{\sigma - \sigma_B} + \frac{1}{\sigma + \frac{r^2}{\sigma_B}} - \frac{1}{\sigma + \bar{\sigma}_B} - \frac{1}{\sigma - \frac{r^2}{\bar{\sigma}_B}}\right] \tag{B-3}$$

At any point $y + iz$ the velocity can be put into nondimensional form, only the vertical velocity w being of interest.

$$\frac{w}{V} = \sin \alpha \ \text{Real}\left(1 + \frac{r^2}{\sigma^2}\right) + \frac{\Gamma_B}{2\pi V r} \ \text{Real}\left[\frac{r}{\sigma - \sigma_B} + \frac{r}{\sigma + \frac{r^2}{\sigma_B}} - \frac{r}{\sigma + \bar{\sigma}_B} - \frac{r}{\sigma - \frac{r^2}{\bar{\sigma}_B}}\right] \tag{B-4}$$

$$\text{Real}\left(1 + \frac{r^2}{\sigma^2}\right) = 1 + \frac{\left(\frac{y^2}{r^2} - \frac{z^2}{r^2}\right)}{\left(\frac{y^2}{r^2} + \frac{z^2}{r^2}\right)^2} \tag{B-5}$$

$$\text{Real}\left(\frac{r}{\sigma - \sigma_B}\right) = \frac{\left(\frac{y - y_B}{r}\right)}{\left(\frac{y - y_B}{r}\right)^2 + \left(\frac{z - z_B}{r}\right)^2} \tag{B-6}$$

$$\text{Real}\left(\frac{r}{\sigma + \frac{r^2}{\sigma_B}}\right) = \frac{\left(\frac{y}{r} + \frac{r y_B}{y_B^2 + z_B^2}\right)}{\left(\frac{y}{r} + \frac{r y_B}{y_B^2 + z_B^2}\right)^2 + \left(\frac{z}{r} - \frac{r z_B}{y_B^2 + z_B^2}\right)} \tag{B-7}$$

$$\text{Real}\left(\frac{r}{\sigma + \bar{\sigma}_B}\right) = \frac{\left(\frac{y}{r} + \frac{y_B}{r}\right)}{\left(\frac{y}{r} + \frac{y_B}{r}\right)^2 + \left(\frac{z}{r} - \frac{z_B}{r}\right)^2} \tag{B-8}$$

$$\text{Real}\left(\frac{r}{\sigma - \frac{r^2}{\bar{\sigma}_B}}\right) = \frac{\left(\frac{y}{r} - \frac{r y_B}{y_B^2 + z_B^2}\right)}{\left(\frac{y}{r} - \frac{r y_B}{y_B^2 + z_B^2}\right)^2 + \left(\frac{z}{r} - \frac{r z_B}{y_B^2 + z_B^2}\right)^2} \tag{B-9}$$

The vertical velocity in the crossflow plane is thus

$$
\begin{aligned}
\frac{w}{V} = \sin\alpha & \left[1 + \frac{\left(\frac{y^2}{r^2} - \frac{z^2}{r^2}\right)}{\left(\frac{y^2}{r^2} + \frac{z^2}{r^2}\right)^2} \right] + \left(\frac{\Gamma_B}{2\pi V r}\right) \left\{ \frac{\left(\frac{y - y_B}{r}\right)}{\left(\frac{y - y_B}{r}\right)^2 + \left(\frac{z - z_B}{r}\right)^2} \right. \\
& + \frac{\left(\frac{y}{r} + \frac{r y_B}{y_B^2 + z_B^2}\right)}{\left(\frac{y}{r} + \frac{r y_B}{y_B^2 + z_B^2}\right)^2 + \left(\frac{z}{r} - \frac{r z_B}{y_B^2 + z_B^2}\right)^2} - \frac{\left(\frac{y}{r} + \frac{y_B}{r}\right)}{\left(\frac{y + y_B}{r}\right)^2 + \left(\frac{z - z_B}{r}\right)^2} \\
& \left. - \frac{\left(\frac{y}{r} - \frac{r y_B}{y_B^2 + z_B^2}\right)}{\left(\frac{y}{r} - \frac{r y_B}{y_B^2 + z_B^2}\right)^2 + \left(\frac{z}{r} - \frac{r z_B}{y_B^2 + z_B^2}\right)^2} \right\} \qquad \text{(B-10)}
\end{aligned}
$$

REFERENCES

1. Polhamus, E. C.: Prediction of Vortex-Lift Characteristics Based on a Leading-Edge Suction Analogy. AIAA Paper No. 69-1133, Oct. 20, 1969. (Jour. of Aircraft, vol. 8, no. 4, Apr. 1971, pp. 193-199)

2. Pitts, W. C., Nielsen, J. N., and Kaattari, G. E.: Lift and Center of Pressure of Wing-Body-Tail Combinations at Subsonic, Transonic, and Supersonic Speeds. NACA Rept. 1307, 1957.

3. Jorgensen, L. H.: Prediction of Static Aerodynamic Characteristics for Space-Shuttle-Like and Other Bodies at Angles of Attack From 0° to 180°. NASA TN D-6996, Jan. 1973.

4. Jorgensen, L. H.: A Method for Estimating Static Aerodynamic Characteristics for Slender Bodies of Circular and Noncircular Cross Section Alone and With Lifting Surfaces at Angles of Attack From 0° to 90°. NASA TN D-7228, Apr. 1973.

5. Mendenhall, M. R., Goodwin, F. K., Dillenius, M. F. E., and Kline, D. M.: Computer Programs for Calculating the Static Longitudinal Aerodynamic Characteristics of Wing-Body-Tail Configurations. NEAR TR 70, May 1974; NASA CR 2474, 1974.

6. Jorgensen, L. H. and Perkins, E. W.: Investigation of Some Wake Vortex Characteristics of an Inclined Ogive-Cylinder Body at Mach Number 2. NACA Rept. 1371, 1958.

7. Dunn, Eldon L.: A Low-Speed Experimental Study of Yaw Forces on Bodies of Revolution at Large Angles of Pitch and Zero Angle of Sideslip. NOTS TM-1588, Mar. 1954.

8. Pick, George S.: Investigation of Side Forces on Ogive-Cylinder Bodies at High Angles of Attack in the $M = 0.5$ to 1.1 Range. AIAA 4th Fluid and Plasma Dynamics Conference, Palo Alto, CA, June 21-23, 1971, AIAA Paper No. 71-570.

9. Gowen, Forrest E. and Perkins, Edward W.: A Study of the Effects of Body Shape on the Vortex Wakes of Inclinded Bodies at a Mach Number of 2. NACA RM A53I17, Dec. 1953.

10. Tinling, Bruce E. and Allen, Clyde Q.: An Investigation of the Normal-Force and Vortex-Wake Characteristics of an Ogive-Cylinder Body at Subsonic Speeds. NASA TN D-1297, Apr. 1962.

11. Mello, J. F.: Investigation of Normal Force Distributions and Wake Vortex Characteristics of Bodies of Revolution at Supersonic Speeds. Jour. of Aero. Sci., vol. 26, no. 3, Mar. 1959, pp. 155-168.

12. Raney, D. J.: Measurement of the Cross Flow Around an Inclinded Body at a Mach Number of 1.91. Royal Aircraft Establishment RAE TN Aero. 2357 1955.

13. Schindel, Leon H. and Chamberlain, Thomas E.: Vortex Separation on Slender Bodies of Elliptic Cross Section. MIT Tech. Rept. 138, Aug. 1967.

14. Coe, Paul L., Jr., Chambers, Joseph R., and Letko, William: Asymmetric Lateral-Directional Characteristics of Pointed Bodies of Revolution at High Angles of Attack. NASA TN D-7095, Nov. 1972.

15. Spencer, Bernard, Jr., and Phillips, W. Pelham: Transonic Aerodynamic Characteristics of a Series of Bodies Having Variations in Fineness Ratio and Cross-Sectional Ellipticity. NASA TN D-2622, Feb. 1965.

16. Ferris, James C.: Static Stability Investigation of a Single-Stage Sounding Rocket at Mach Numbers from 0.60 to 1.20. NASA TN D-4013, June 1967.

17. Cooper, Morton, Gapcynski, John P., and Hasel, Lowell E.: A Pressure Distribution Investigation of a Fineness-Ratio-12.2 Parabolic Body of Revolution (NACA RM-10) at $M = 1.59$ and Angles of Attack up to 36°. NACA RM L52G14a, Oct. 1952.

18. Chamberlain, Thomas E.: Aerodynamic Forces, Separation Lines, and Vortex Trajectories on Slender Bodies with Several Nose Shapes. Thesis, Mass. Inst. of Tech., June 1966.

19. Hill, Jacques, A. F.: A Non-Linear Theory of the Lift on Slender Bodies of Revolution. Presented at U. S. Navy Symposium on Aeroballistics, Laurel, MD, Oct. 19-20, 1954.

20. Rodgers, E. J.: Real Flow Over a Body of Revolution at Angle of Attack. Pennsylvania State Univ. Ordnance Research Lab. Tech.Memo, File No. TM 5.2420-13, Mar. 28, 1963.

21. Jorgensen, Leland H. and Perkins, Edward W.: Investigation of Some Wake Vortex Characteristics of an Inclined Ogive-Cylinder Body at Mach Number 1.98. NACA RM A55E31, Aug. 1955.

22. Jorgensen, Leland H.: Inclinded Bodies of Various Cross Sections at Supersonic Speeds. NASA Memo 10-3-58A, Nov. 1958.

23. Letko, William: A Low-Speed Experimental Study of the Directional Characteristics of a Sharp-Nosed Fuselage Through a Large Angle-of-Attack Range at Zero Angle of Sideslip. NACA TN-2911, Mar. 1953.

24. Sacks, Alvin, H.: Vortex Interference on Slender Airplanes. NACA TN-3525, Nov. 1955.

25. Dillenius, M. F. E., Mendenhall, M. R., and Spangler, S. B.: Calculation of the Longitudinal Aerodynamic Characteristics of STOL Aircraft with Externally-Blown Jet-Augmented Flaps. NASA CR-2358, Feb. 1974.

26. Mook, D. T. and Maddox, S. A.: Extension of a Vortex-Lattice to Include the Effects of Leading-Edge Separation. Jour. of Aircraft, vol. 11, no. 2, Feb. 1974, pp. 127-128.

27. Polhamus, E. C.: Charts for Predicting the Subsonic Vortex-Lift Characteristics of Arrow, Delta, and Diamond Wings. NASA TN D-6243, Apr. 1971.

28. Rose, L. M.: Low-Speed Investigation of a Small Triangular Wing of Aspect Ratio 2.0. I.- The Effect of Combination with a Body of Revolution and Height Above a Ground Plane. NACA RM A7K03, Aug. 1948.

29. Wentz, W. H., Jr.and Kohlman, D. L.: Wind-Tunnel Investigation of Vortex Breakdown on Slender Sharp-Edged Wings. NASA CR-98737, 1968.

30. Barlett, G. E. and Vidal, R. J.: Experimental Investigation of Influence of Edge Shape on the Aerodynamic Characteristics of Low-Aspect-Ratio Wings at Low Speeds. Jour. of Aero. Sci., vol. 22, no. 8, Aug. 1955, p. 517.

31. Winter, H.: Flow Phenomena on Plates and Airfoils of Short Span. NACA TM-798, July 1936.

32. Peckham, D. H.: Low-Speed Wind-Tunnel Tests on a Series of Uncambered Slender Pointed Wings with Sharp Edges. R & M No. 3186, Brit. A. R. C., 1958.

33. Lange/Wacke: Test Report on Three- and Six-Component Measurements on a Series of Tapered Wings of Small Aspect Ratio. NACA TM-1176, May 1948.

34. Wentz, W. H., Jr.: Effects of Leading-Edge Camber on Low-Speed Characteristics of Slender Delta Wings. NASA CR-2002, Oct. 1972.

35. Lee, G. H.: Note on the Flow Around Delta Wings with Sharp Leading Edges. ARC RM-3070, 1955.

36. Tosti, L. P.: Low Speed Static Stability and Damping-In-Roll Characteristics of Some Swept and Unswept Low-Aspect-Ratio Wings. NACA TN-1468, Oct. 1947.

37. Graham, D.: Chordwise and Spanwise Loading Measured at Low Speeds on a Large Triangular Wing Having an Aspect Ratio of 2 and a Thin, Subsonic-Type Airfoil Section. NACA RM A50A04a, Mar. 1950.

38. Graham, D. and Koenig, D. G.: Tests in the Ames 40- by 80-Foot Wind Tunnel of an Airplane Configuration with an Aspect Ratio 2 Triangular Wing and an All-Movable Horizontal Tail-Longitudinal Characteristics. NACA RM A51B21, Apr. 1951.

39. Graham, D. and Koenig, D. G.: Tests in the Ames 40- by 80-Foot Wind Tunnel of an Airplane Configuration with an Aspect Ratio 4 Triangular Wing and an All-Movable Horizontal Tail-Longitudinal Characteristics. NACA RM A51H10a, Oct. 1951.

40. Bradley, R. G., Smith, C. W., Bhateley, I. C.: Vortex-Lift Prediction for Complex Wing Planforms. Jour. of Aircraft, vol. 10, no. 6, June 1973, pp. 379-381.

41. Ermolenko, S. D.: Nonlinear Theory of Small Aspect Ratio Wings. Soviet Aeronautics, vol. 9, no. 2, 1966.

42. Michael, W. H., Jr.: Flow Studies in the Vicinity of a Modified Flat Plate Rectangular Wing in Aspect Ratio 0.25. NACA TN-2790, June 1952.

43. Jones, G. W., Jr.: Investigation of the Effects of Variation in the Reynolds Number Between 0.4×10^6 and 3.0×10^6 on the Low-Speed Aerodynamic Characteristics of Three Low-Aspect-Ratio Symmetrical Wings with Rectangular Planforms. NACA RM L52G18, Sept. 1952.

44. Elle, B. J.: An Investigation at Low Speeds of the Flow Near the Apex of Thin Delta Wings with Sharp Leading Edges. ARC Rept. 19780, Jan. 1958.

45. Bergesen, A. J. and Porter, J. D.: An Investigation of the Flow Around Slender Delta Wings with Leading-Edge Separation. Princeton University, A.E. Rept. No. 510, May 1960.

46. Woodward, F. A. and Larson, J. W.: A Method of Optimizing Camber Surfaces for Wing-Body Combinations at Supersonic Speeds. Part I - Theory and Application. Doc. D-610741, Pt. I, The Boeing Co., 1965.

47. Carmichael, R. L. and Woodward, F. A.: An Integrated Approach to the Analysis and Design of wings and Wing-Body Combinations in Supersonic Flow. NASA TN D-3685, Oct. 1966.

48. Squire, L. C.: The Estimation of the Non-Linear Lift of Delta Wings at Supersonic Speeds. Jour. Royal Aero. Soc., vol. 67, Aug. 1963.

49. Hill, W. A., Jr.: Experimental Lift of Low-Aspect-Ratio Triangular Wings at Large Angles of Attack and Supersonic Speeds. NACA RM A57I17, Nov. 1957.

50. Lampert, S.: Aerodynamic Force Characteristics of Delta Wings at Supersonic Speed. CIT/JPL Rept. No. 20-82, Sept. 1954.

51. Nielsen, J. N.: Missile Aerodynamics. McGraw-Hill Book Co., Inc., 1960.

52. Lemaire, D. A.: Some Observations of the Low-Speed Flow Over a Sharp-Edged Delta Wing of Unit Aspect Ratio. WPAFB Aerospace Research Labs, ARL/A Rept. 126, June 1965.

53. Peterson, V. L. and Menees, G. P.: Aerodynamic Loads at Mach Numbers From 0.70 to 2.22 on an Airplane Model Having a Wing and Canard of Triangular Plan Form and Either Single or Twin Vertical Tails. NASA TN D-690, June 1961.

54. Brady, J. A., Page, R. V., and Koenig, D. G.: Large-Scale Low-Speed Wind-Tunnel Test of a Delta Winged Supersonic Transport Model with a Delta Canard Control Surface. NASA TM X-643, Jan. 1962.

55. Smith, D. W. and Reed, V. D.: Subsonic Static Longitudinal Stability and Control Characteristics of a Wing-Body Combination Having Pointed Wing of Aspect Ratio 2 with Constant-Percent-Chord Trailing-Edge Elevons. NACA RM A53C20, May 1953.

56. Driver, C.: Effects of Wing Height on the Stability and Control Characteristics at Mach Number of 2.01 of a Canard Airplane Configuration With a 70° Delta Wing. NASA TM X-328, Sept. 1960.

57. Peterson, V. L., and Menees, G. P.: Static Longitudinal Stability and Control Characteristics of an Unswept Wing nad Unswept Horizontal-Tail Configuration at Mach Numbers 0.70 to 2.22. NASA MEMO 6-11-59A, May 1959.

58. Hummel, D. and Redeker, G.: Über den Einfluss des Aufplatzens der Wirbel auf die aerodynamischen Beiwerte von Deltaflügeln mit kleinem Seitenverhältnis beim Schiebeflug, Jahrbuch der WGLR, 1967.

59. Earnshaw, P. B. and Lawford, J. A.: Low Speed Wind-Tunnel Experiments on a Series of Sharp-Edged Delta Wings. Part 1 - Forces, Moments, Normal-Force Fluctuations and Positions of Vortex Breakdown. RAE TN-2780, 1961.

60. Chigier, Norman A.: Measurements of Vortex Breakdown Over a Delta Wing Using a Laser Anemometer. NEAR TR 62, Jan. 1974.

61. Keener, E. R. and Chapman, G. T.: Onset of Aerodynamic Side Forces at Zero Sideslip on Symmetric Forebodies at High Angles of Attack. AIAA Paper No. 74-770, Aug. 5, 1974.

62. Lamar, J. E.: Extension of the Leading Edge Suction Analogy to Wings with Separated Flow Around the Side Edges at Subsonic Speeds. NASA TR R-428, 1974.

COMPONENTS	TYPE	NORMAL-FORCE COEFFICIENT	LIFT COEFFICIENT	PITCHING-MOMENT COEFFICIENT	CENTER OF PRESSURE LOCATION	AXIAL-FORCE COEFFICIENT
NOSE	Potential	$C_{N_{N,p}}$	$C_{L_{N,p}}$	$C_{m_{N,p}}$	$\bar{x}_{N,p}$	--------
	Viscous	$C_{N_{N,v}}$	$C_{L_{N,v}}$	$C_{m_{N,v}}$	$\bar{x}_{N,v}$	--------
WING IN PRESENCE OF BODY	Potential	$C_{N_{W(B),p}}$	$C_{L_{W(B),p}}$	$C_{m_{W(B),p}}$	$\bar{x}_{W(B),p}$	$C_{A_{W(B),p}}$
	Viscous	$C_{N_{W(B),v}}$	$C_{L_{W(B),v}}$	$C_{m_{W(B),v}}$	$\bar{x}_{W(B),v}$	$C_{A_{W(B),v}}$
BODY IN PRESENCE OF WING	Potential	$C_{N_{B(W),p}}$	$C_{L_{B(W),p}}$	$C_{m_{B(W),p}}$	$\bar{x}_{B(W),p}$	--------
	Viscous	$C_{N_{B(W),v}}$	$C_{L_{B(W),v}}$	$C_{m_{B(W),v}}$	$\bar{x}_{B(W),v}$	--------
AFTERBODY	-------	C_{N_A}	C_{L_A}	C_{m_A}	$\bar{x}_A$	--------
TAIL IN PRESENCE OF BODY	Potential	$C_{N_{T(B),p}}$	$C_{L_{T(B),p}}$	$C_{m_{T(B),p}}$	$\bar{x}_{T(B),p}$	$C_{A_{T(B),p}}$
	Viscous	$C_{N_{T(B),v}}$	$C_{L_{T(B),v}}$	$C_{m_{T(B),v}}$	$\bar{x}_{T(B),v}$	$C_{A_{T(B),v}}$
BODY IN PRESENCE OF TAIL	Potential	$C_{N_{B(T),p}}$	$C_{L_{B(T),p}}$	$C_{m_{B(T),p}}$	$\bar{x}_{B(T),p}$	--------
	Viscous	$C_{N_{B(T),v}}$	$C_{L_{B(T),v}}$	$C_{m_{B(T),v}}$	$\bar{x}_{B(T),v}$	--------
COMPLETE CONFIGURATION	-------	C_N	C_L	C_m	$\bar{x}$	C_A

Table I.- Summary of force and moment coefficient notation.

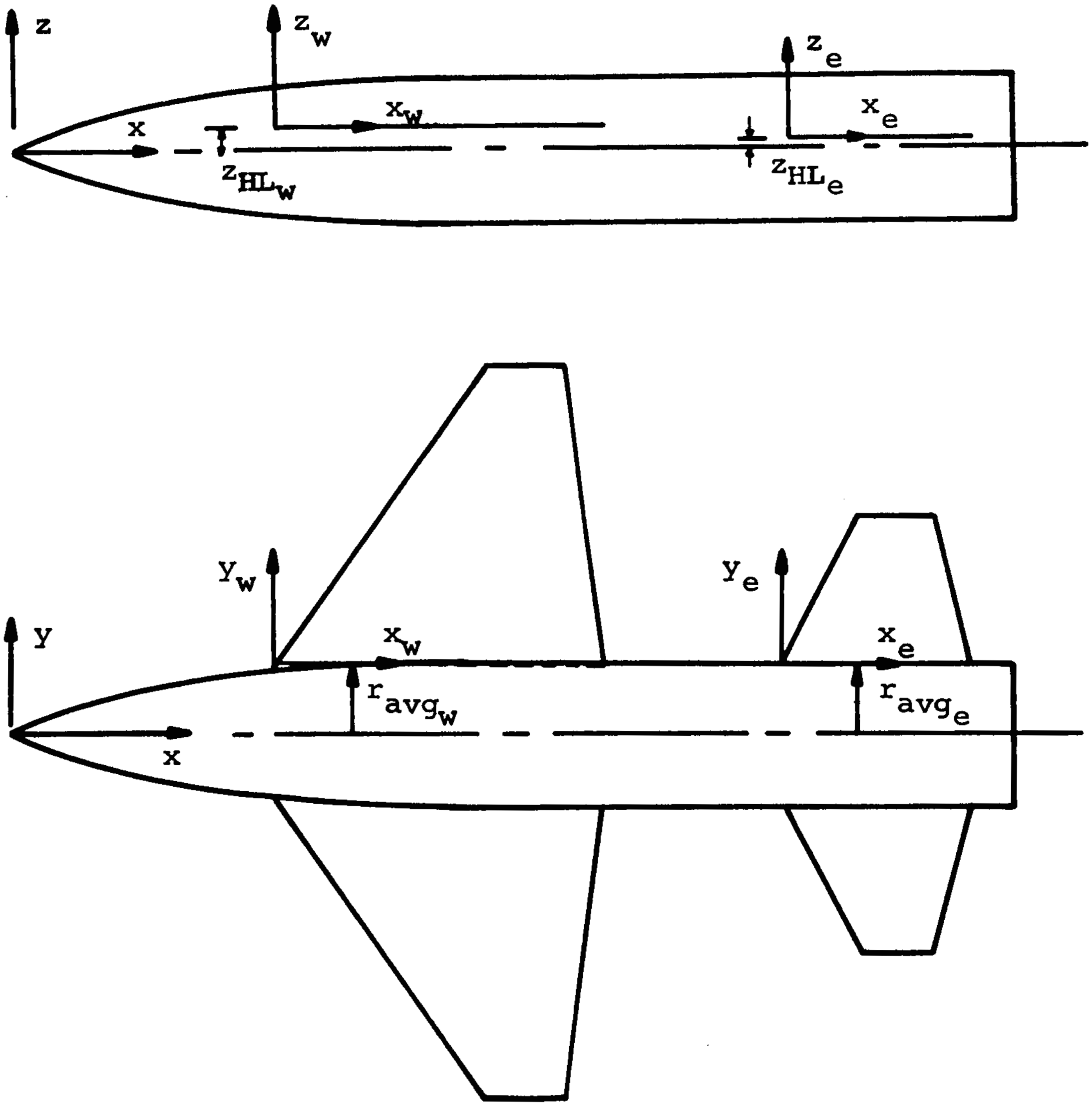

Figure 1.- Configuration coordinate systems.

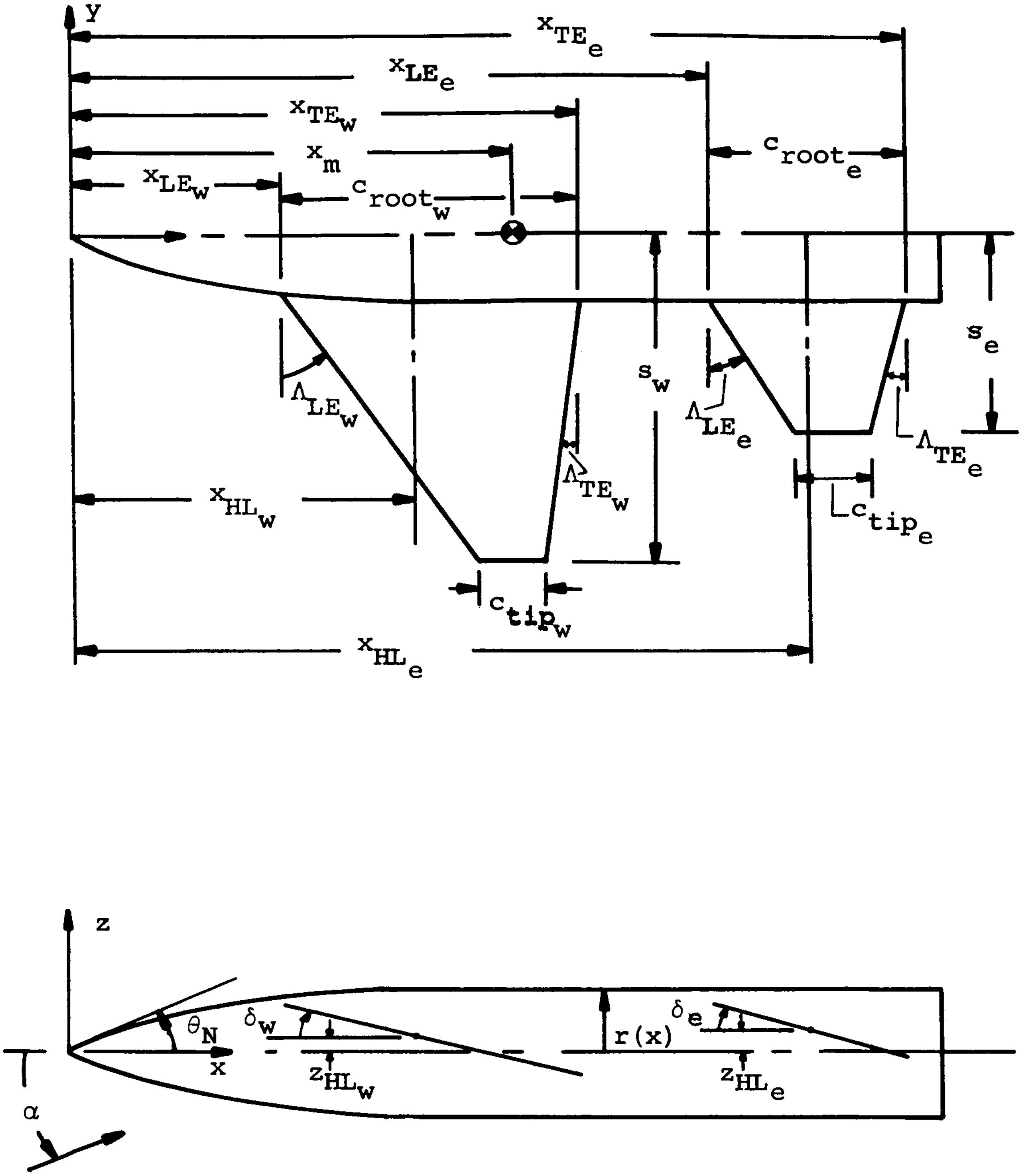

Figure 2.- Configuration geometry.

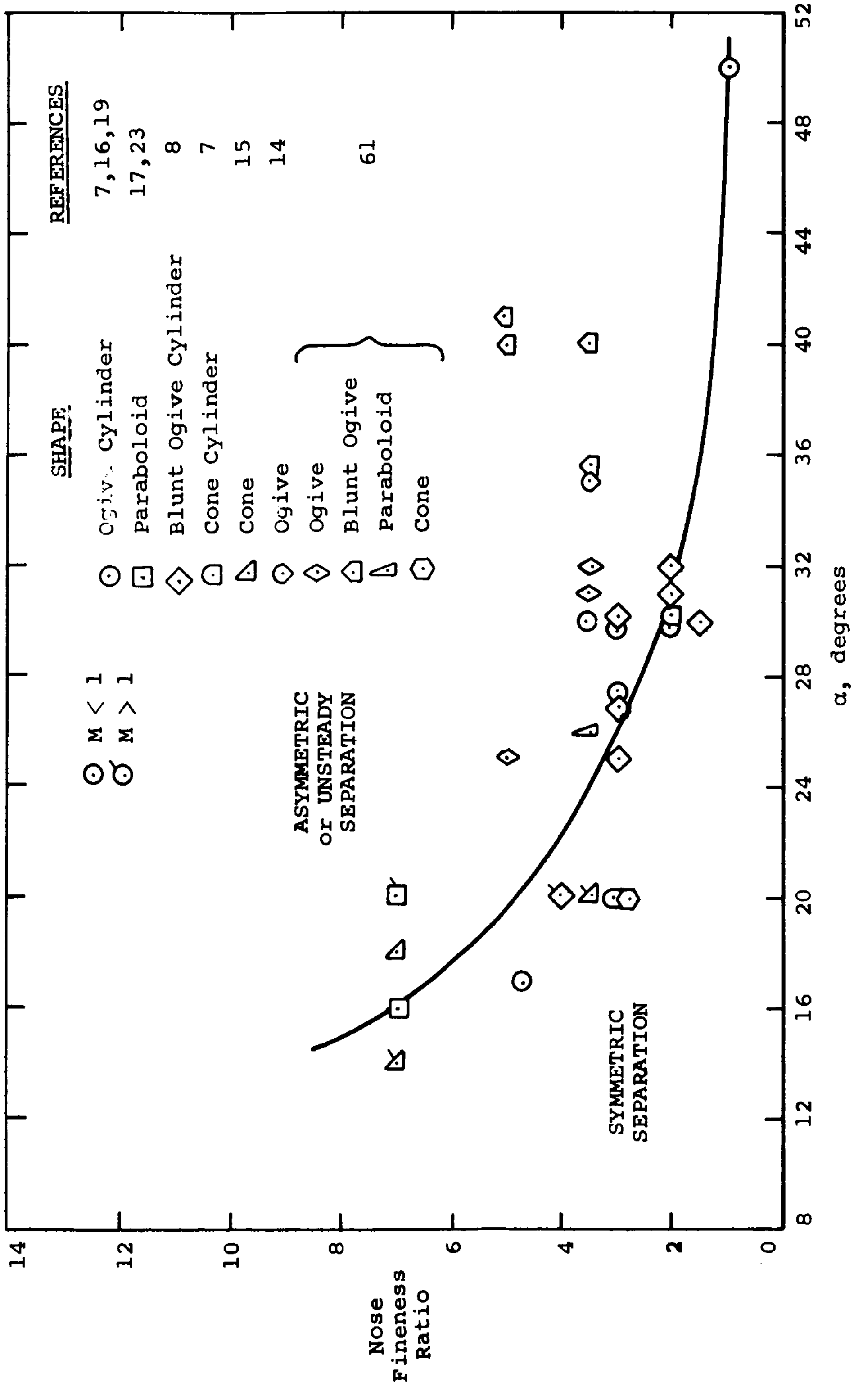

Figure 3.- Onset of asymmetric separation on bodies of revolution.

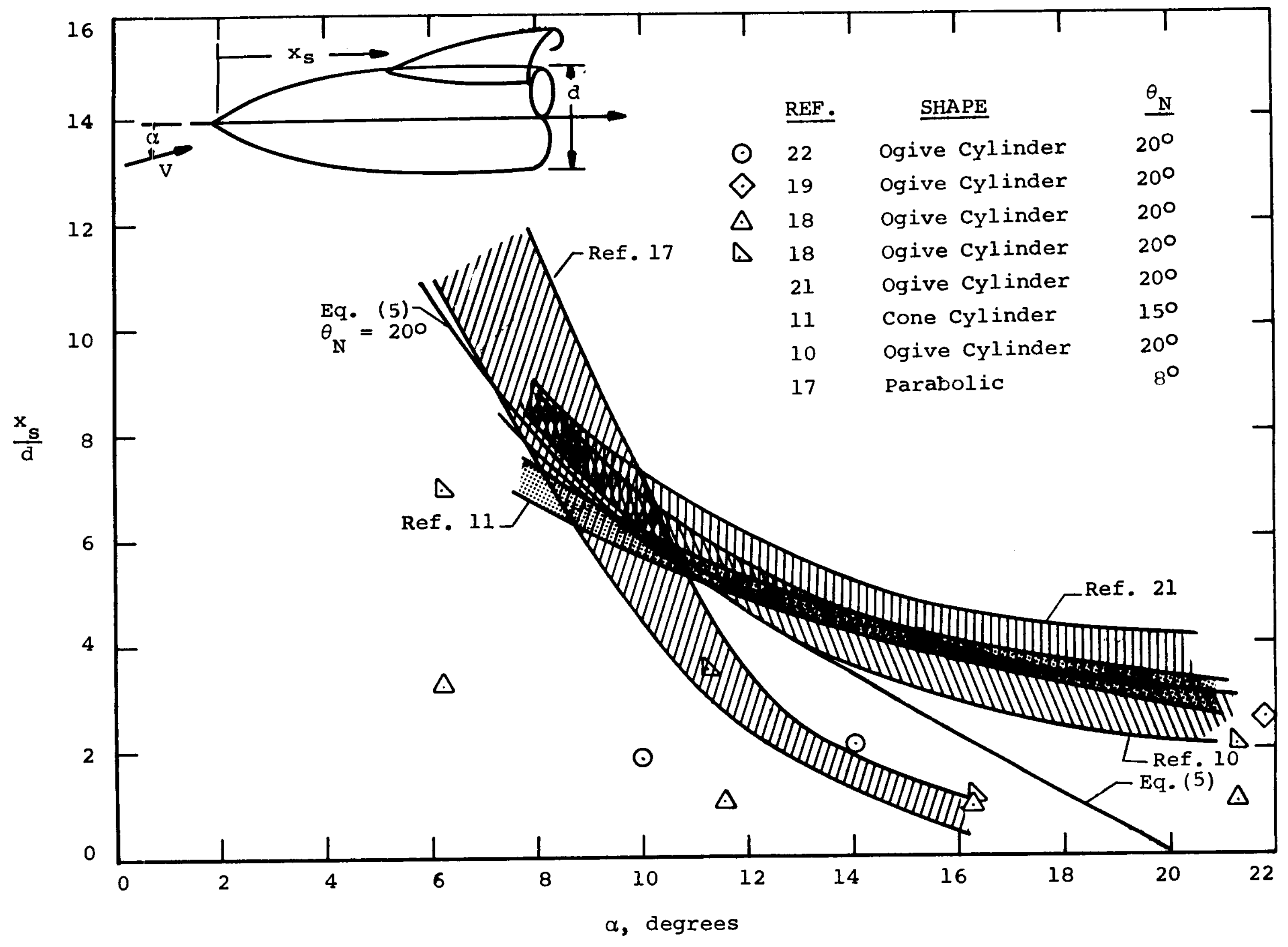

(a) Sharp-nosed bodies.

Figure 4.- Axial location of separation on bodies of revolution.

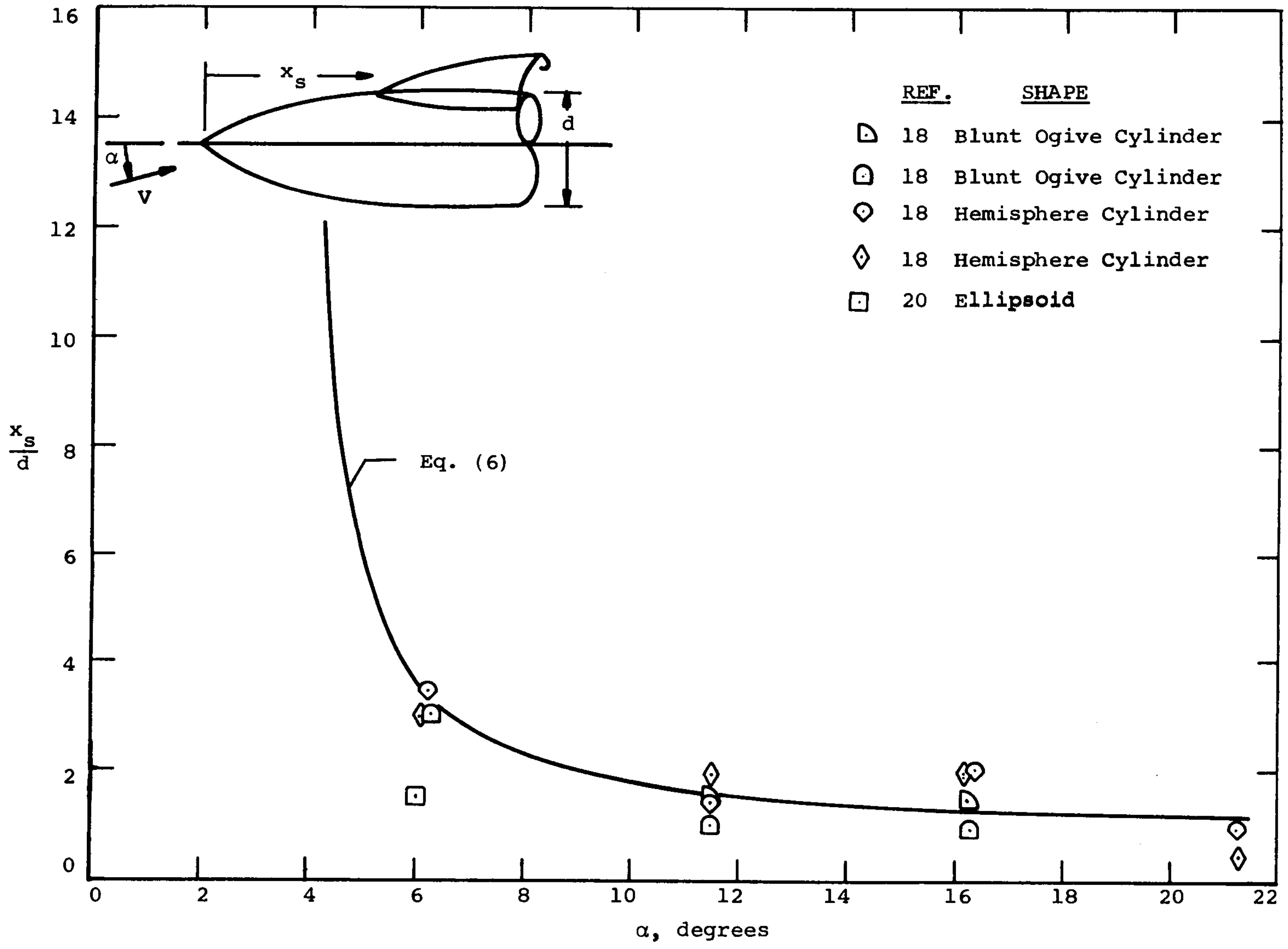

(b) Blunt-nosed bodies.

Figure 4.- Concluded.

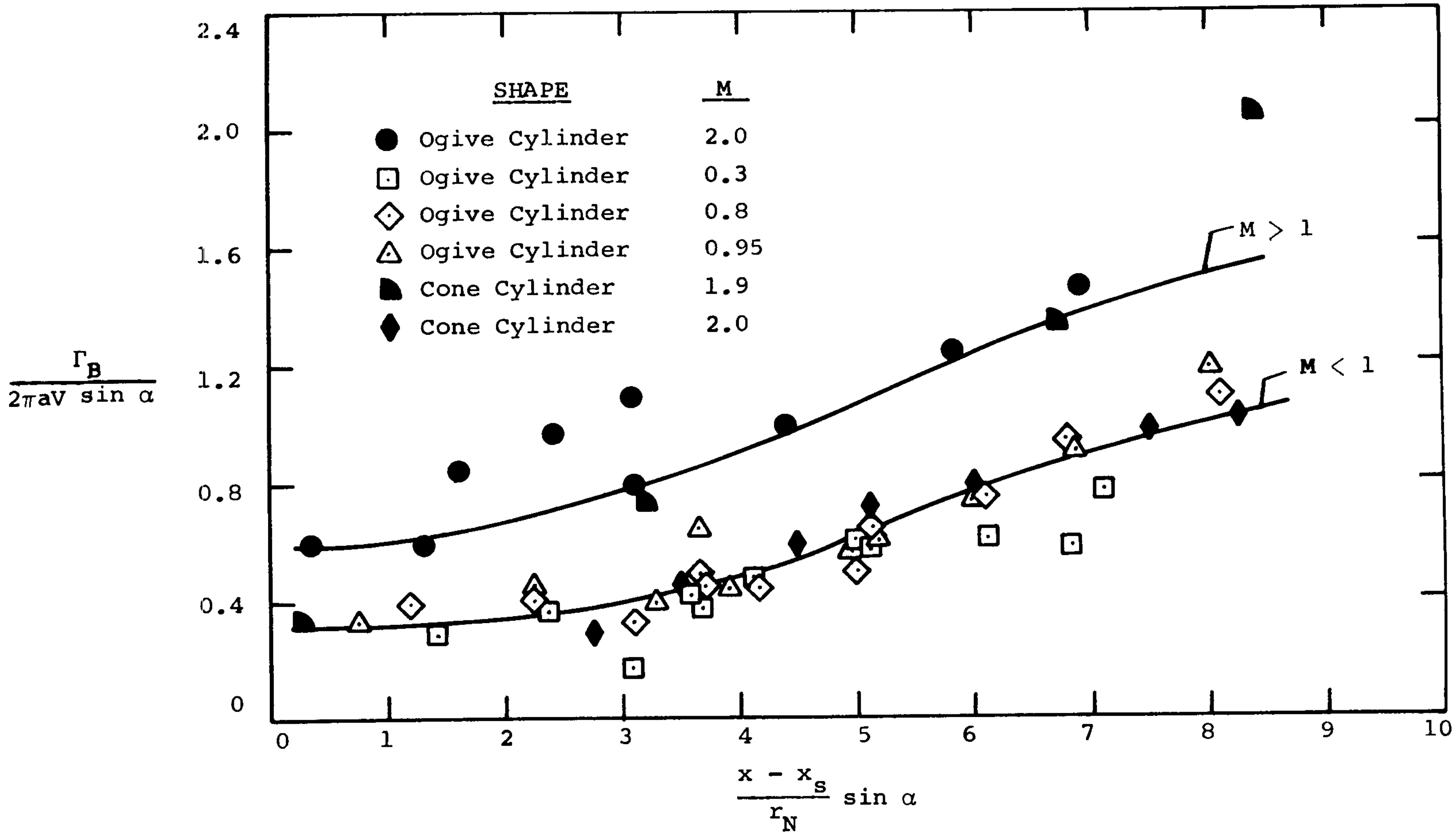

(a) Vortex strength.

Figure 5.- Body-vortex characteristics.

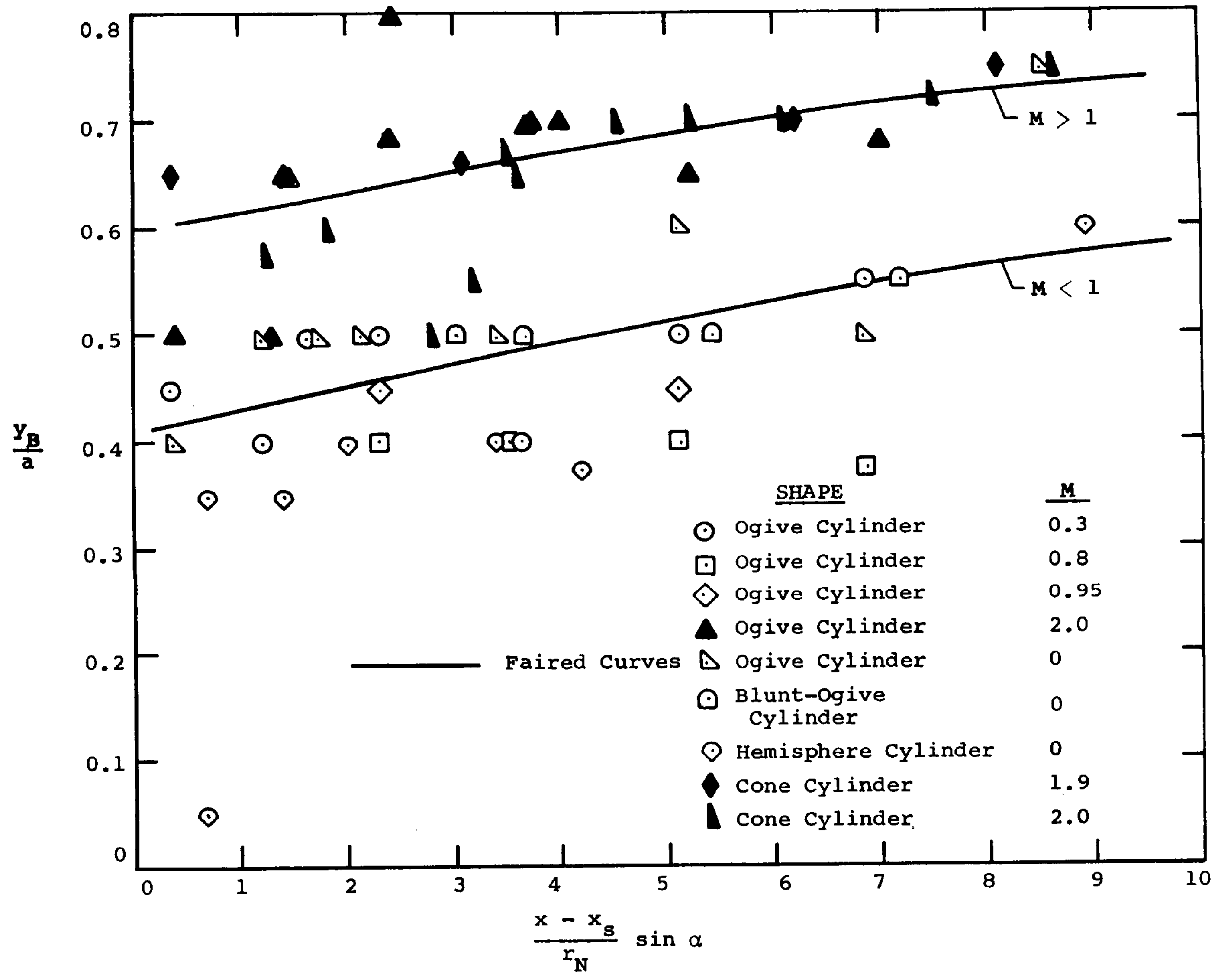

(b) Horizontal vortex position.

Figure 5.- Continued.

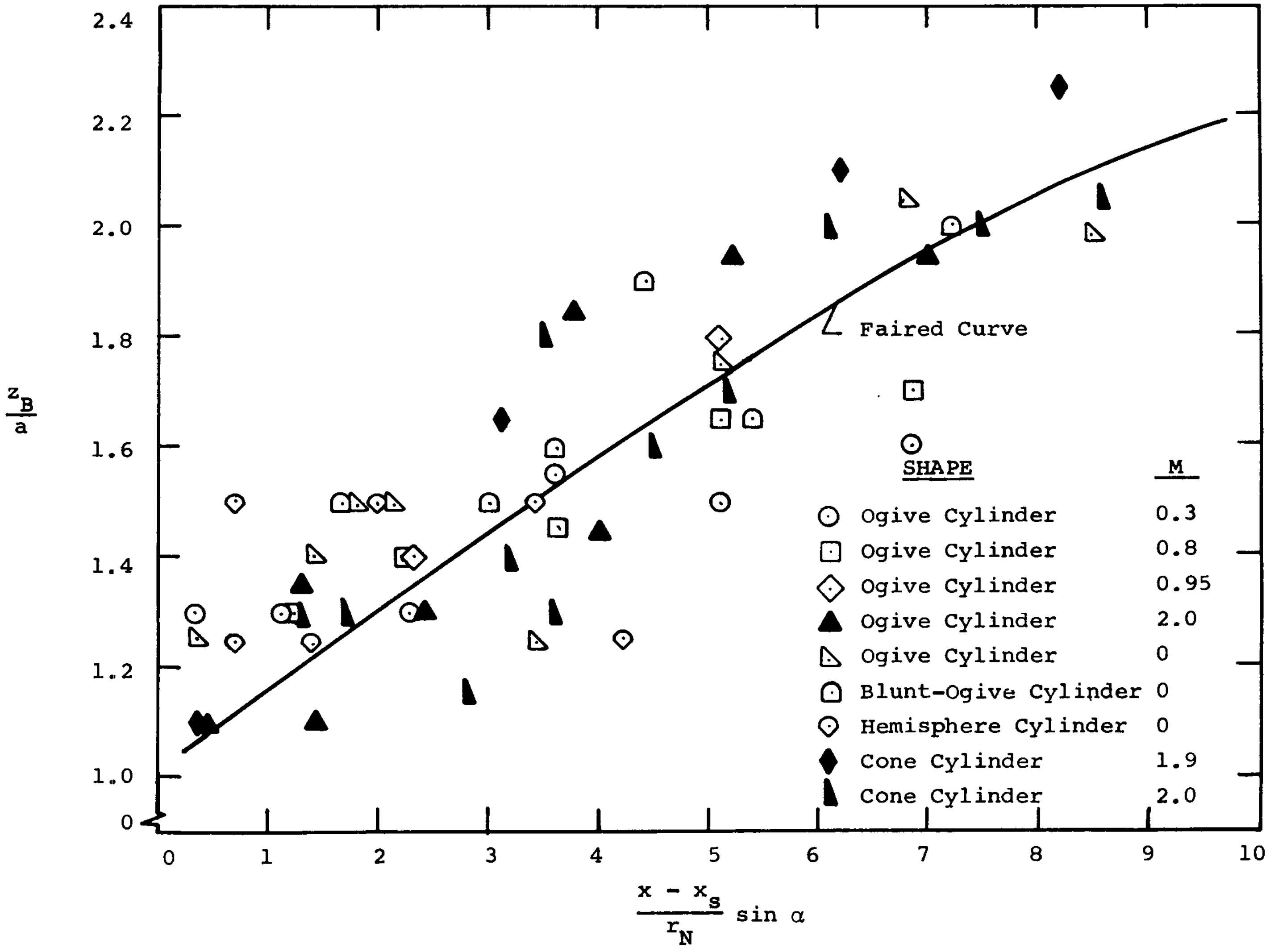

(c) Vertical vortex position.

Figure 5.- Concluded.

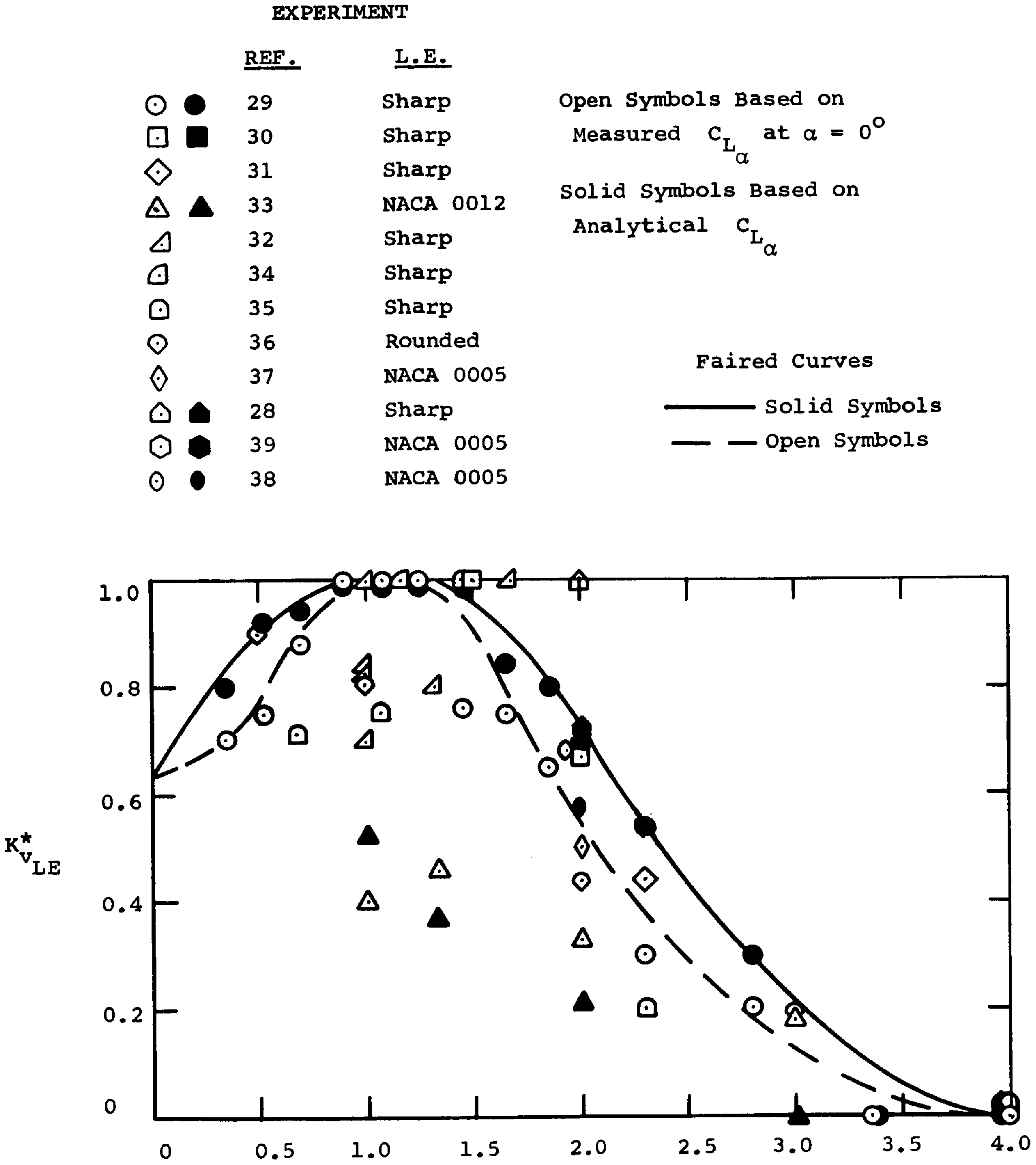

(a) Correlation curves.

Figure 6.- Vortex lift on delta wings in incompressible flow.

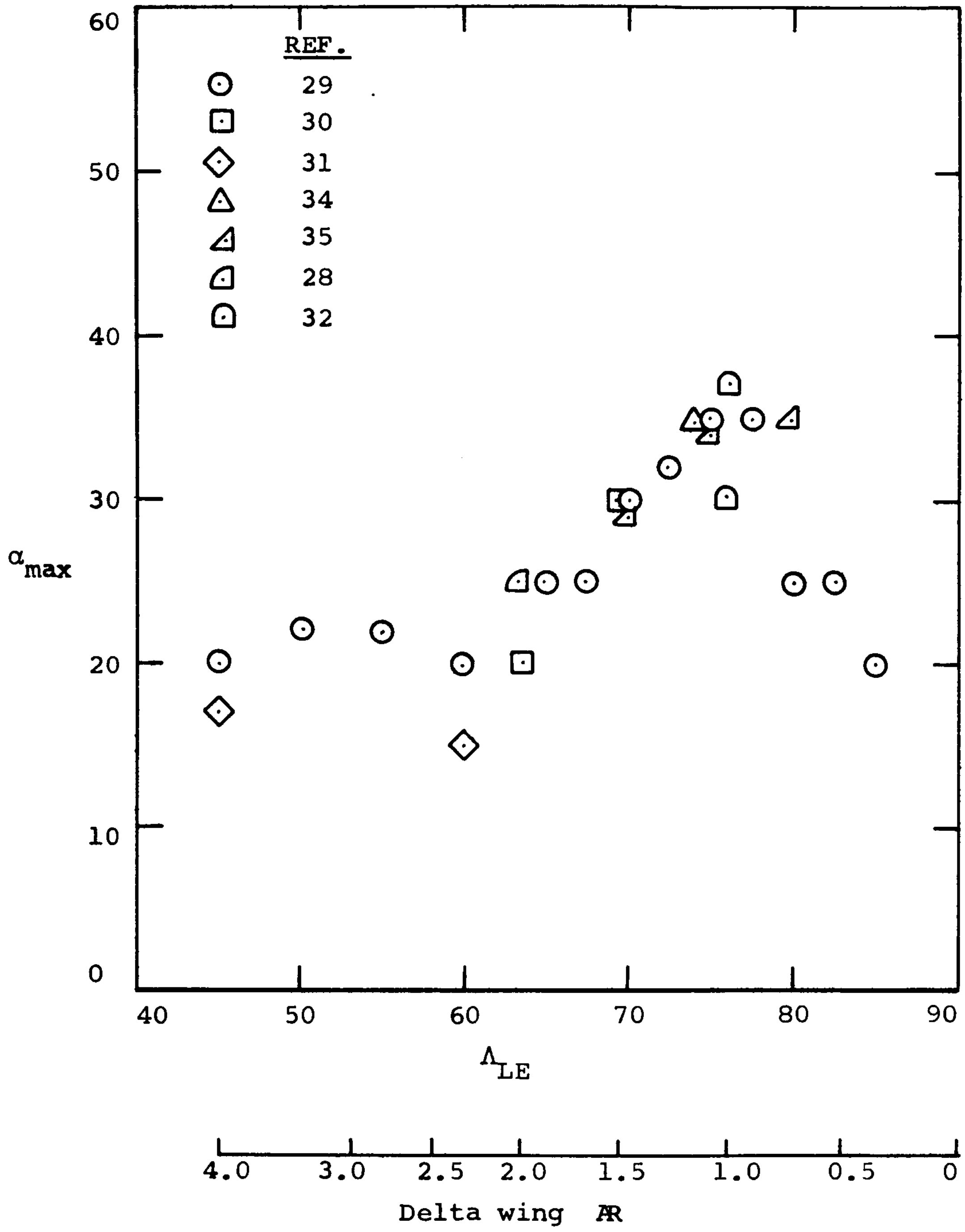

(b) Limits of validity of $K_{v_{LE}}$.

Figure 6.- Concluded.

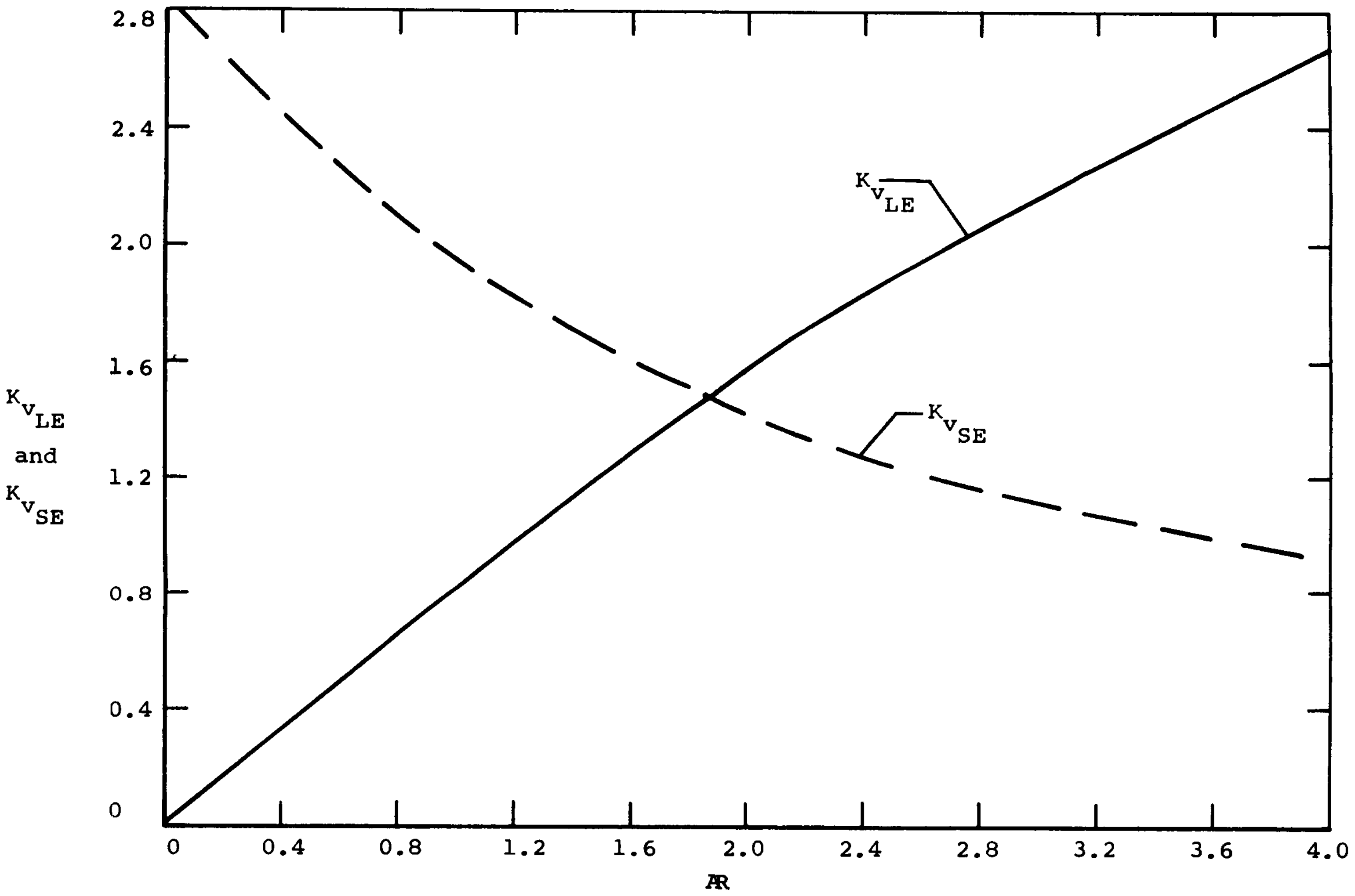

(a) Vortex-lattice predictions.

Figure 7.- Leading-edge and side-edge suction coefficients for rectangular wings in incompressible flow.

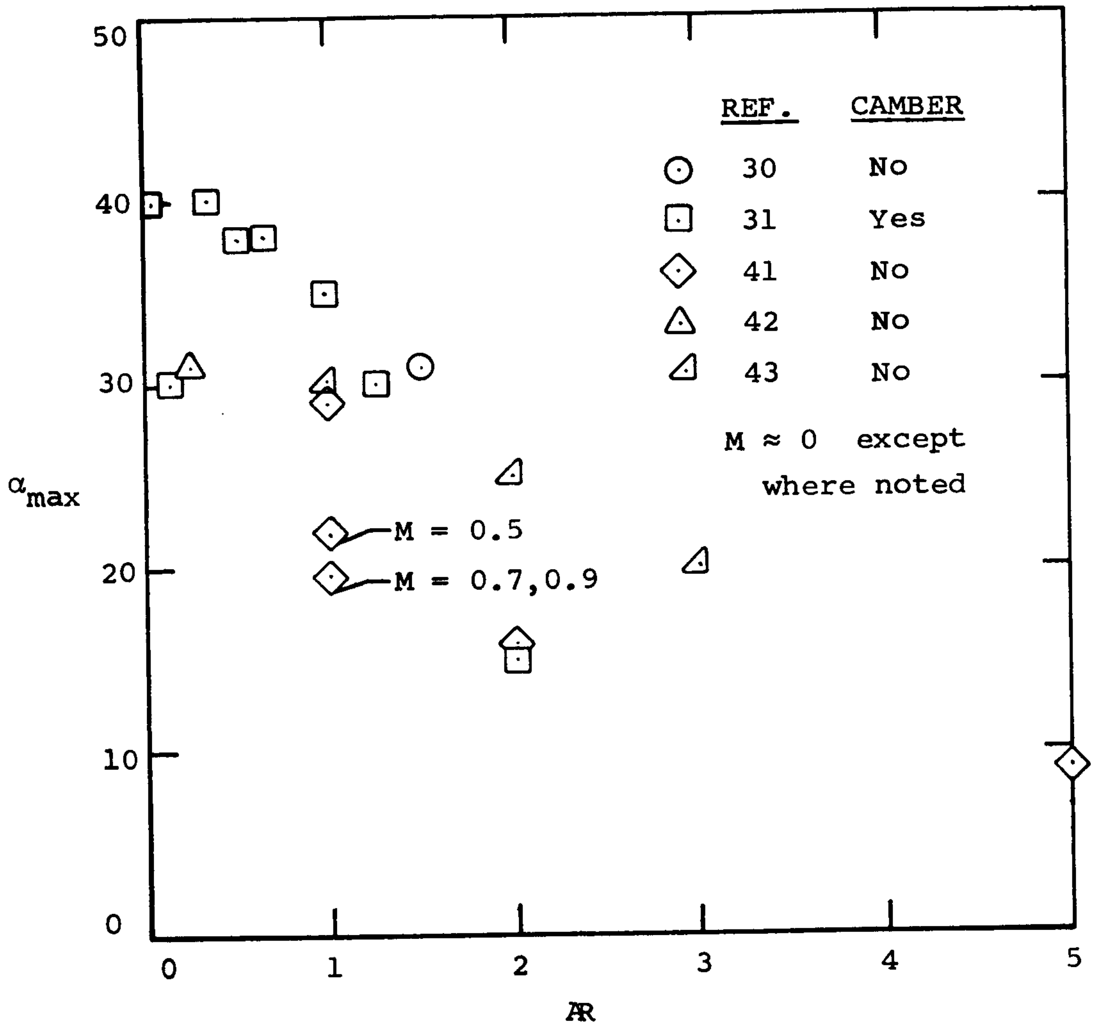

(b) Limits of validity of $K_{v_{LE}}$ and $K_{v_{SE}}$.

Figure 7.- Concluded.

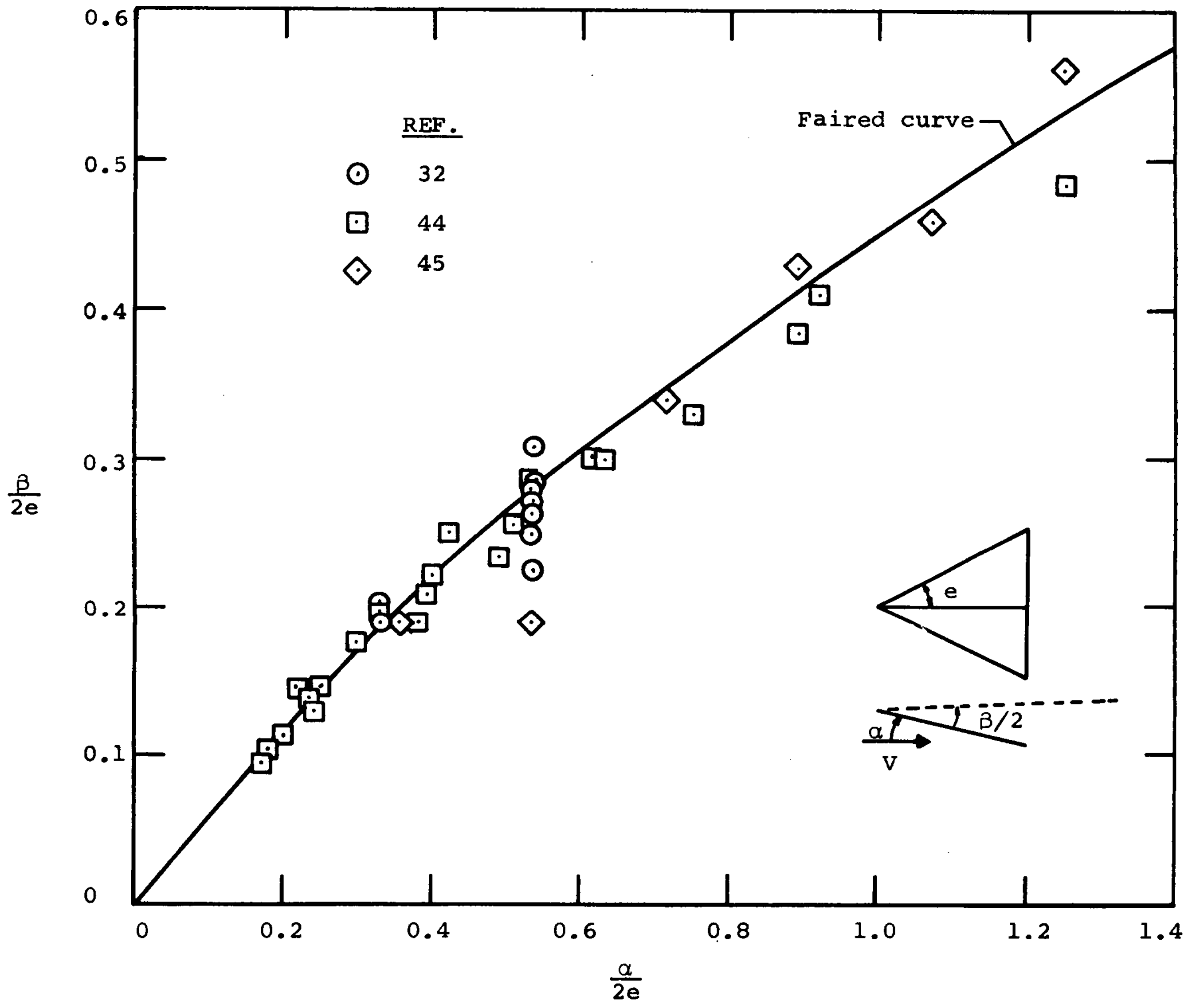

Figure 8.- Delta wing-separation vortex vertical position.

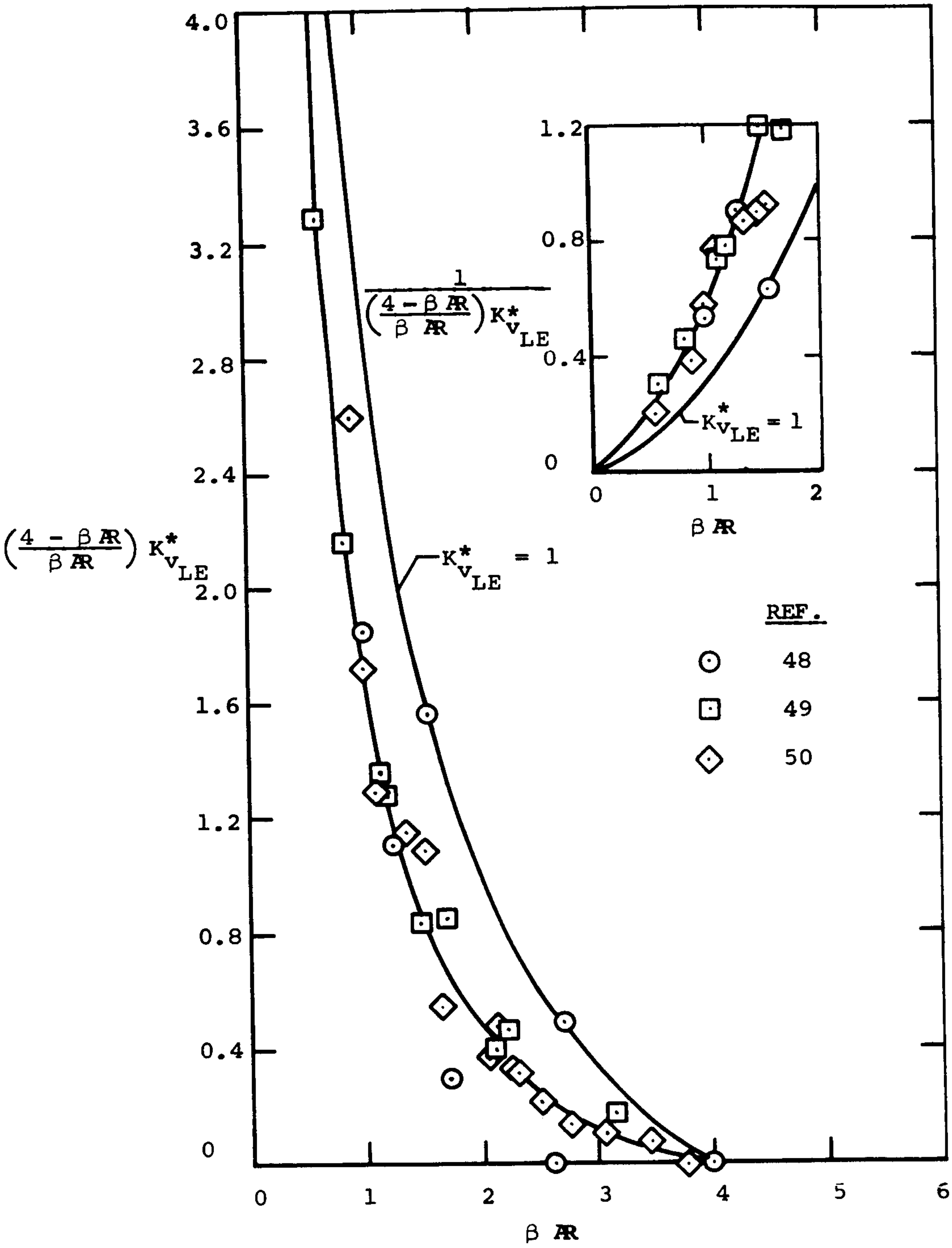

(a) Correlation curves.

Figure 9.- Vortex lift on delta wings in supersonic flow.

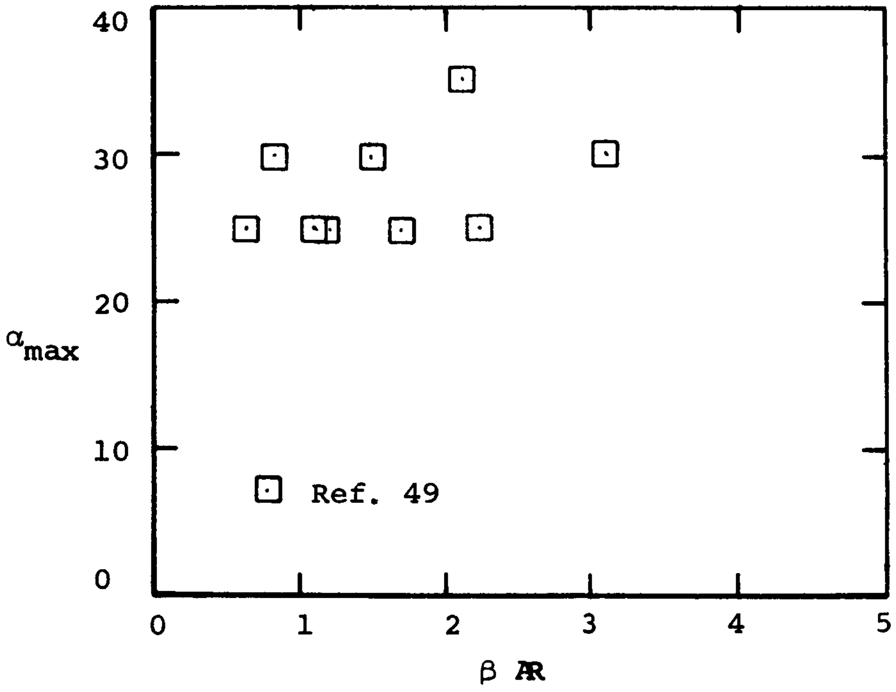

(b) Limits of validity of $K_{v_{LE}}$.

Figure 9.- Concluded.

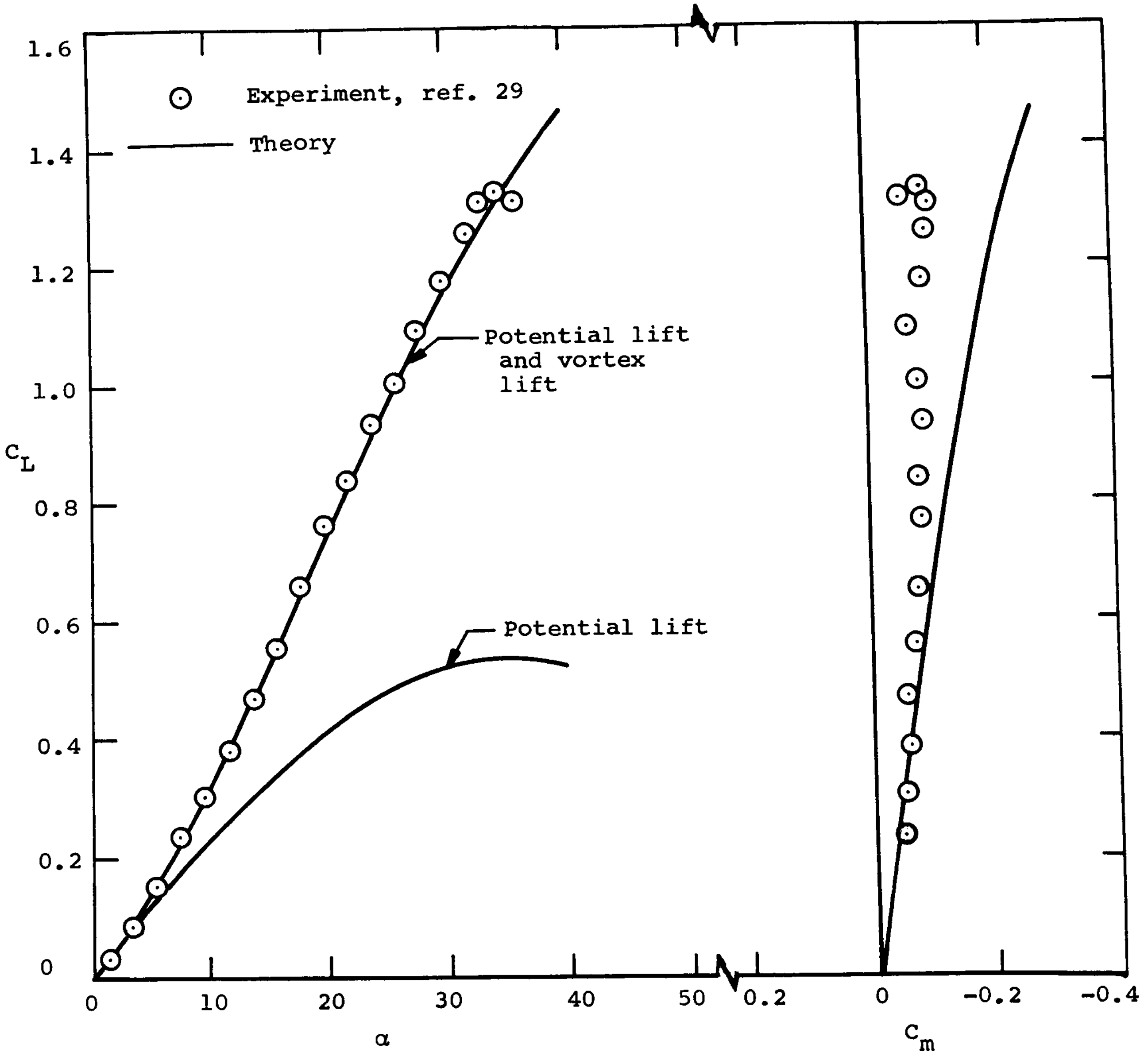

(a) $A\!\!\!R = 1.07$, $\Lambda_{LE} = 75^{\circ}$.

Figure 10.- Measured and predicted lift and pitching-moment characteristics of sharp-edged delta wings.

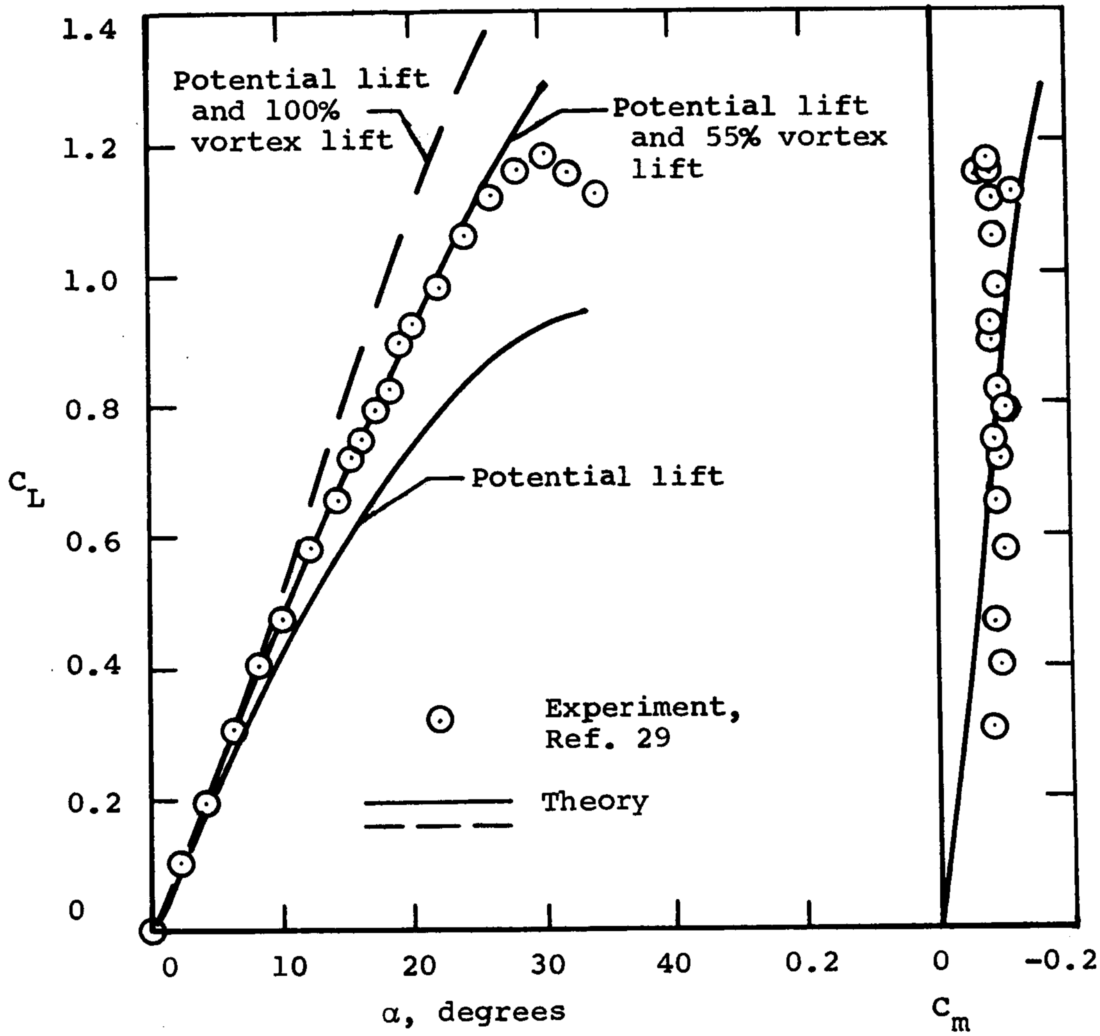

(b) $AR = 2.31$, $\Lambda_{LE} = 60^{\circ}$.

Figure 10.- Concluded.

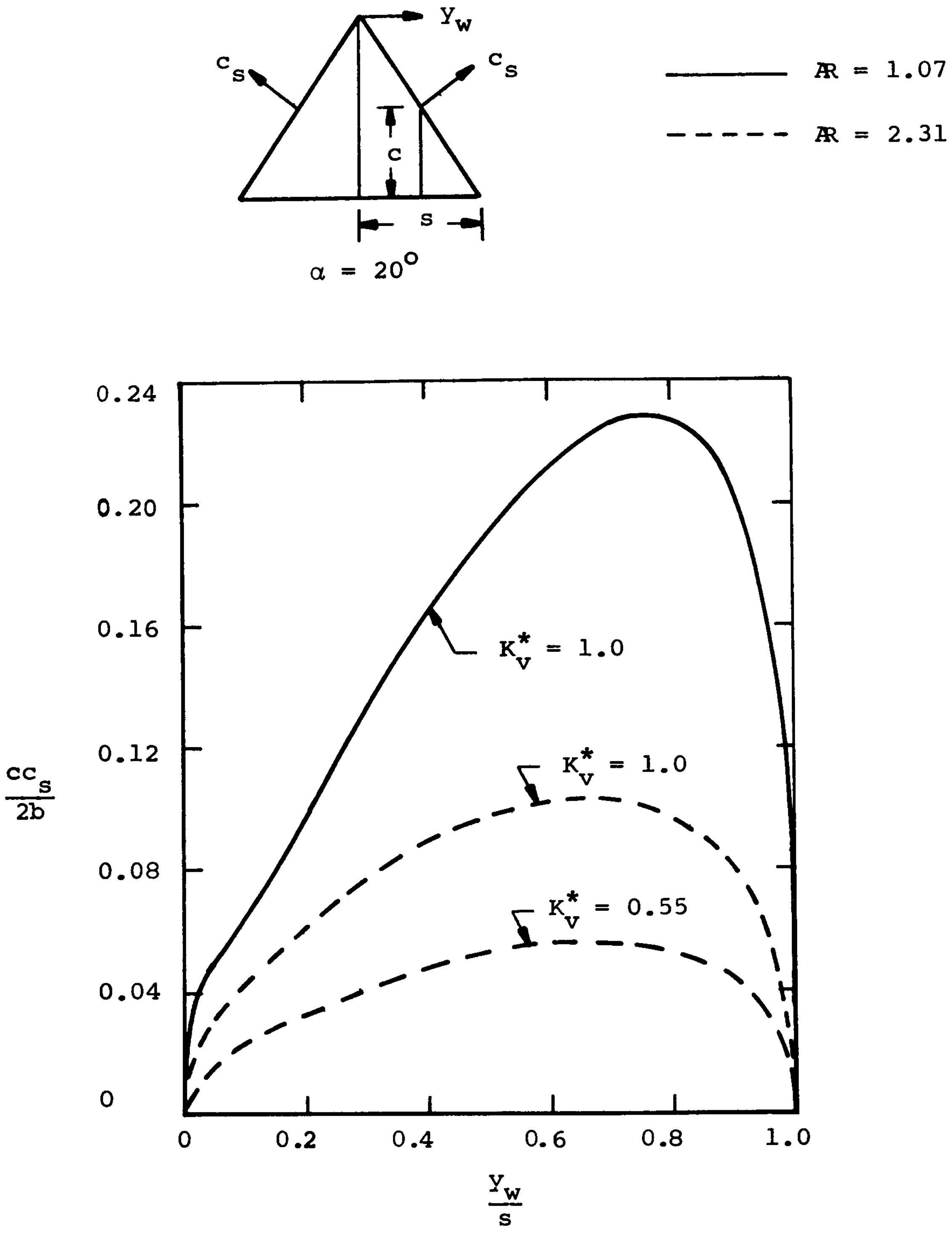

Figure 11.- Predicted leading-edge suction distribution on two delta wings at $\alpha = 20^\circ$.

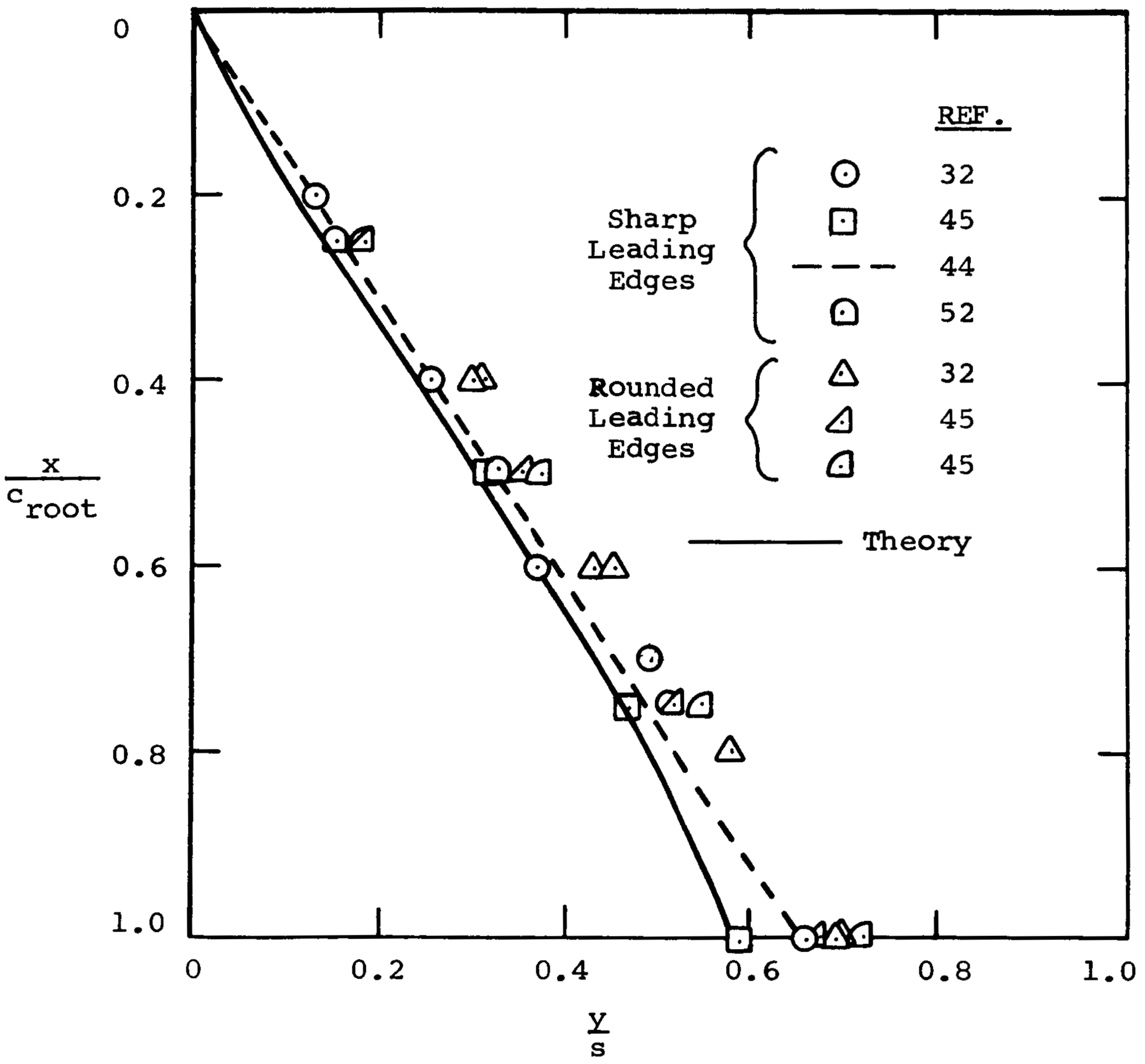

Figure 12.- Comparison of measured and predicted lateral vortex positions on delta wings with aspect ratio 1 at 15° angle of attack.

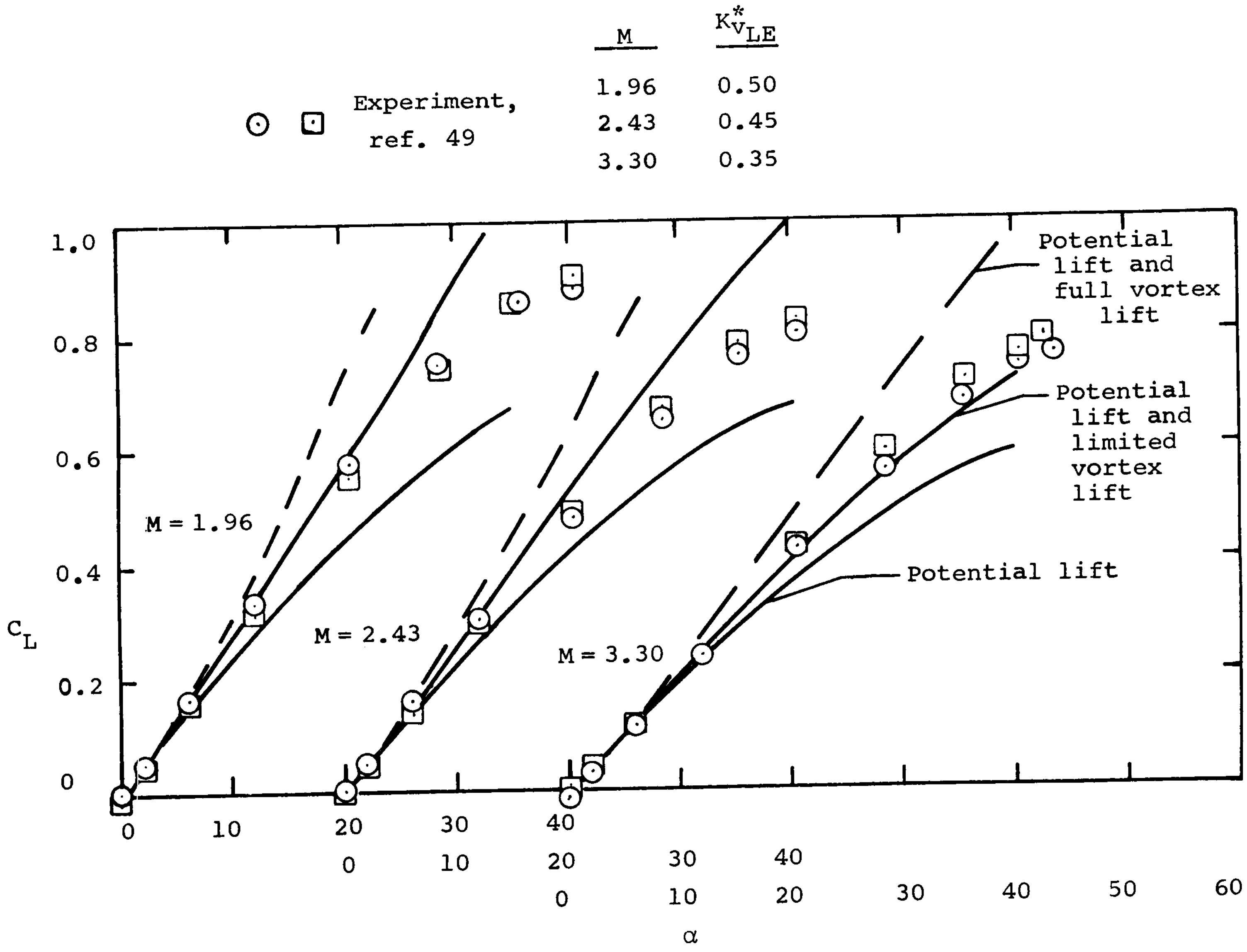

Figure 13.- Comparison of measured and predicted lift coefficients on a delta wing of aspect ratio 1 in supersonic flow.

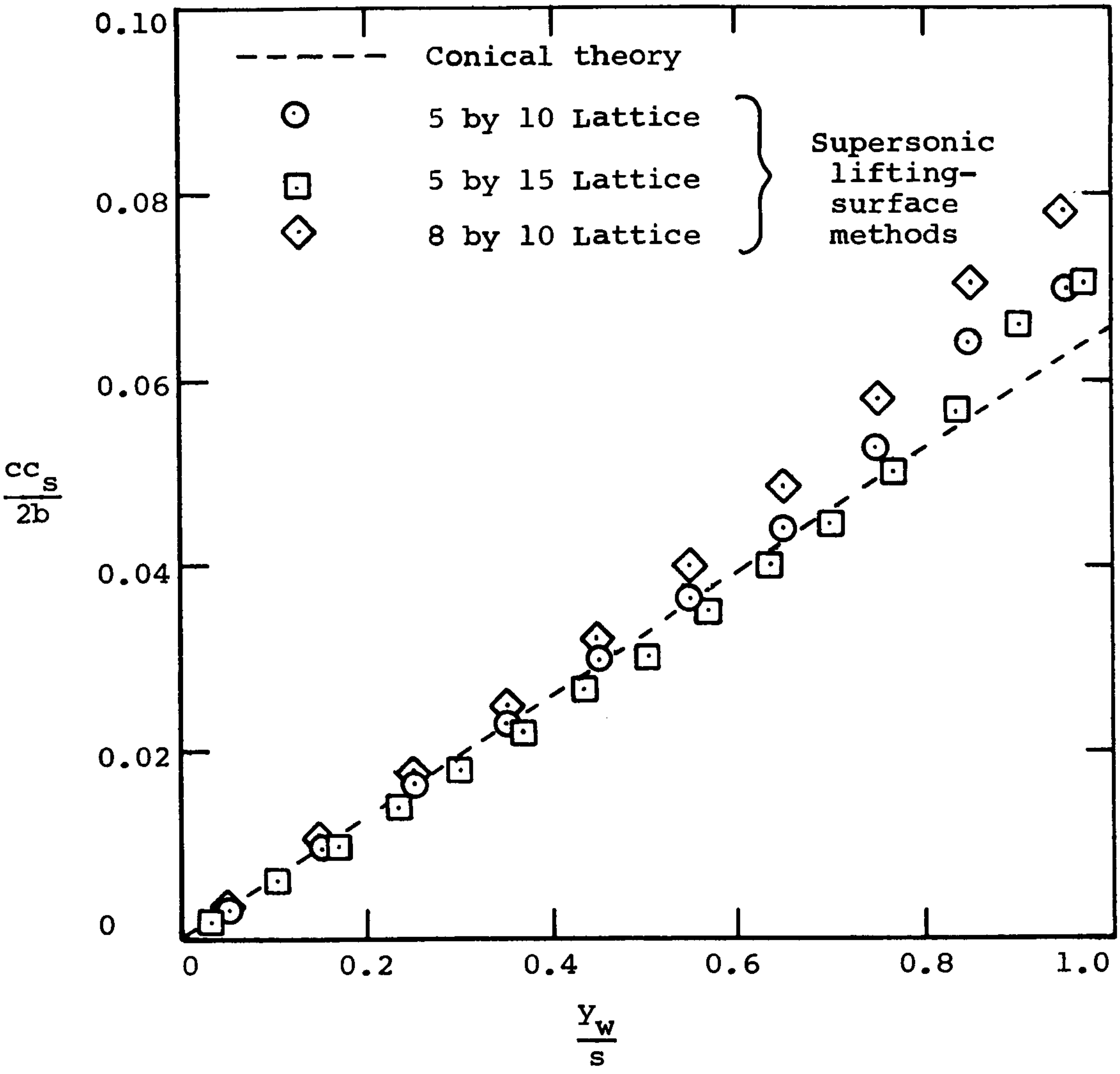

Figure 14.- Predicted spanwise suction distribution on an aspect ratio 1 delta wing at at M = 1.96 and 10° angle of attack.

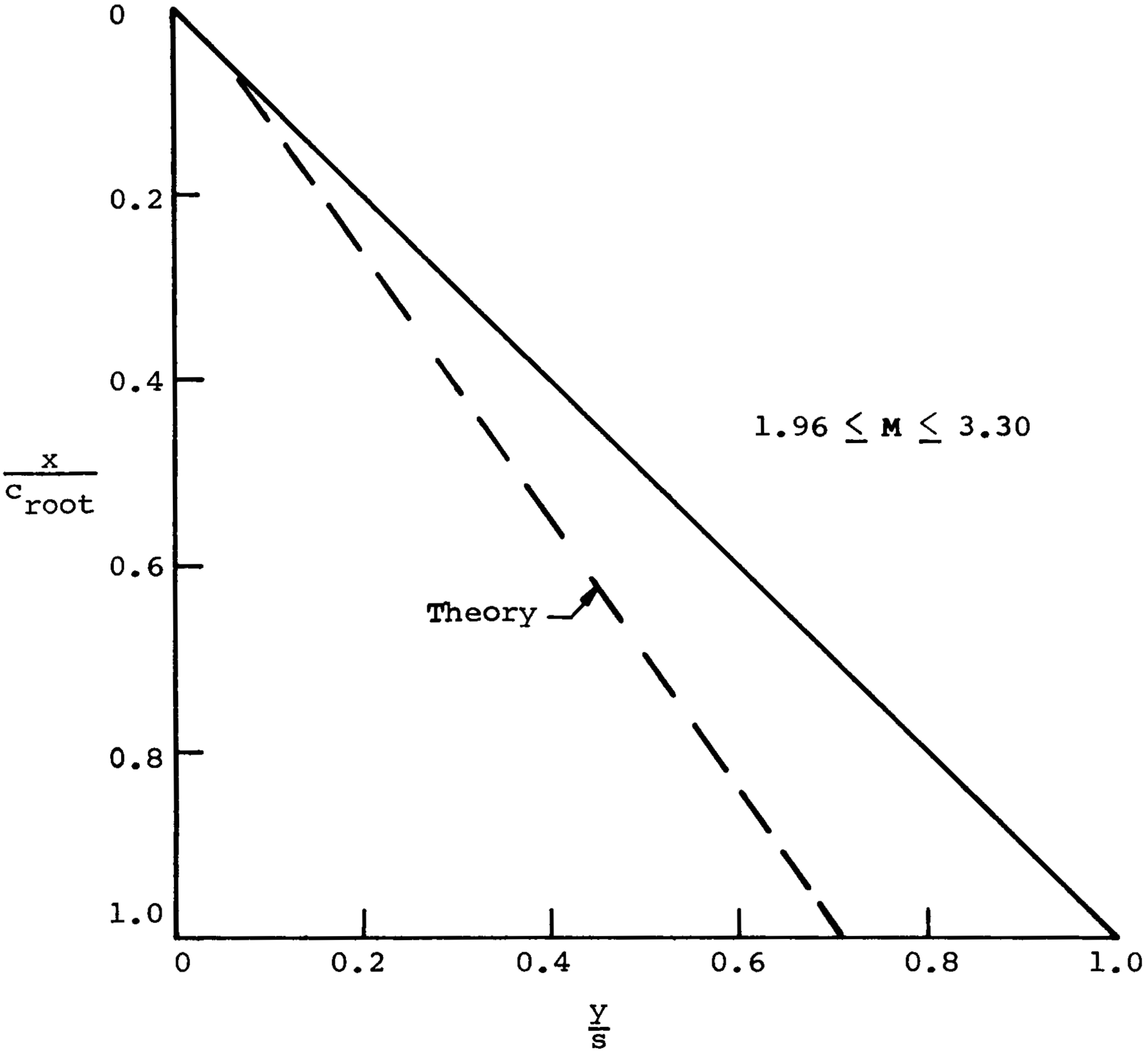

Figure 15.- Predicted lateral vortex position on an aspect ratio 1 delta wing in supersonic flow.

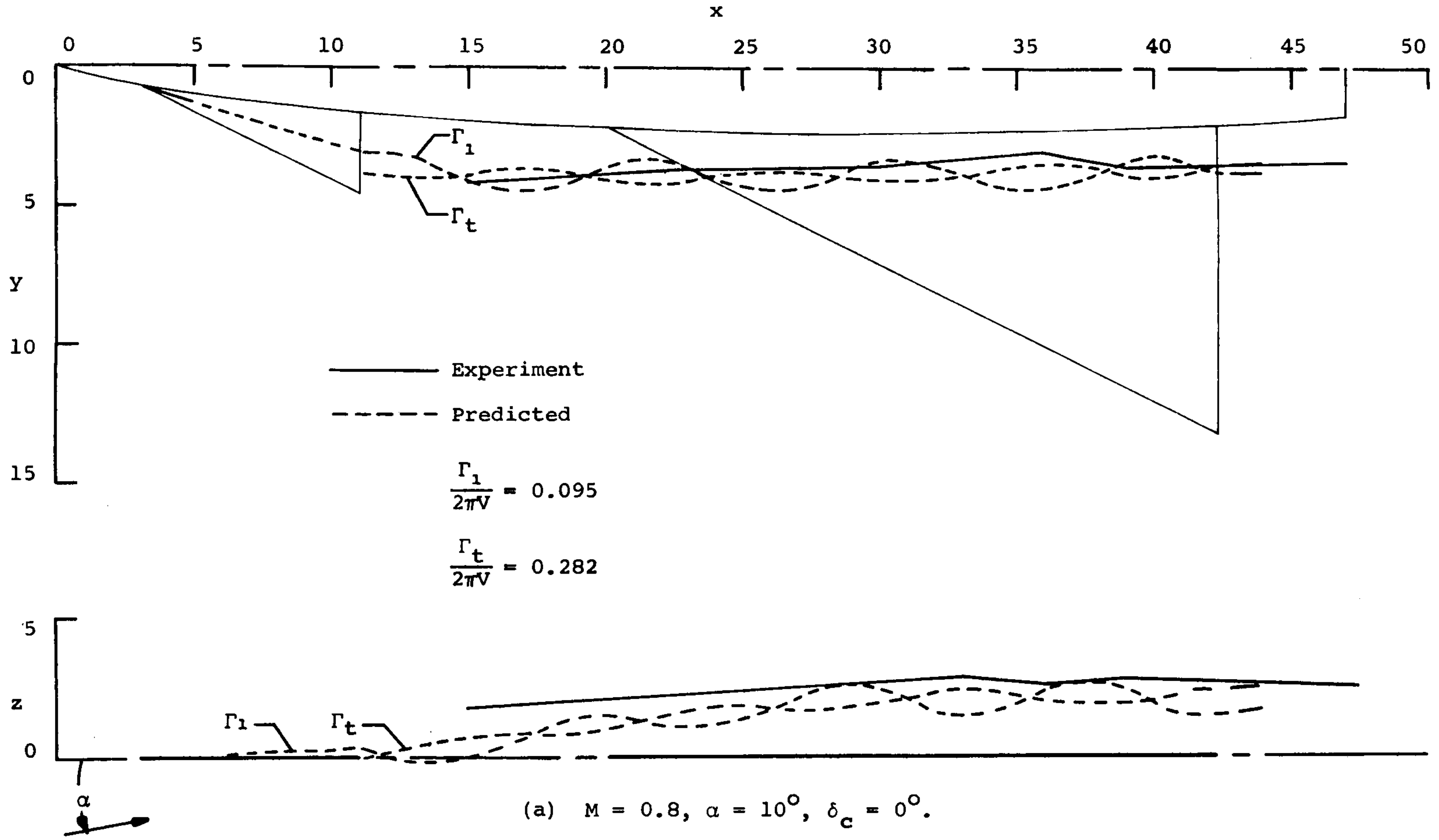

(a) $M = 0.8$, $\alpha = 10^\circ$, $\delta_c = 0^\circ$.

Figure 16.- Comparison of predicted and observed vortex trajectories on a canard-body-wing configuration.

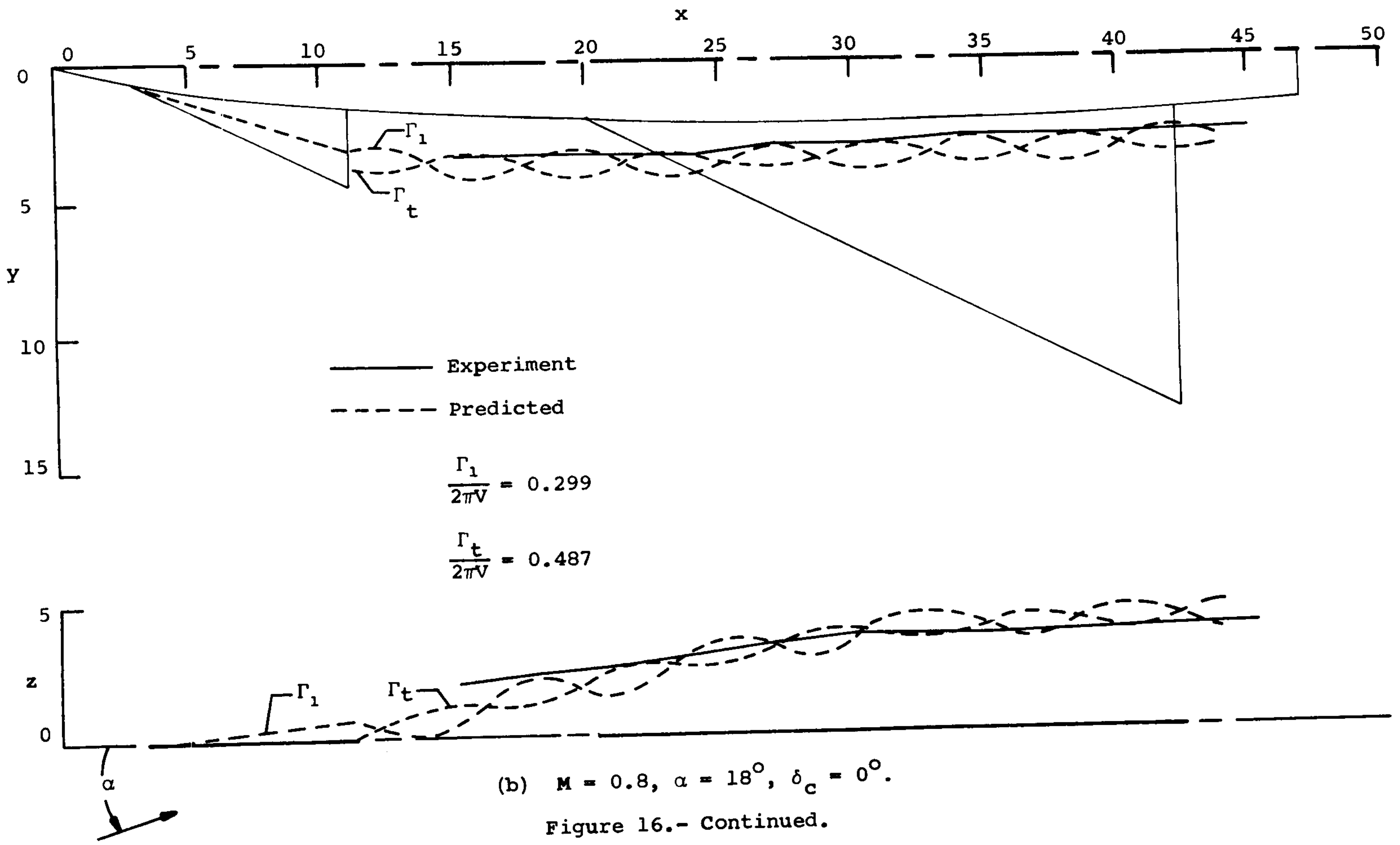

(b) $M = 0.8$, $\alpha = 18^\circ$, $\delta_c = 0^\circ$.

Figure 16.- Continued.

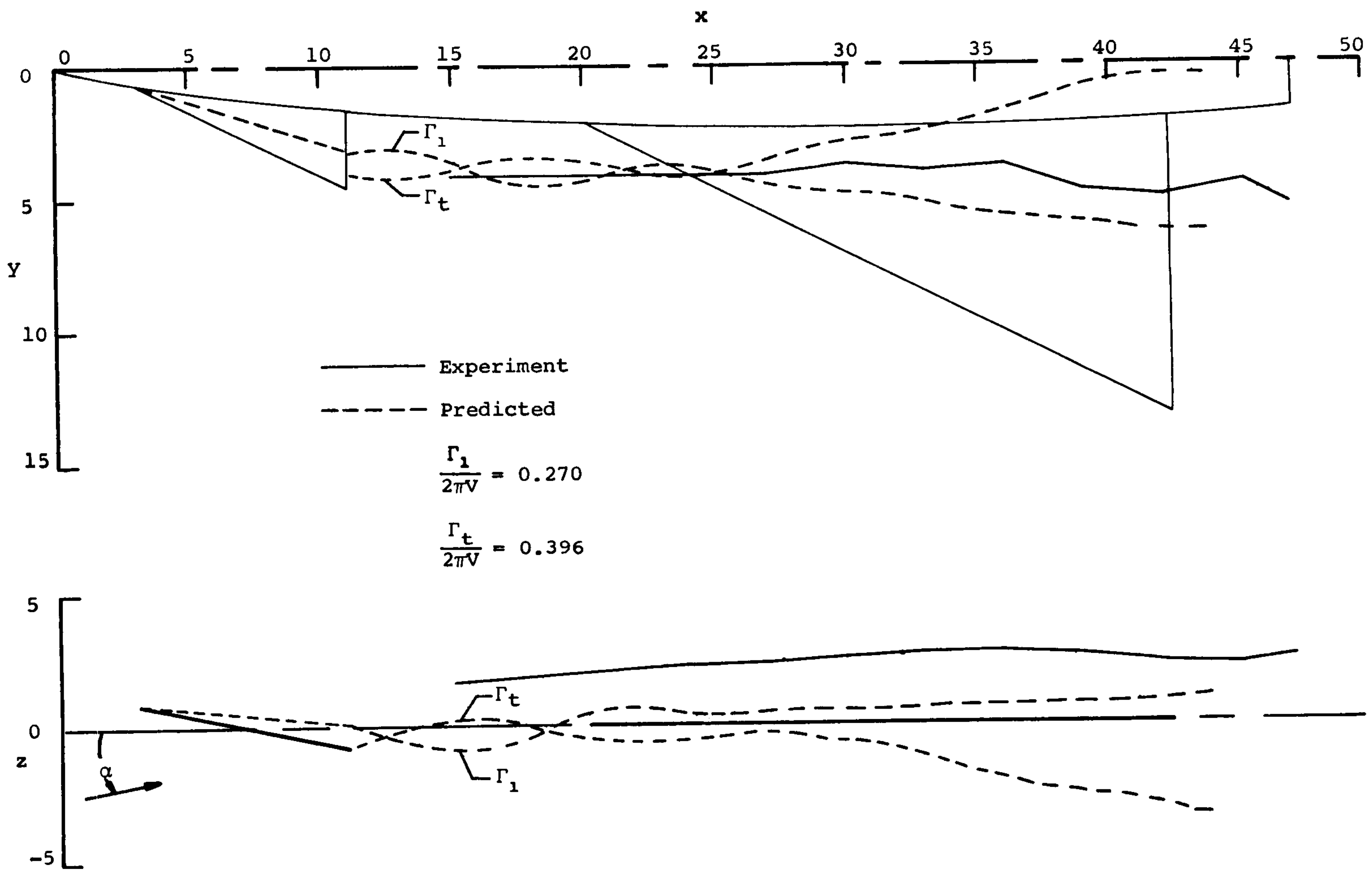

(c) $M = 0.8$, $\alpha = 10^\circ$, $\delta_c = 10^\circ$.

Figure 16.- Continued.

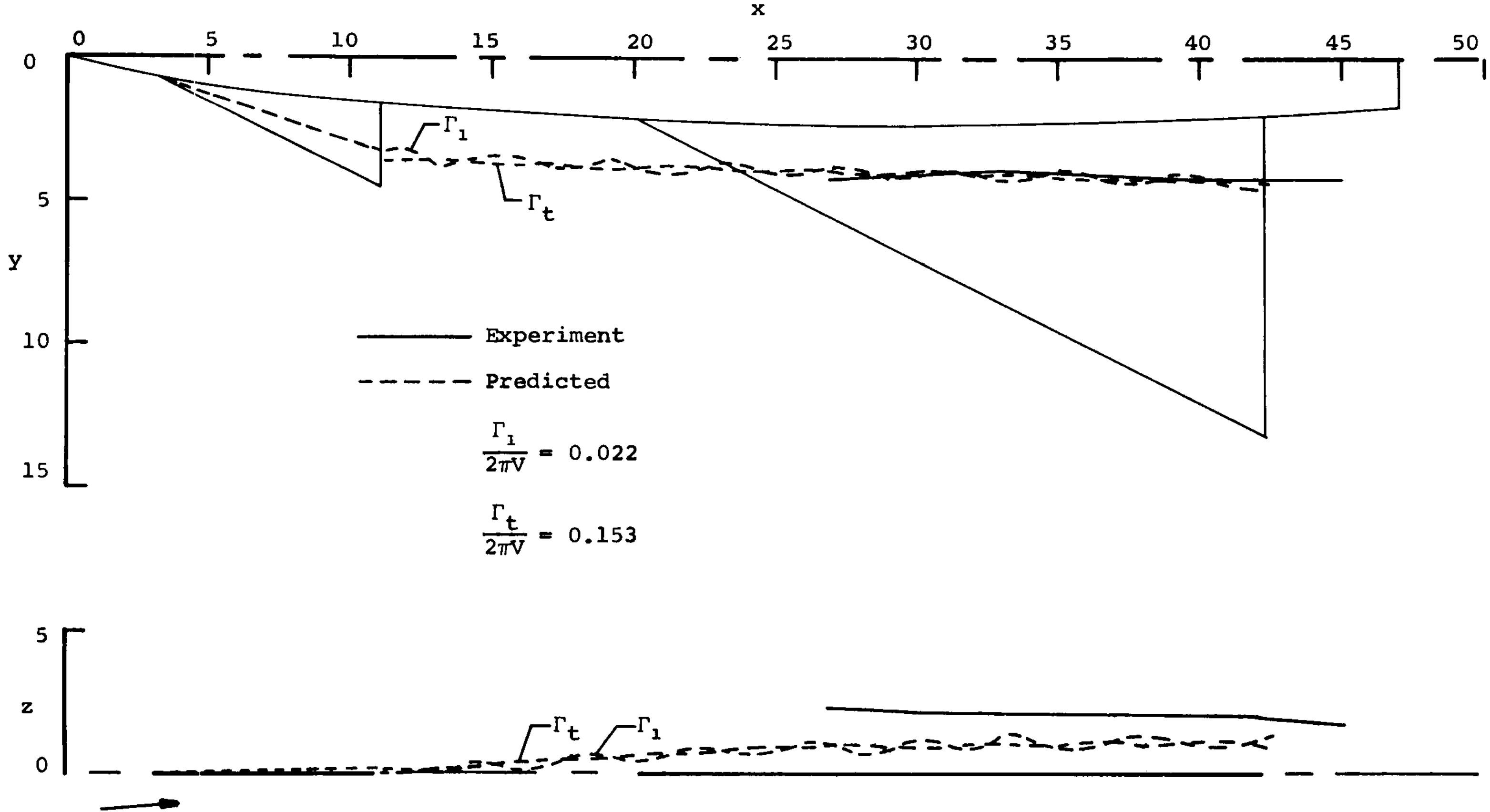

(d) M = 1.3, $\alpha = 5^\circ$, $\delta_c = 0^\circ$.

Figure 16.- Continued.

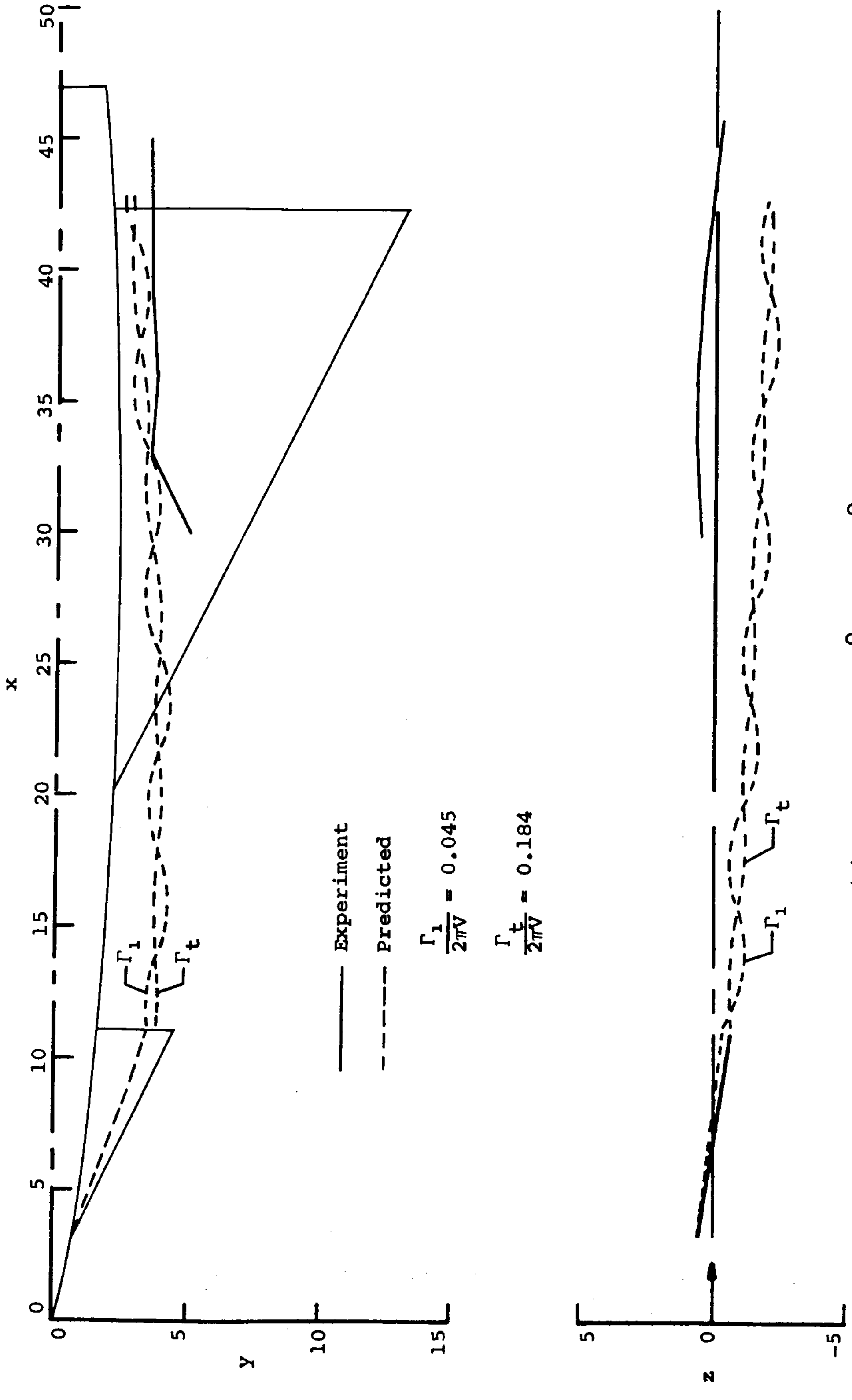

(e) M = 1.3, $\alpha = 0^\circ$, $\delta_c = 10^\circ$.

Figure 16.- Concluded.

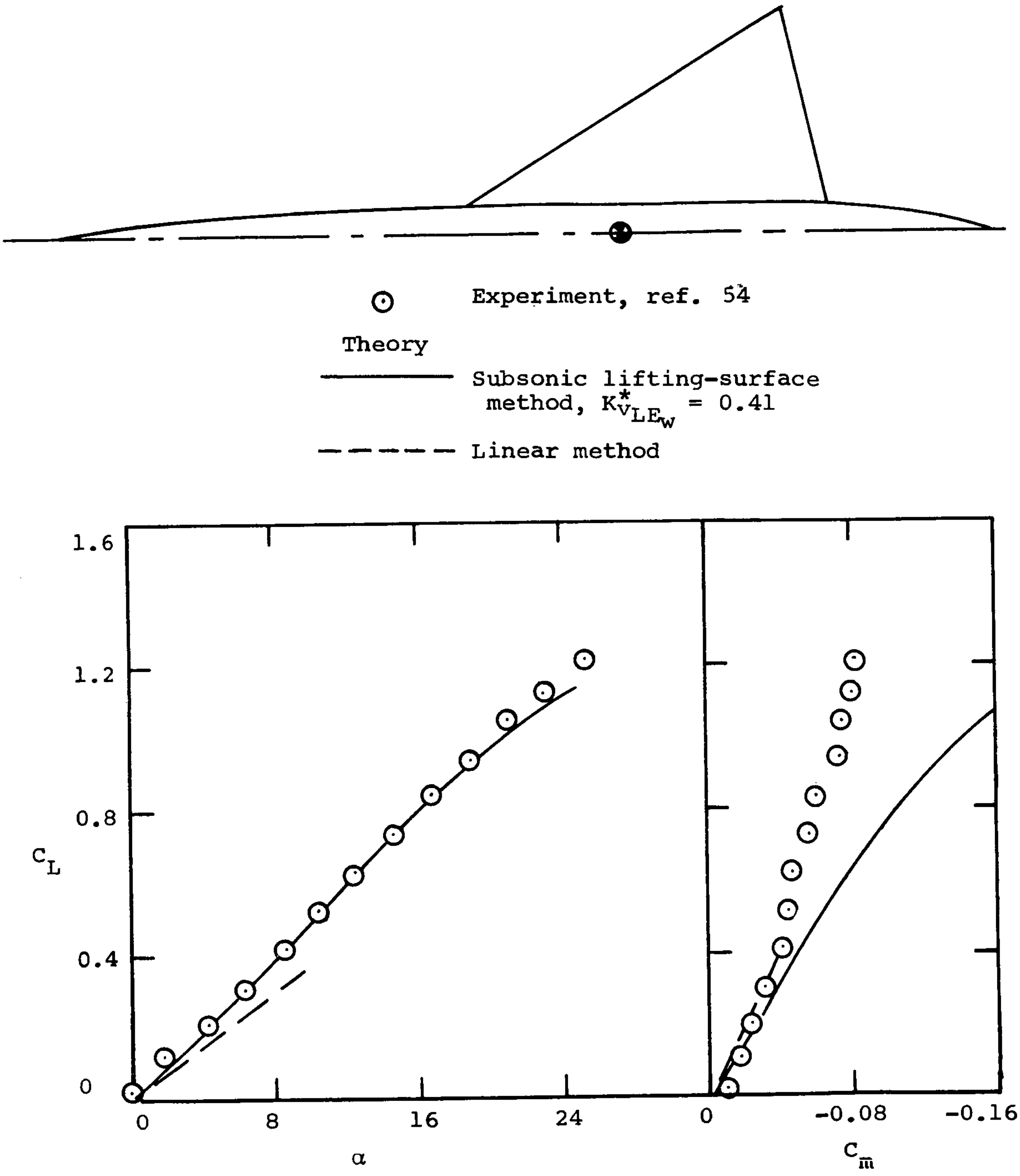

(a) Canard off.

Figure 17.- Comparison of measured and predicted lift and pitching-moment coefficients on a canard-body-wing configuration in subsonic flow.

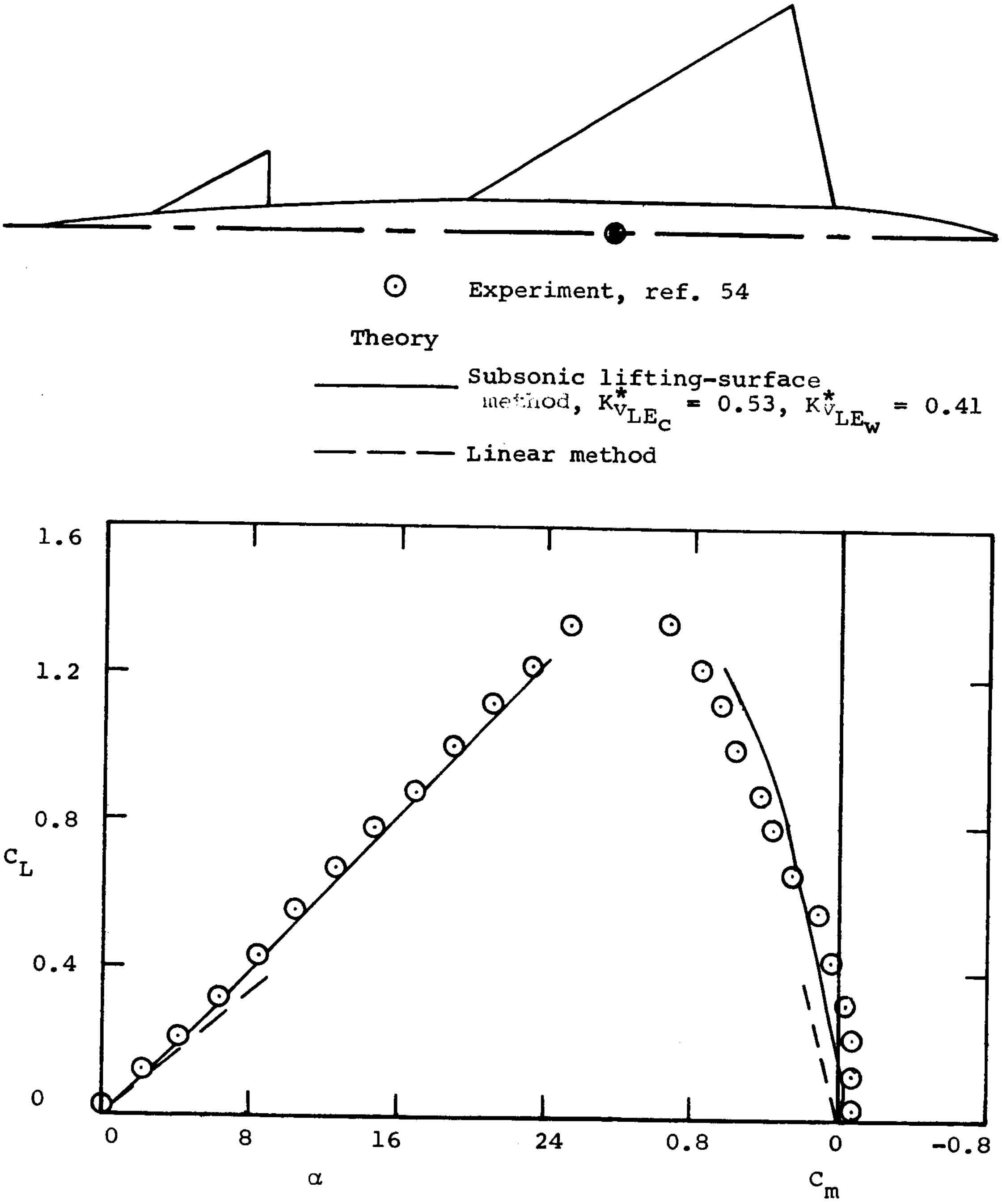

(b) Canard on, $\delta_c = 0^{\circ}$.

Figure 17.- Continued.

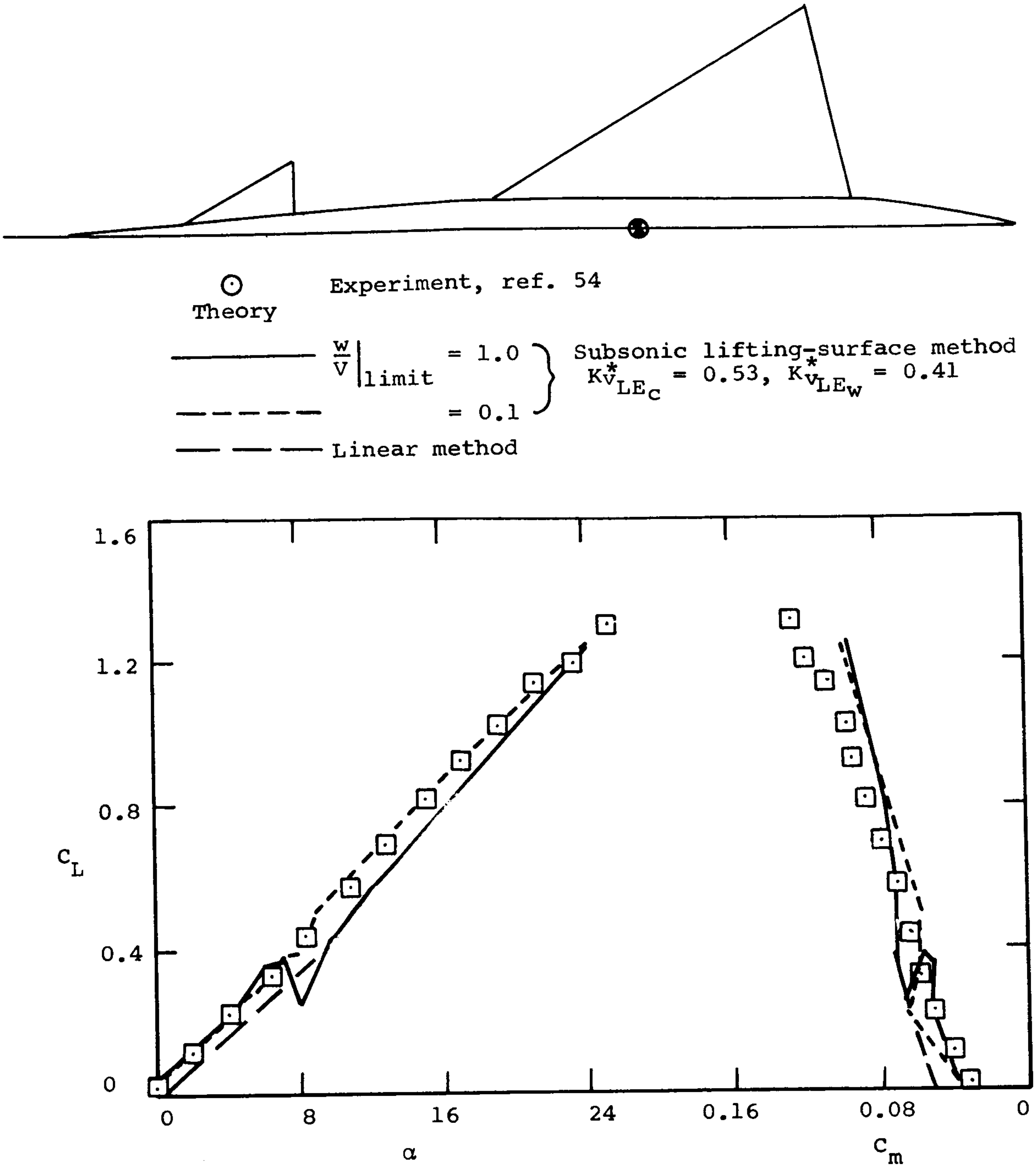

(c) Canard on, $\delta_c = 10^{\circ}$.

Figure 17.- Concluded.

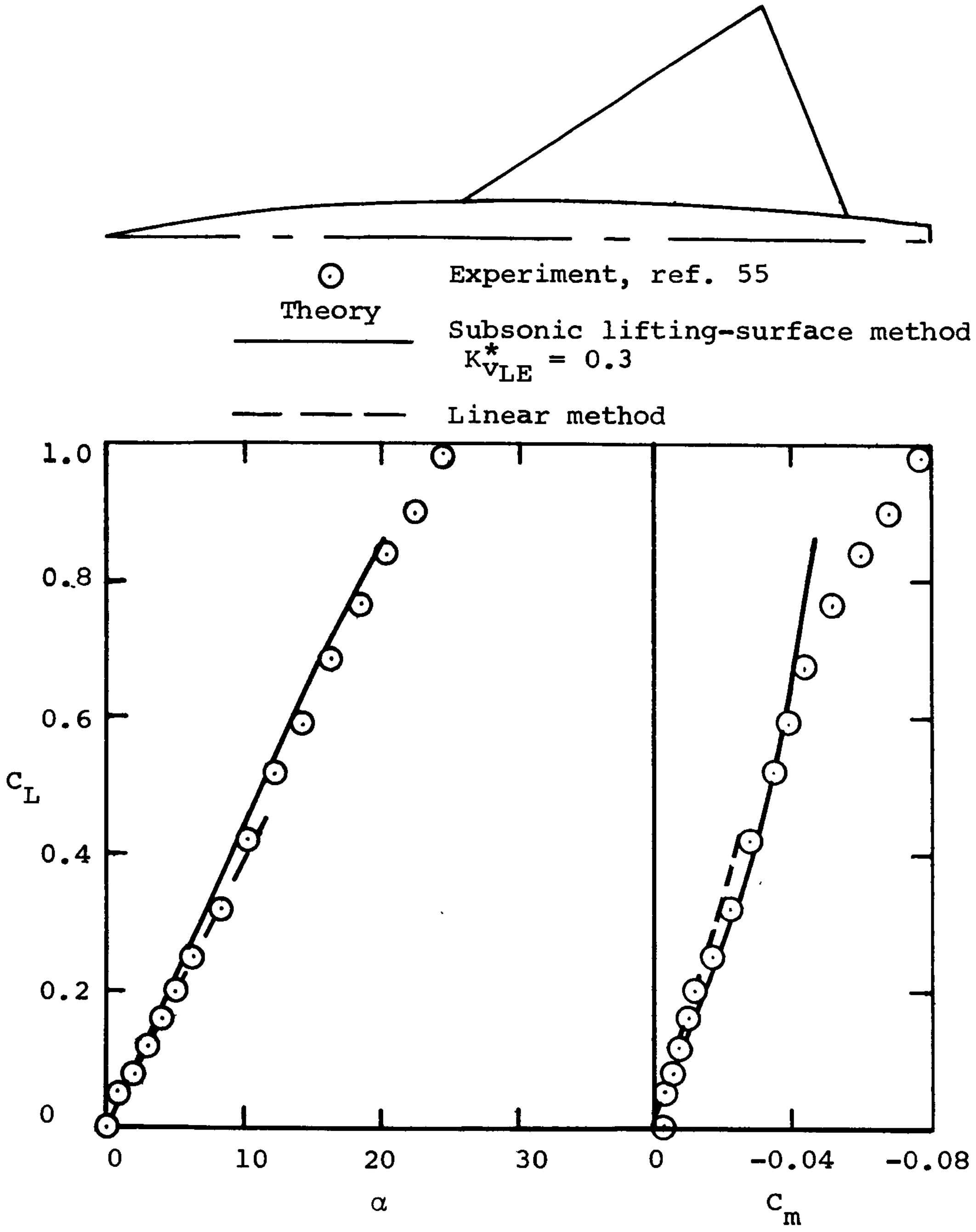

(a) M = 0.24.

Figure 18.- Comparison of measured and predicted lift and pitching-moment coefficients on a wing-body combination in subsonic flow.

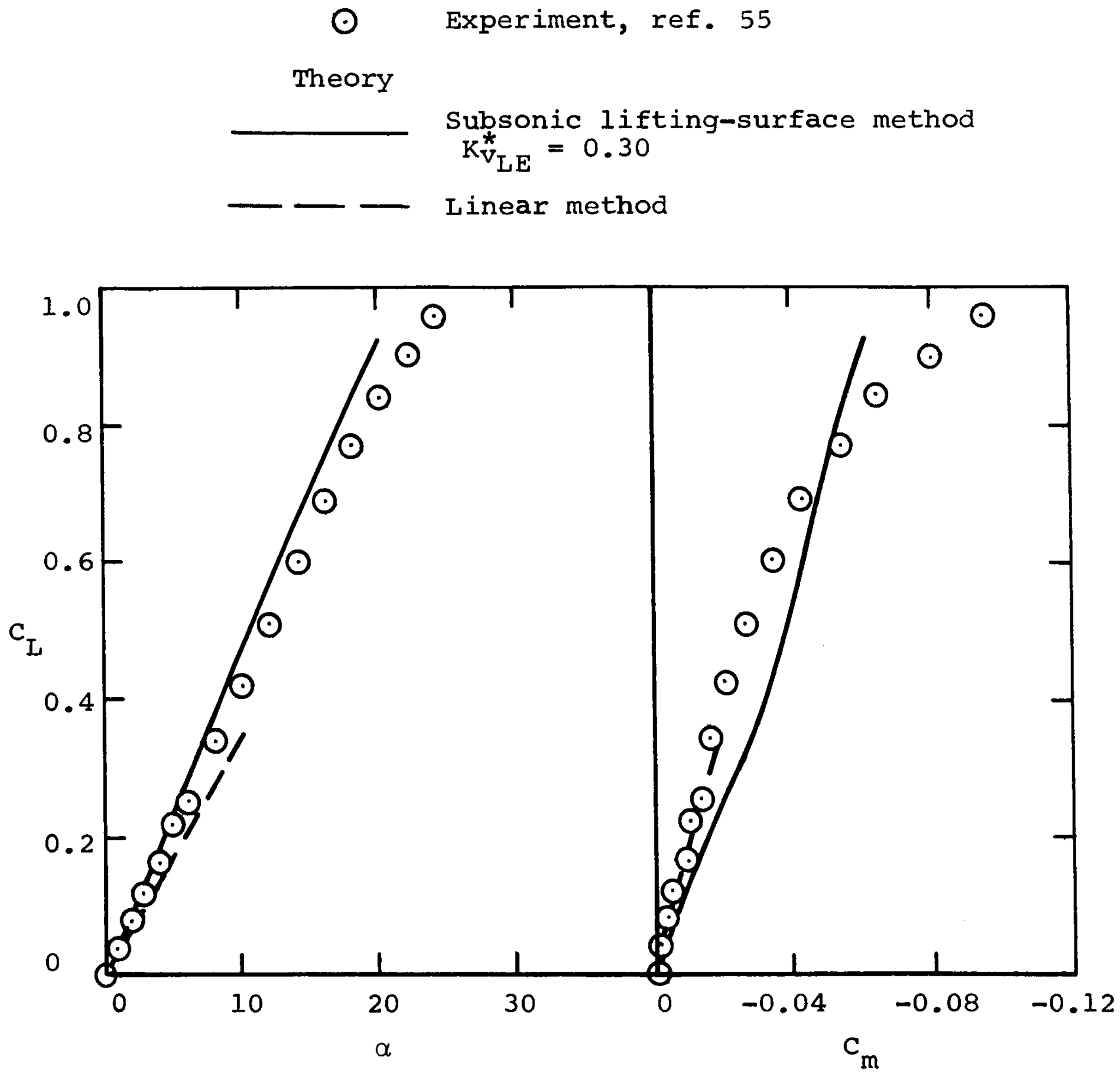

(b) M = 0.6.

Figure 18.- Continued.

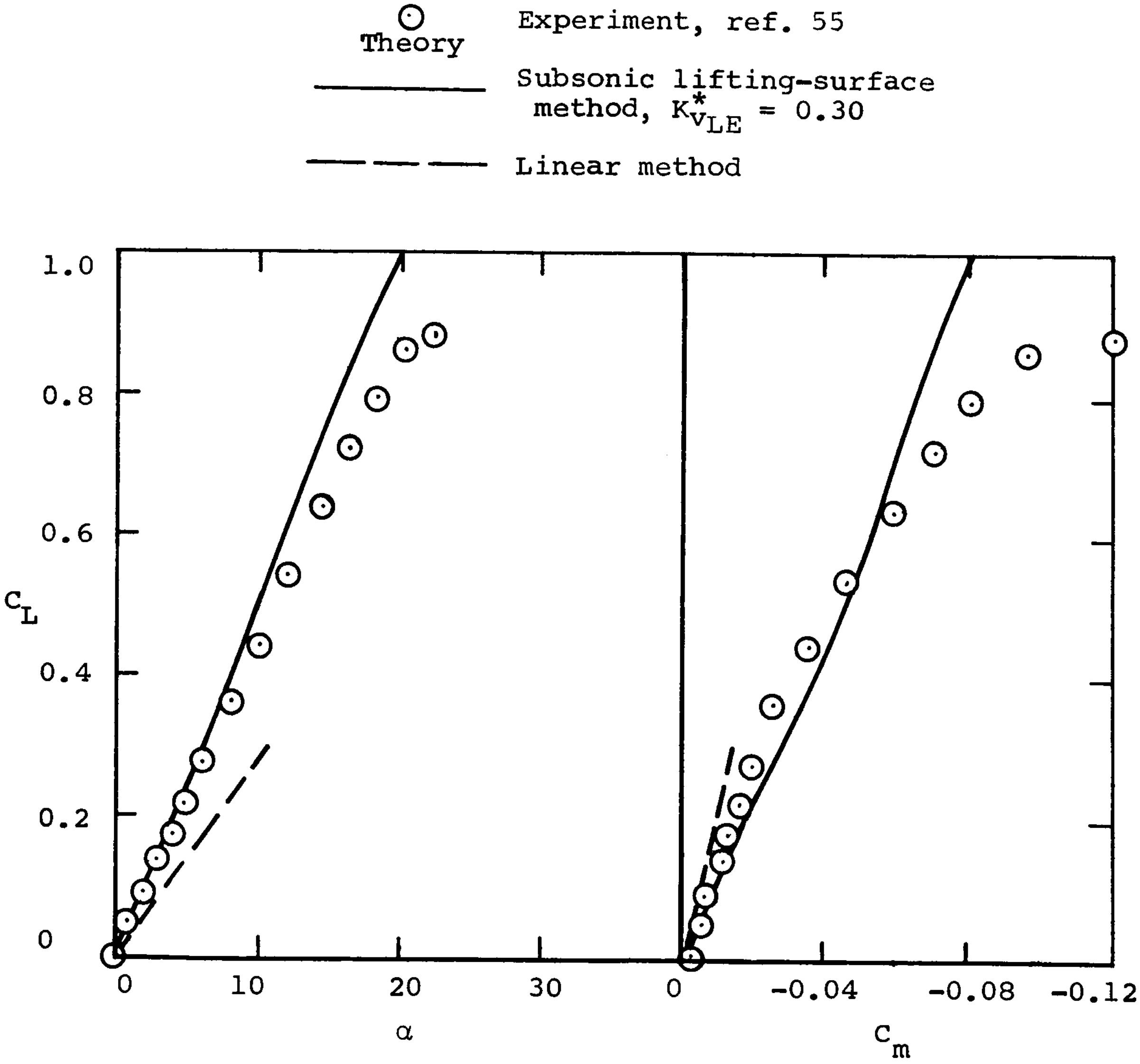

(c) M = 0.8.

Figure 18.- Concluded.

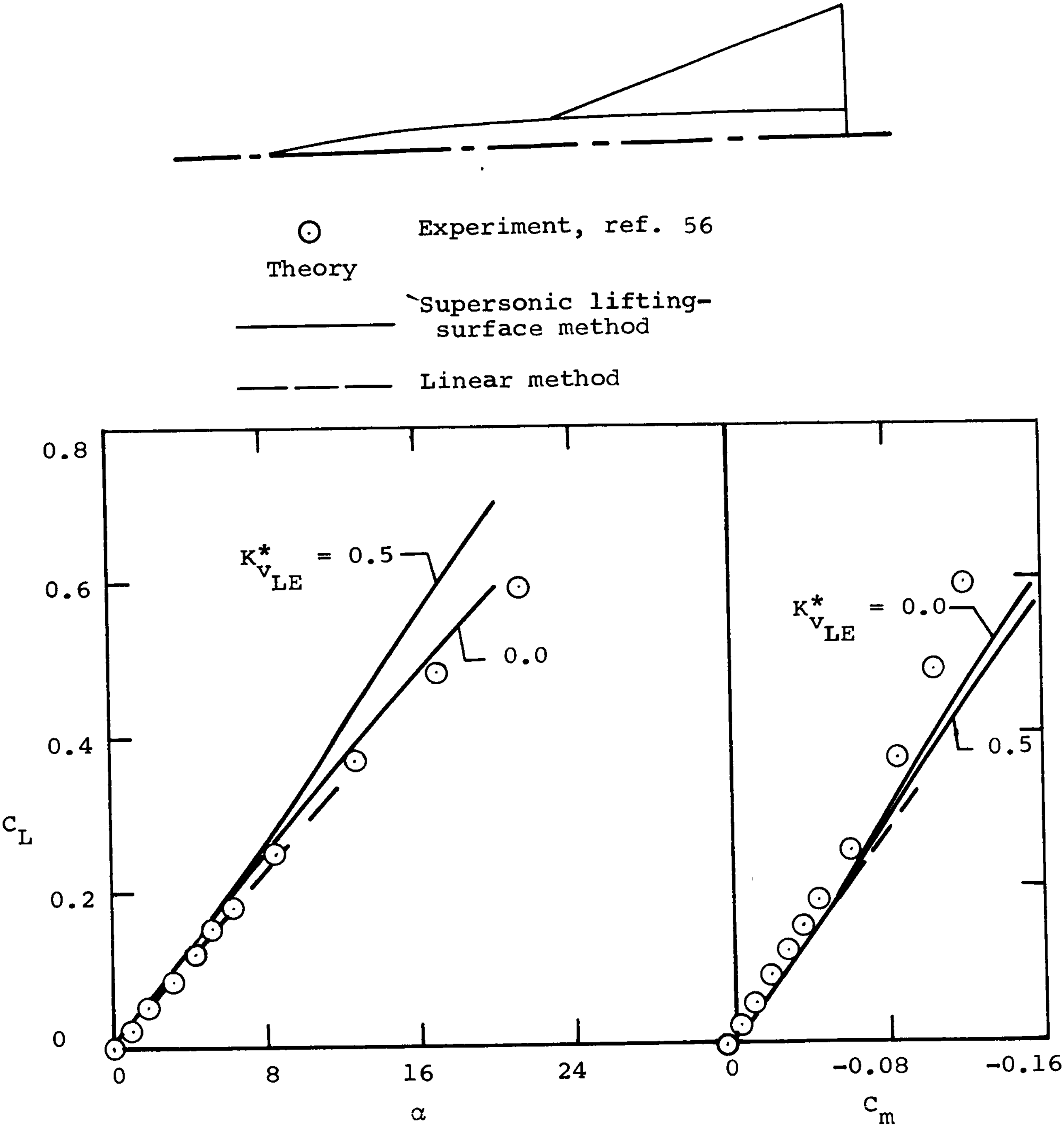

(a) Canard off.

Figure 19.- Comparison of measured and predicted lift and pitching-moment coefficients on a canard-body-wing configuration at M = 2.01.

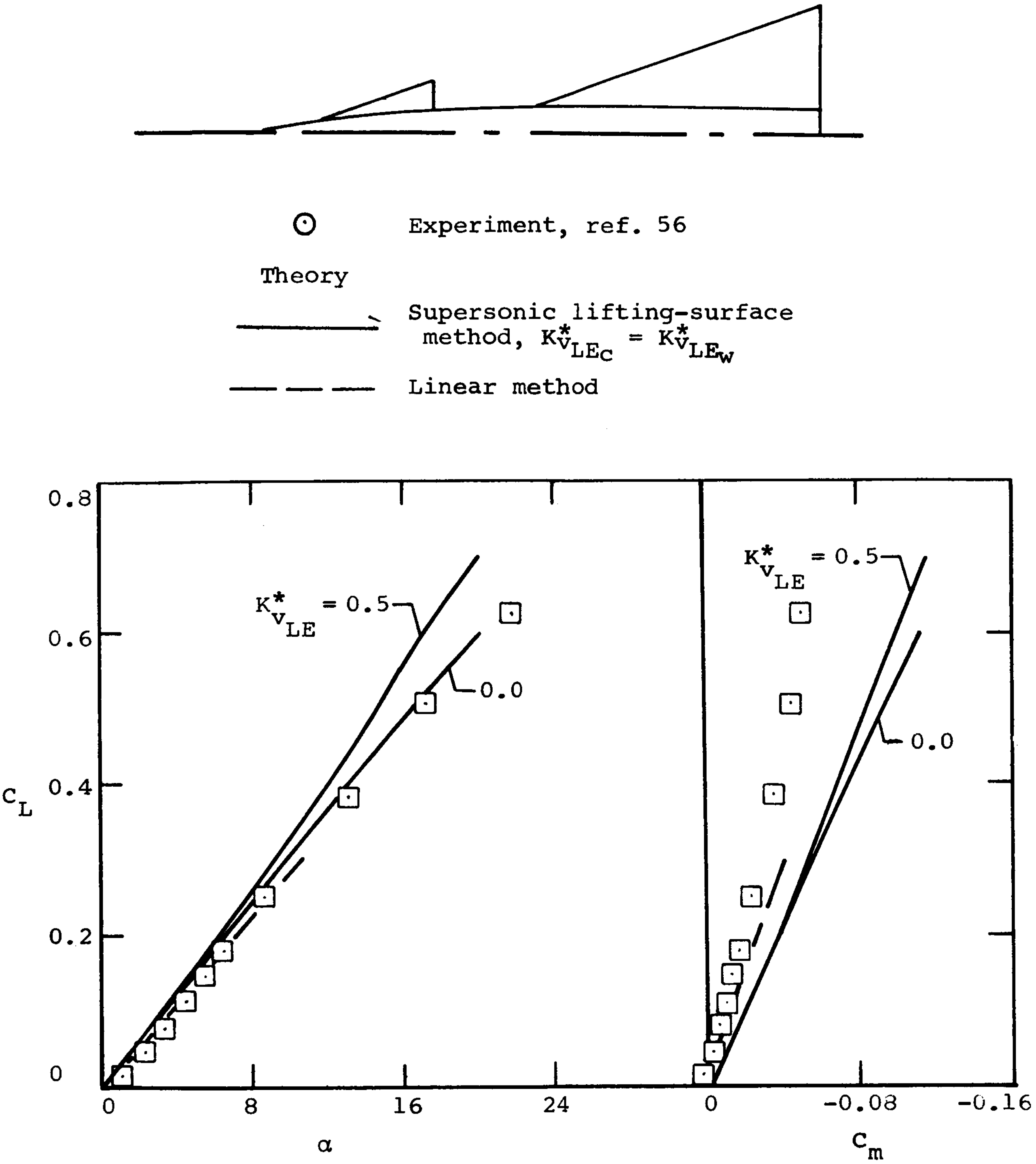

(b) Canard on, $\delta_c = 0^\circ$.

Figure 19.- Continued.

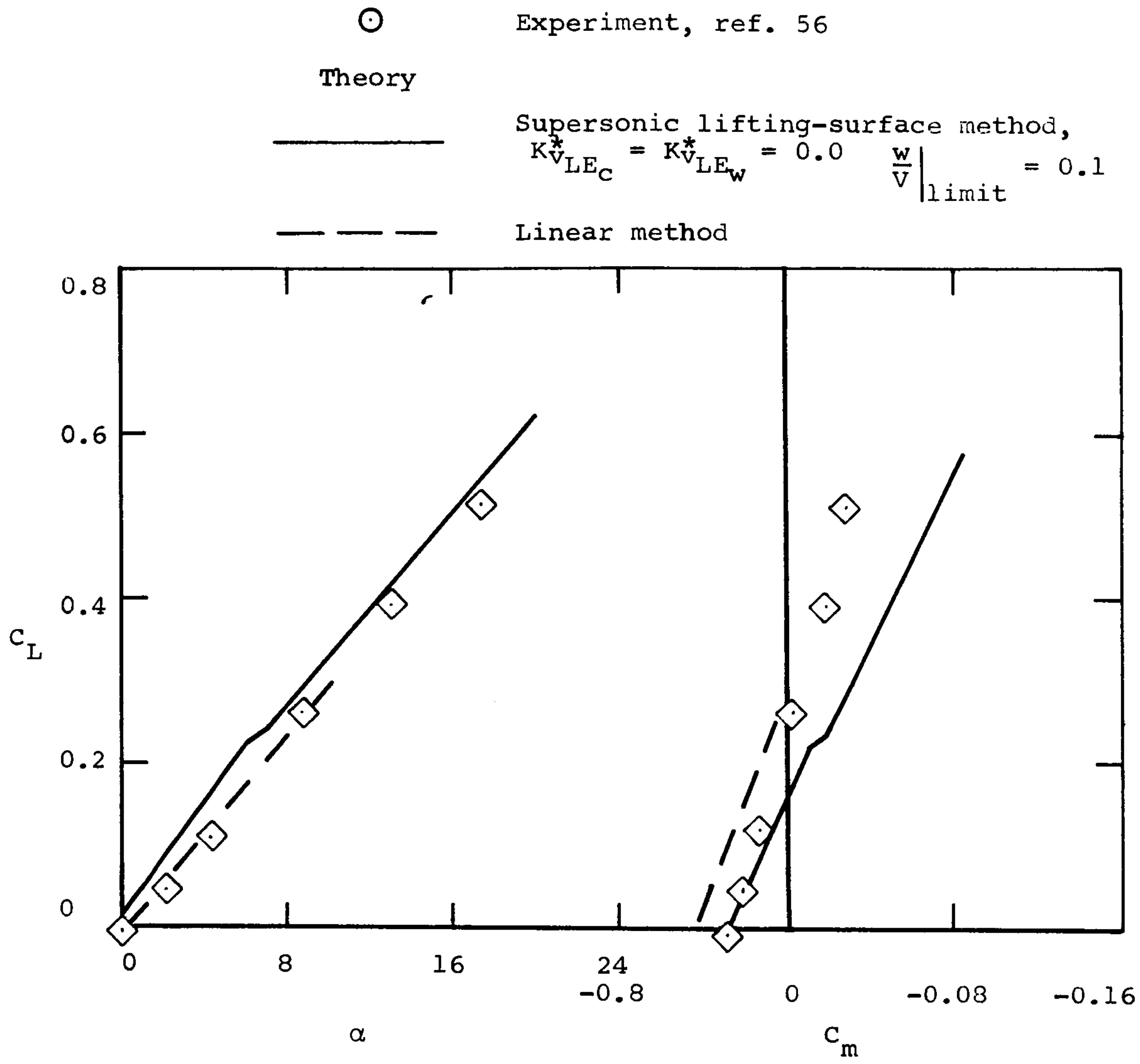

(c) Canard on, $\delta_c = 10^\circ$.

Figure 19.- Concluded.

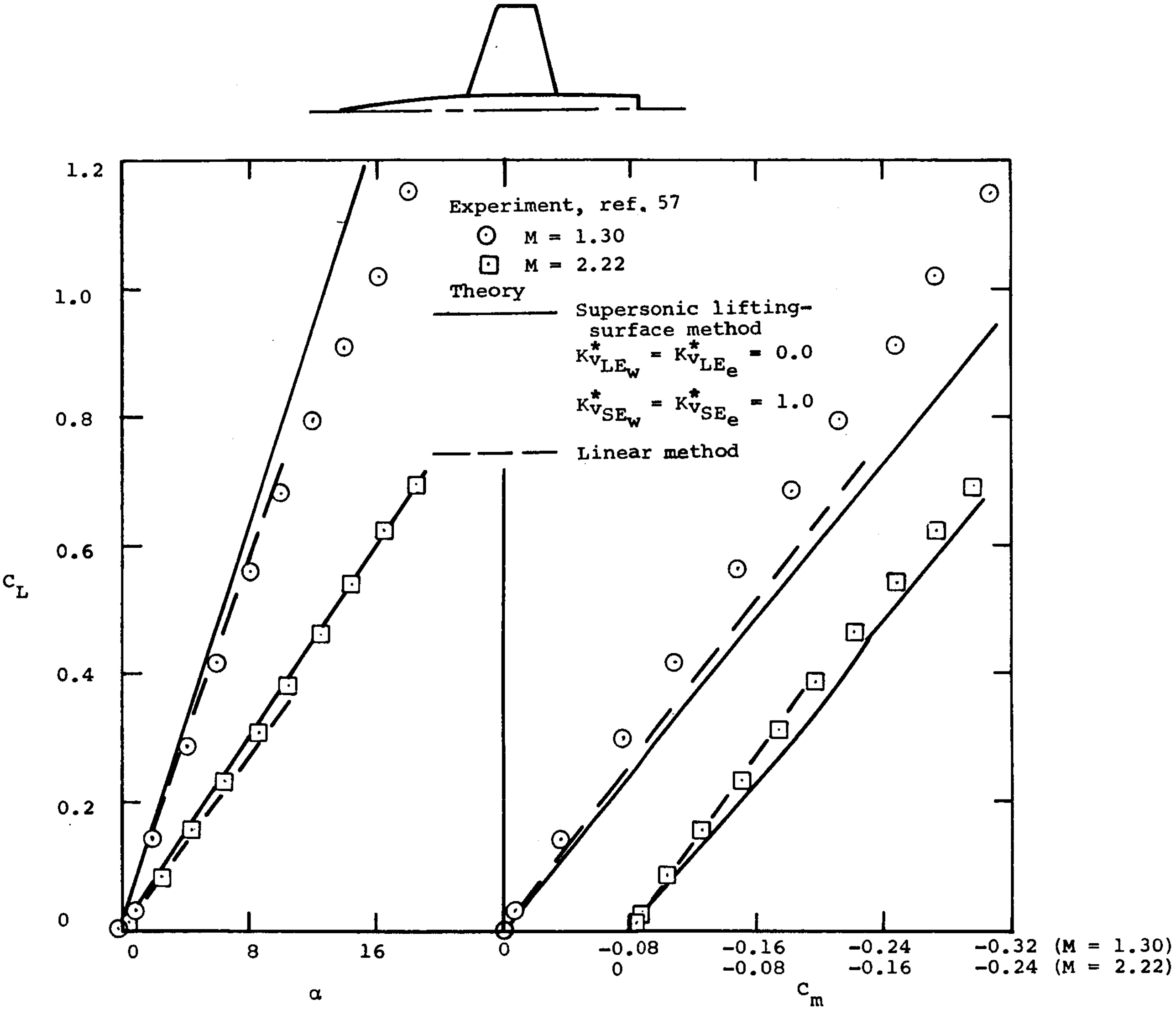

(a) Tail off; M = 1.30 and 2.22.

Figure 20.- Comparison of measured and predicted lift and pitching-moment coefficients on a wing-body-tail configuration in supersonic flow.

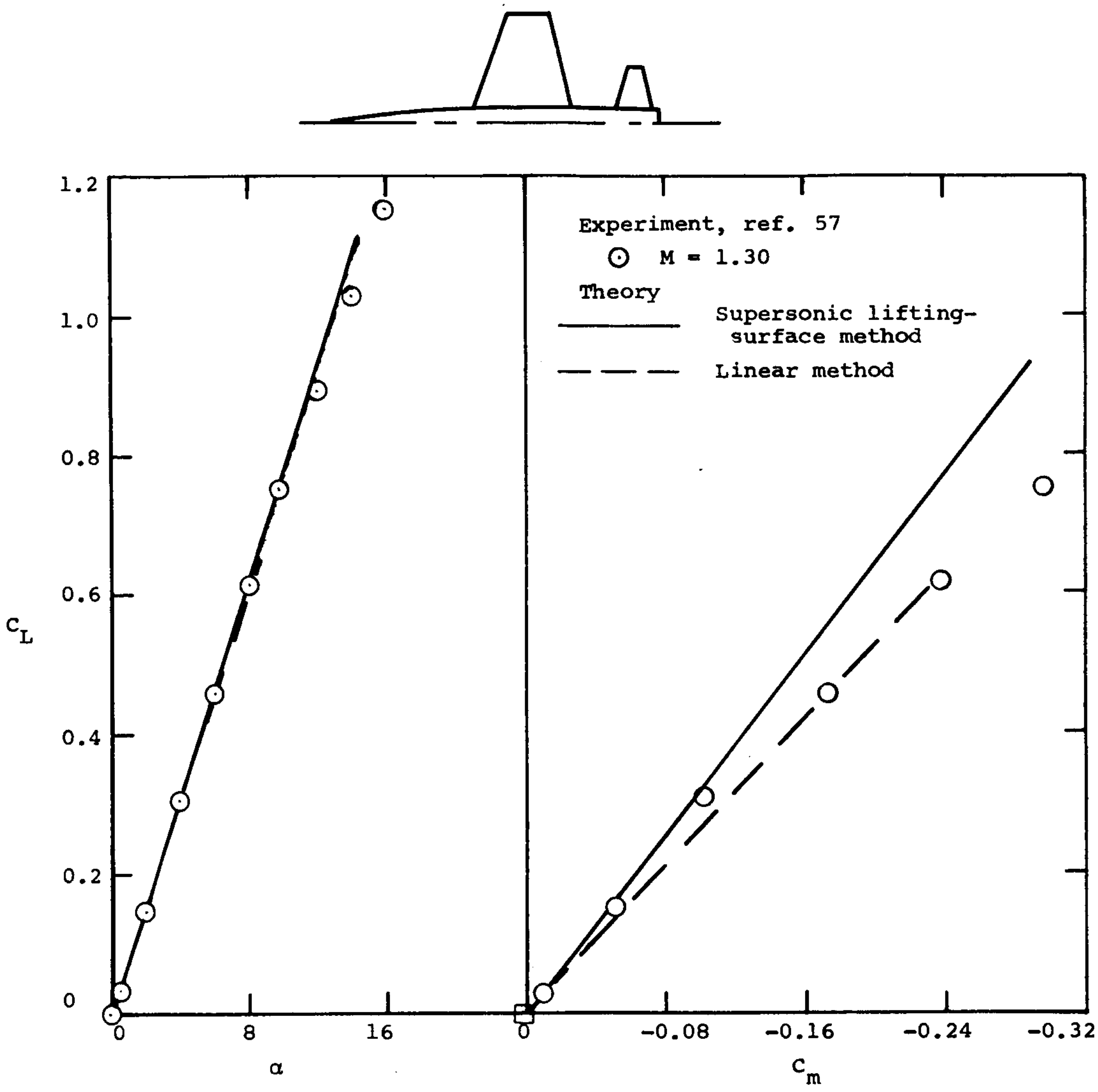

(b) Tail on, $\delta_e = 0^\circ$.

Figure 20.- Continued.

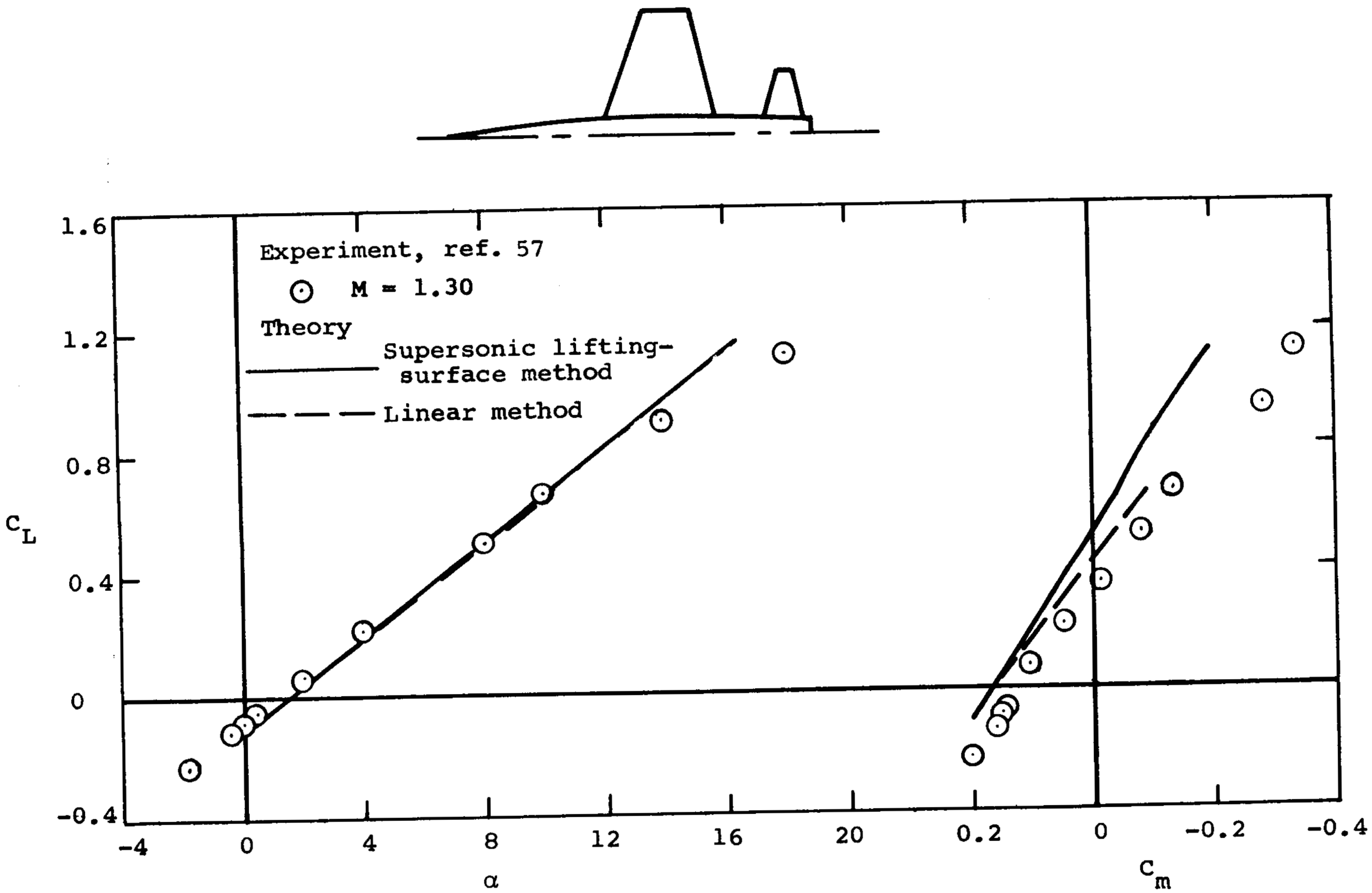

(c) Tail on, $\delta_e = -10^\circ$.

Figure 20.- Continued.

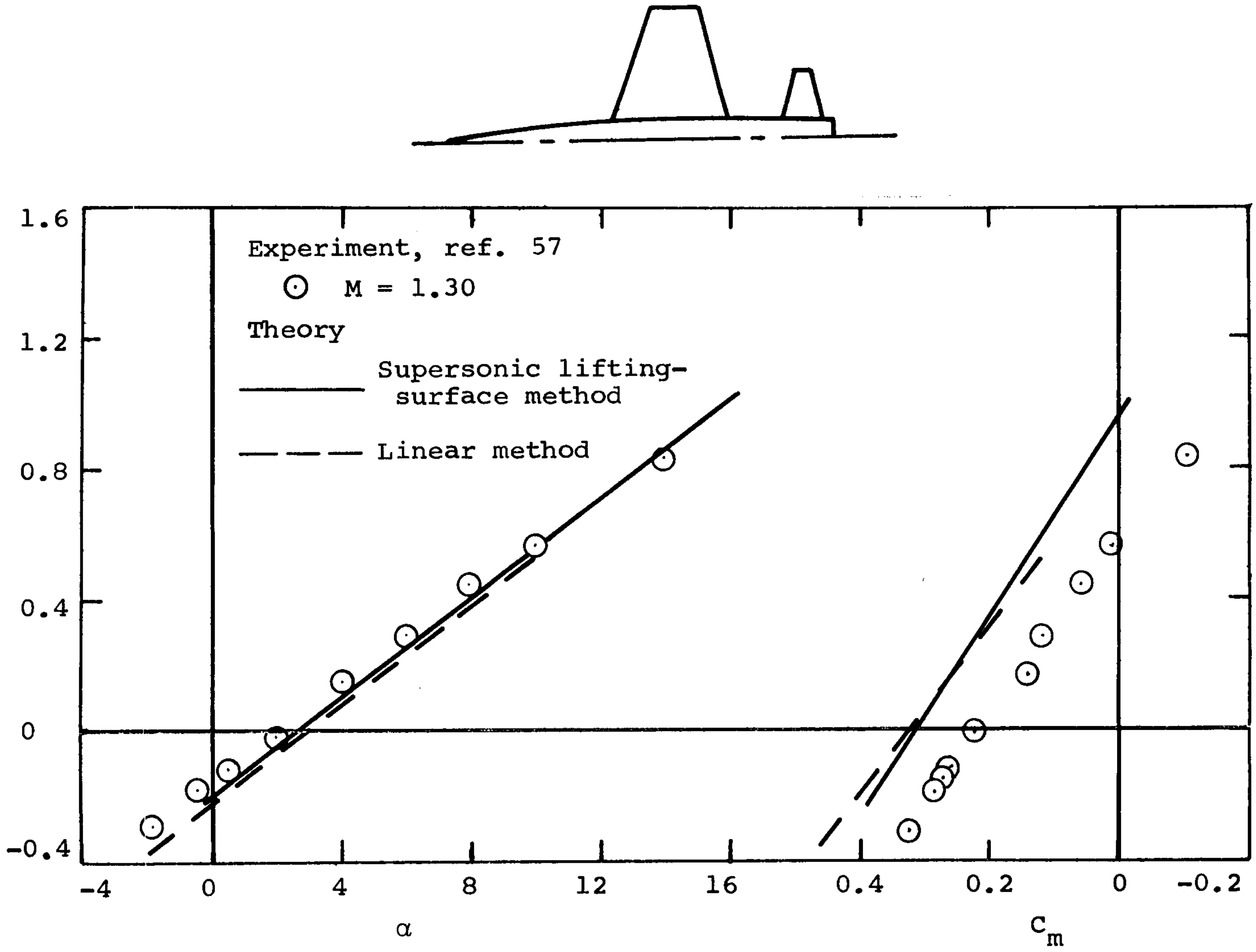

(d) Tail on, $\delta_e = -20^{\circ}$.

Figure 20.- Concluded.

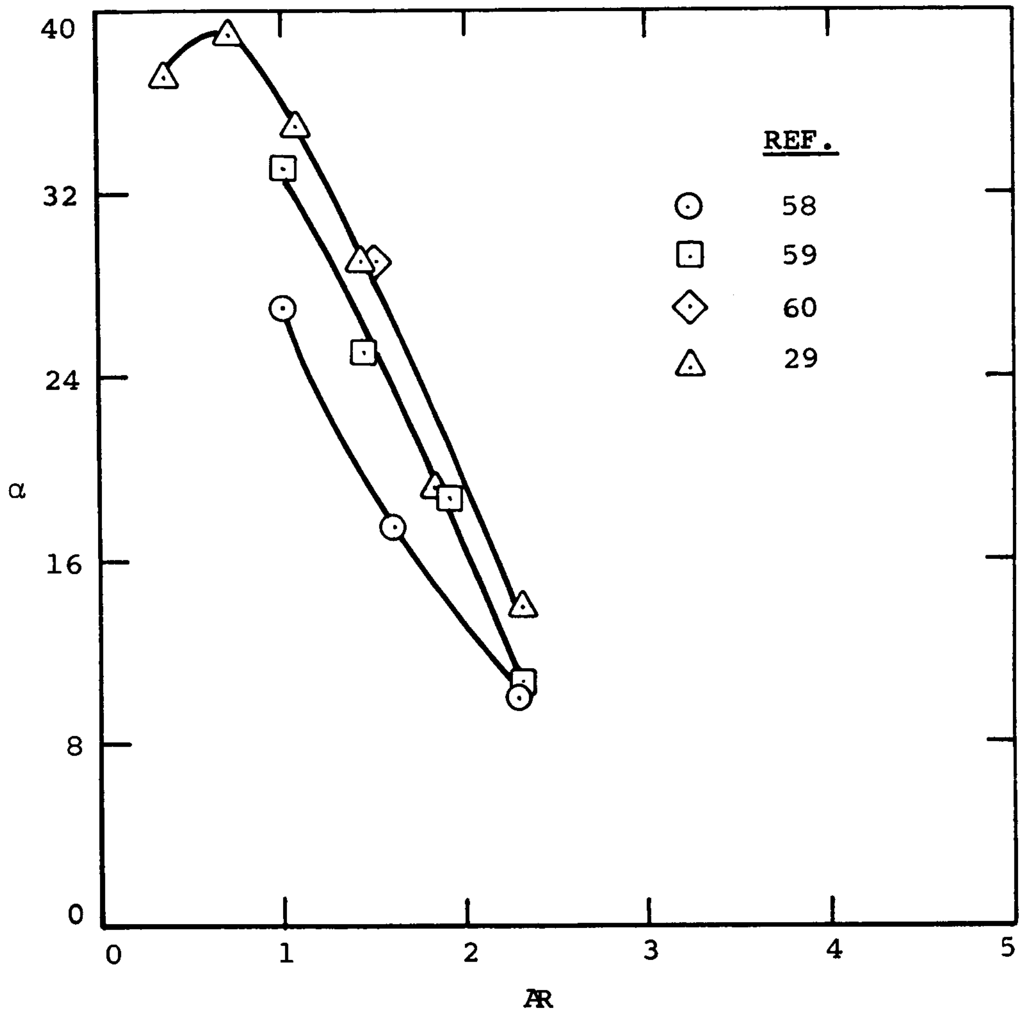

Figure 21.- Angle of attack for vortex bursting at the trailing edge of delta wings.

NASA-Langley, 1975

1. Report No.
NASA CR 2473

2. Government Accession No.

3. Recipient's Catalog No.

4. Title and Subtitle
EFFECT OF SYMMETRICAL VORTEX SHEDDING ON THE LONGITUDINAL AERODYNAMIC CHARACTERISTICS OF WING-BODY-TAIL COMBINATIONS

5. Report Date
January 1975

6. Performing Organization Code

7. Author(s)
Michael R. Mendenhall and Jack N. Nielsen

8. Performing Organization Report No.

9. Performing Organization Name and Address
Nielsen Engineering and Research, Inc.
510 Clyde Avenue
Mountain View, CA 94043

10. Work Unit No.

11. Contract or Grant No.
NAS 2-7347

12. Sponsoring Agency Name and Address
National Aeronautics and Space Administration
Washington, D.C.

13. Type of Report and Period Covered
Contractor Report

14. Sponsoring Agency Code

15. Supplementary Notes

16. Abstract

An engineering prediction method for determining the longitudinal aerodynamic characteristics of wing-body-tail combinations is developed. The method includes the effects of nonlinear aerodynamics of components and the interference between components. Nonlinearities associated with symmetrical vortex shedding from the nose of the body are considered as well as the nonlinearities associated with the separation vortices from the leading edges and side edges of the lifting surfaces. The wing and tail characteristics are calculated using lifting-surface theories which include effects of incidence, camber, twist, and induced velocities from external sources of disturbance such as bodies and vortices. The lifting-surface theories calculate the distribution of leading-edge and side-edge suction which is converted to vortex lift using the Polhamus suction analogy. Correlation curves are developed to determine the fraction of the theoretical suction force which is converted into vortex lift. The prediction method is compared with experimental data on a variety of aircraft configurations to assess the accuracy and limitations of the method.

17. Key Words (Suggested by Author(s))
Engineering prediction method for longitudinal aerodynamic characteristics of wing-body-tail combinations

18. Distribution Statement
Unclassified - Unlimited

CAT. 01

19. Security Classif. (of this report)
Unclassified

20. Security Classif. (of this page)
Unclassified

21. No. of Pages
115

22. Price*
4.50

*For sale by the National Technical Information Service, Springfield, Virginia 22151